

NOTE TO USERS

This reproduction is the best copy available.

UMI®

615915222

FORMABILITY AND FATIGUE BEHAVIOR OF TAILOR (LASER) WELDED BLANKS FOR AUTOMOTIVE APPLICATIONS

by

Dheeraj Anand
B. E. – Metallurgy
Government College of Engineering, Pune, India, 2000

A thesis
presented to Ryerson University
in partial fulfillment of the
requirement for the degree of
Master of Applied Science
in the Program of
Mechanical Engineering

Toronto, Ontario, Canada, 2004

©Dheeraj Anand 2004

RYERSON UNIVERSITY LIBRARY

UMI Number: EC52910

INFORMATION TO USERS

The quality of this reproduction is dependent upon the quality of the copy submitted. Broken or indistinct print, colored or poor quality illustrations and photographs, print bleed-through, substandard margins, and improper alignment can adversely affect reproduction.

In the unlikely event that the author did not send a complete manuscript and there are missing pages, these will be noted. Also, if unauthorized copyright material had to be removed, a note will indicate the deletion.

UMI®

UMI Microform EC52910

Copyright 2008 by ProQuest LLC.

All rights reserved. This microform edition is protected against unauthorized copying under Title 17, United States Code.

ProQuest LLC
789 E. Eisenhower Parkway
PO Box 1346
Ann Arbor, MI 48106-1346

Borrower's Page

Ryerson University requires the signatures of all persons using or photocopying this thesis. Please sign below, and give address and date.

[illegible]

Abstract

Formability and Fatigue Behavior of Tailor (Laser) Welded Blanks for Automotive Applications

©Dheeraj Anand 2004

Master of Applied Science
Department of Mechanical and Industrial Engineering
Ryerson University

The drive towards weight reduction in the automotive industry has led to the use of tailor welded blanks (TWBs). This work is aimed at evaluating the forming and fatigue behavior of the TWBs with different thickness combinations and compositions. Forming tests were carried out to determine the forming limit diagrams (FLDs) of the TWBs, and compared with those of the individual steel sheets. The results showed that the FLDs of the TWBs lie in-between those of the individually formed steel sheets that comprise the TWBs. A semi-empirical relation based on the mean values of the strain-hardening exponents (n -values) and of the thickness of the base metals was developed to calculate the FLD_0 of the TWBs. The calculated FLD_0 values were found to be in good agreement with the experimentally determined values. The fatigue tests showed that TWBs made from zinc coated/galvanized steels exhibited a lower fatigue limit, as compared with the TWB combinations from comparable uncoated steel. This was attributed to the intergranular cracking in the galvanized TWBs, caused by the presence of zinc penetrating beneath the sheet surface.

Acknowledgements

I initially would like to thank my supervisors Dr. S. D. Bhole and Dr. D. L. Chen for their excellent guidance, continuous support and patience throughout my research work.

I also would like to thank DOFASCO Inc., Hamilton, ON, Canada for their interest in this work and support for carrying out a part of the experiments at their Research and Development Facility. The guidance and support extended by Mr. Paul Andreychuk and Mr. Gary Boudreau is gratefully acknowledged.

I would like to thank the Department of Mechanical and Industrial Engineering and the School of Graduate Studies at Ryerson University for their support in terms of departmental facilities, research stipend and scholarship.

I would like to acknowledge my supervisors funding resource – Natural Sciences and Engineering Research Council of Canada (NSERC) for the financial support provided for this research.

Finally, I would like to thank all my family and friends for their support and encouragement through this endeavor.

Table of Contents

Author's Declaration	ii
Borrower's Page	iii
Abstract	iv
Acknowledgements	v
Table of Contents	vi
List of Figures	viii
List of Tables	xi
Nomenclature	xii
Chapter 1 Introduction	1
1.1 Introduction	1
Chapter 2 Fundamental Knowledge and Literature Survey	3
2.1 Manufacturing of Tailor Welded Blanks	3
2.2 Forming Process	4
2.2.1 Forming Limit Diagram	9
2.2.2 Measurement of Forming Strains	13
2.2.3 Factors Affecting the Forming Process	18
2.2.3.1 Material Properties	18
2.2.3.2 Die Geometry	19
2.2.3.3 Lubrication	21
2.3 Fatigue of Formed Components	22
2.4 Recent Studies on Formability of Tailor Welded Blanks	25
2.5 Recent Studies on Fatigue of Tailor Welded Blanks	30
2.6 Objectives of Research	32
Chapter 3 Experimental Procedure	34
3.1 Materials	34
3.2 Sample Preparation and Testing	36
3.2.1 Laser Welding Parameters	36
3.2.2 Formability Tests and Strain Measurement	36
3.2.3 Tensile Tests	42

3.2.4 Fatigue Tests	44
3.2.5 Microstructure and Microhardness Tests	46
3.2.6 Scanning Electron Microscopy	47
Chapter 4 Experimental Results	48
4.1 Microstructural Observations	48
4.2 Tensile Properties	48
4.3 Formability Results	51
4.3.1 Forming Limit Diagrams	51
4.3.2 Major and Minor Strains	54
4.4 Fatigue Results	56
Chapter 5 Discussion	57
5.1 On Weld Quality and Failure Location	57
5.2 On Microhardness	60
5.3 On Formability	63
5.3.1 Effect of Strain-hardening Exponent and Sheet Thickness on the FLD ₀ of Tailor Welded Blanks	63
5.3.2 Comparison of the Forming Limit Diagram of Tailor Welded Blanks with the Base Metals	67
5.4 On Fatigue Strength	72
Chapter 6 Conclusions	78
6.1 Summary	78
6.2 Recommendations for Future Work	80
References	81
Appendix A	86
Appendix B	91
Appendix C	95
Appendix D	106

List of Figures

Figure 1.1. Various tailor welded blank components used in an automotive structure	2
Figure 2.1. Laser welding process.....	4
Figure 2.2. A door-inner panel stamped from a tailor welded blank.	5
Figure 2.3. Engineering stress - strain curve.	6
Figure 2.4. Incremental deformation of a principal element.....	8
Figure 2.5. Graphical representation of deformations in the two-dimensional strain space.....	9
Figure 2.6. Keeler's concept of Formability Limit.....	10
Figure 2.7. Keeler-Goodwin Curve—the first published full FLD.....	11
Figure 2.8. Standard FLD shape with a 10% marginal zone.	12
Figure 2.9. Commonly used grid patterns.....	15
Figure 2.10. Set up for electrochemical marking.	16
Figure 2.11. Deformed circular grid representing the major and minor strains.	16
Figure 2.12. Mylar tape used for calculating the major and minor strains.....	17
Figure 2.13. Grid analyzing system used for recording the forming strains.	17
Figure 2.14. Die geometry.	20
Figure 2.15. Draw bead and hemispherical punch used in laboratory experiments.	20
Figure 2.16. Draw bead simulator.....	22
Figure 2.17. Features of a fatigue fracture—A and B are the failure initiation points.	23
Figure 2.18. A schematic S-N curve showing the fatigue limit for steels.	24
Figure 2.19. Typical fatigue stress cycles.....	25
Figure 2.20. Two types of splitting in forming of TWBs.....	26
Figure 2.21. Specimen showing the limiting dome height to failure.....	27
Figure 2.22. Comparing the FLDs of different thickness TWBs with the base metal of thickness 1mm.....	28
Figure 2.23. Concept of new FLD for a different thickness TWB.....	29
Figure 2.24. Fatigue test results for laser and spot welds.	31
Figure 2.25. Effect of loading direction on fatigue strength for welded structure.	31

Figure 2.26. Effect of welding process on fatigue strength.....	32
Figure 3.1. MTS 866.02 formability press.....	37
Figure 3.2. Hemispherical punch used for the forming tests.....	38
Figure 3.3. Formed specimen showing fracture/necking as the failure criterion.	38
Figure 3.4. Shims and rubber puck used for forming tests.	39
Figure 3.5. Specimen widths superimposed on a forming limit diagram.....	40
Figure 3.6. SGA software screen for locating the deformed squares.	41
Figure 3.7. SGA software screen showing the major and minor strains.	42
Figure 3.8. Geometry and dimensions of standard tensile test specimens.....	43
Figure 3.9. Geometry and dimensions of fatigue test specimens with a laser-welded butt joint.....	44
Figure 3.10. Light micrograph showing the indent pattern, size and spacing across the weld.	47
Figure 4.1. Microstructures of the laser welded blanks. (a) GMX (b) W-Car (c) MC-DI.....	49
Figure 4.2. Stress-strain curves of the thinner base metals of the TWBs.....	50
Figure 4.3. Stress-strain curves of the thicker base metals of the TWBs.	51
Figure 4.4. Comprehensive FLD for GMX TWB.....	52
Figure 4.5. Comprehensive FLD for W-Car TWB.....	53
Figure 4.6. Comprehensive FLD for MC-DI TWB.....	53
Figure 4.7. S-N curves for the base metal and different TWB combinations, tested at 50 Hz, R = 0.1 and room temperature.	56
Figure 5.1. Failure location in narrow width specimens.....	59
Figure 5.2. Failure location in broad width specimens.....	60
Figure 5.3. Microhardness profile of the three TWBs.	61
Figure 5.4. Typical microstructures in the laser welded blanks. (a) Base metal (b) Weld metal.	63
Figure 5.5. Principle of similar triangles for interpolation.....	65
Figure 5.6. Forming limit diagram for GMX TWB combination.	68
Figure 5.7. Forming limit diagram for W-Car TWB combination.	70

Figure 5.8. Forming limit diagram for MC-DI TWB combination.	71
Figure 5.9. Typical SEM micrographs showing the fatigue initiation sites. (a) W-Car (b) MC-DI (c) GMX and (d) BM.	75
Figure 5.10. SEM micrograph showing the regime of fatigue crack propagation. (a) W-Car (b) MC-DI.	75
Figure 5.11. Low-magnification SEM micrograph showing an overall view of the fracture surfaces and the corresponding EDS spectrum. (a) and (b) W-Car (c) and (d) MC-DI.	76
Figure 5.12. SEM micrograph showing the area of fatigue crack growth. (a) GMX (b) BM.	76
Figure 5.13. Low-magnification SEM micrograph showing an overall view of the fracture surfaces and the corresponding EDS spectrum. (a) and (b) GMX (c) and (d) BM.	77

List of Tables

Table 2.1. Comparison of failure height from the base and strain values of specimens with same deformation mode.	28
Table 3.1. Chemical composition of the materials.	35
Table 3.2. Physical parameters of the tailor welded blanks.	35
Table 3.3. Laser welding parameters.	36
Table 4.1. Tensile properties of the base metals.	50
Table 4.2. Minor and major strain values for the TWBs.	54
Table 5.1. Failure location and orientation in different width specimens.	59
Table 5.2. Comparison of the calculated and adjusted measured FLD_0 value for the TWBs.	66
Table 5.3. Percentage increase in the FLD_0 values of TWBs.	71
Table 5.4. Fatigue ratio of the TWBs and BM.	73

Nomenclature

Acronym	Definition
A/SP	Auto/steel partnership
ASTM	American society for testing and materials
CCD	Charge coupled device
CO ₂	Carbon di-oxide
CRT	Cathode-ray tube
DP	Dual phase
EDDQ	Extra deep drawing quality
EDS	Energy dispersive X-ray spectrometry
FLD	Forming limit diagram
FLD ₀	Forming limit value under plane strain condition
HAZ	Heat-affected zone
HSLA	High strength low alloy
IF	Interstitial free
LASER	Light amplification by stimulated emission of radiation
LDH	Limiting dome height
NADDRG	North American deep drawing research group
Nd:YAG	Neodymium: yttrium-aluminum-garnet
SAE	Society of automotive engineers
SEM	Scanning electron microscope
SGA	Square grid analyzer
TRIP	Transformation induced plasticity
TWB	Tailor welded blank
UTS	Ultimate tensile strength
YS	Yield strength

Symbol	Definition
A	Amplitude ratio
A_c	Cross-sectional area
e	Engineering strain
K	Strength coefficient
n	Strain-hardening exponent
N	Number of cycles
P	Applied load
P_{\max}	Maximum load
P_{mean}	Mean load
P_{\min}	Minimum load
r	Coefficient of anisotropy
R	Stress ratio
S	Engineering stress
t	Material thickness
β	Strain ratio
ϵ	True strain
σ	True stress
σ_a	Stress amplitude
σ_m	Mean stress
σ_{\max}	Maximum stress
σ_{\min}	Minimum stress

Chapter 1

Introduction

1.1 Introduction

In the past two decades, the automotive industry has seen stringent government regulations concerning fuel conservation and safety mandates along with environmental concerns. These regulations have prompted automakers to come up with innovative solutions to design lighter cars for reduced fuel consumption, while improving the overall structure of the vehicles for occupant safety. However, these changes have led to a significant increase in the manufacturing costs. To reduce the costs and the weight, alternate materials such as aluminum and composites have been proposed for body panels, but none have shown the versatility of steel. Various new grades of steel have been developed which show excellent forming quality and are able to meet most automotive requirements [1].

The conventional automobile body components consist of several individually formed stampings being spot welded together in order to meet the material and strength requirements at various locations in the assembly. Alternatively, various steel options can be welded together prior to the forming process to produce a tailor welded blank (TWB). Such a concept of combining different materials into a welded blank enables engineers to "tailor" the blank so that appropriate material with the required properties are located precisely within the part where needed [1]. The differences in the materials can be found in their grade, thickness, strength and surface condition like galvanized (zinc coated), galvanized (zinc-aluminum coated) or cold rolled and annealed. Tailor welded blanks are currently used for body side frames, door inner panels, motor compartment rails, center pillar inner panels and wheelhouse / shock tower panels as seen in Figure 1.1.

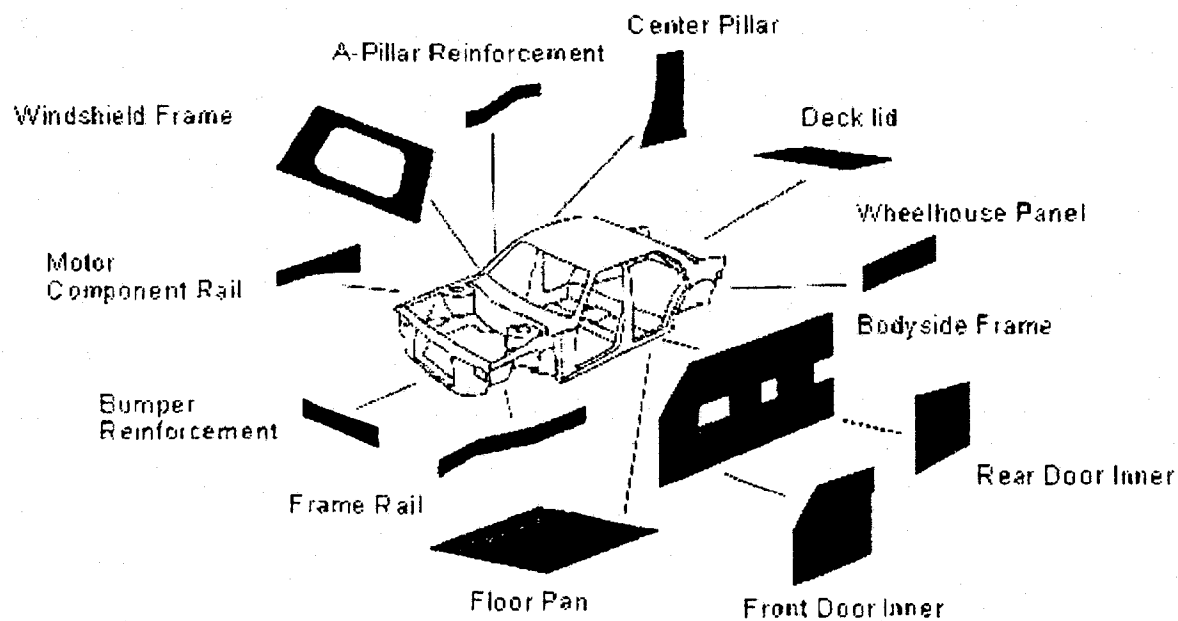


Figure 1.1. Various tailor welded blank components used in an automotive structure [1].

Tailor welded blanks, having generated enormous interest in the automotive industry, have been found to have many potential benefits, including [1]:

- a. Fewer parts,
- b. Fewer dies,
- c. Fewer spot welds,
- d. Reduced design and development time,
- e. Lower manufacturing costs,
- f. Less material input, better utilization of steel,
- g. Weight reduction,
- h. Improved dimensional accuracy,
- i. Improved structural integrity,
- j. Improved safety,
- k. Reduced scrap.

Chapter 2

Fundamental Knowledge and Literature Survey

2.1 Manufacturing of Tailor Welded Blanks

Tailor welded blanks, as the name suggests, involve the welding of two (or more) sheets together. The different types of welds identified for this application include:

- a. Laser Beam
- b. Resistance Mash Seam
- c. High Frequency Induction
- d. Electron Beam

By far, laser tailor welded blanks have found the widest applications in the automotive industry [1]. Both solid state CO₂ and Nd:YAG are being used as the source to generate the laser beams. For automotive applications involving laser welding of thinner sections (in this study), no weld consumable or filler wire is used. The laser weld produces a butt-joint with a narrower (about 1 mm) heat-affected zone (HAZ), as compared to other processes. In the resistance mash seam welding process, the HAZ is about twice the width of the laser weld. The other identified advantages of laser welding are better appearance, weather seal surface and better noise suppression. A laser beam (Figure 2.1) can be used to weld a maximum weld length of about 3800 mm and the use of a multi-axes robotic system makes it possible to weld a non-parallel bead. All these factors and especially the narrower HAZ have made laser welding popular for manufacturing tailor welded blanks [1].

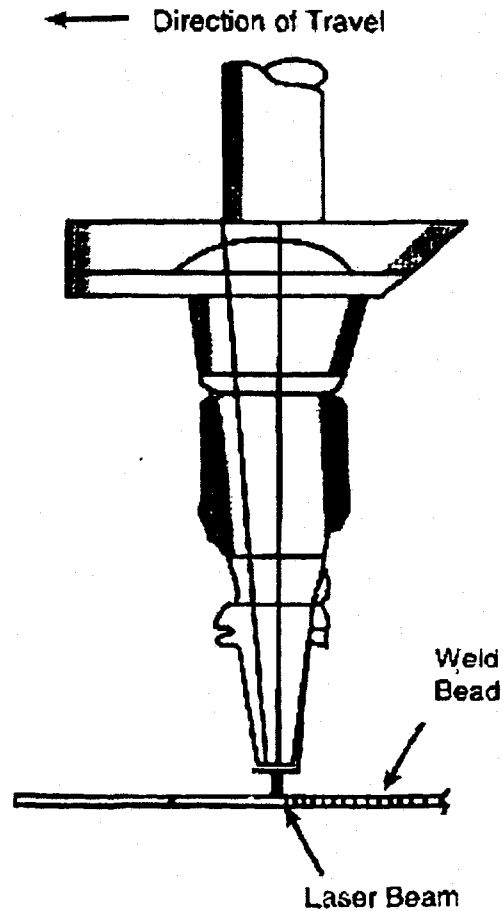


Figure 2.1. Laser welding process [1].

2.2 Forming Process

Forming (or stamping) is defined as the permanent deformation of a sheet metal blank into the desired shape using a set of matching die sets. During the course of the stamping process, sheet metal is subjected to both elastic and plastic deformation, which together constitutes the total deformation. It is the plastic (permanent) deformation that remains in the stamping on the removal of the applied load, and thus the final shape of the blank is achieved, as seen in Figure 2.2. Elastic deformation is released as springback or elastic recovery of the stamping [2]. The

amount of plastic deformation is expressed in terms of strain or sometimes referred to as stretch. Strain is a dimensionless quantity and refers to the amount (%) by which a panel has been deformed or changed from its original length. On the other hand, stress is the intensity of force within a metal which resists a change in shape and dimension. It is defined as the force per unit area.

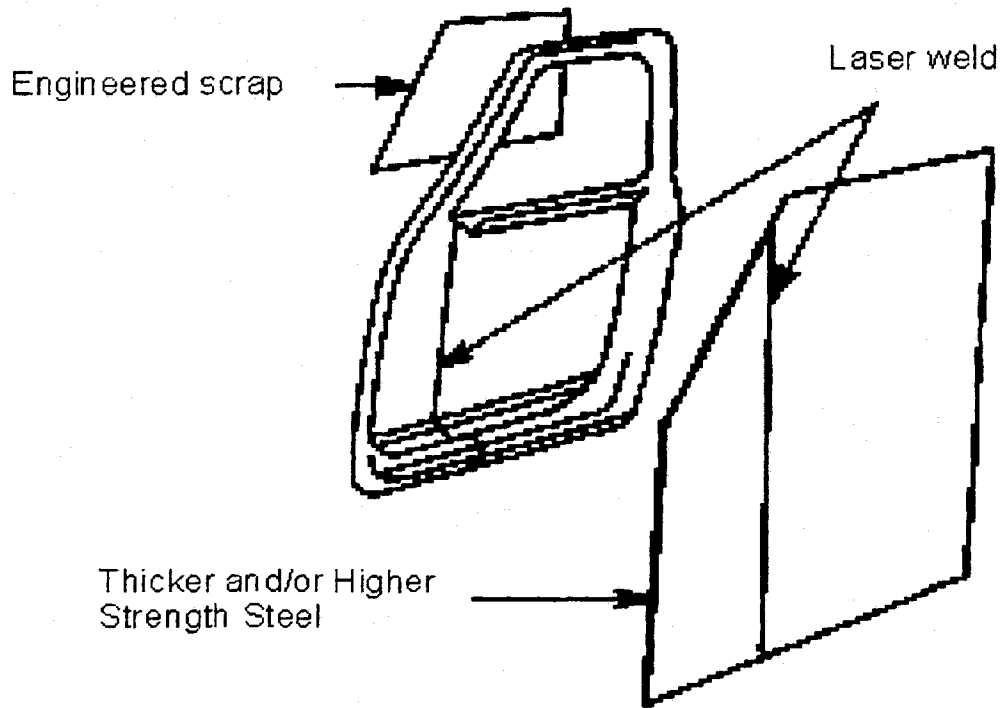


Figure 2.2. A door-inner panel stamped from a tailor welded blank.

The stress – strain ($\sigma - \epsilon$) curve, as shown in Figure 2.3, is generated by recording the load with progressive extension of the test specimen. The load and displacement obtained are then converted to the stress and strain, respectively. The two important material properties that govern the forming process are yield stress (YS) and ultimate tensile stress (UTS). As seen from Figure 2.3, the strain corresponding to the yield stress is the elastic strain and the strain between the yield stress and the ultimate tensile stress is the plastic strain. This range of strain is called the plastic deformation range, and for a successful stamping process the applied stresses must

be within this range. If the stresses are lower than the yield stress, no permanent plastic deformation occurs, and the stresses higher than the ultimate tensile stress will lead to splitting or fracture [2].

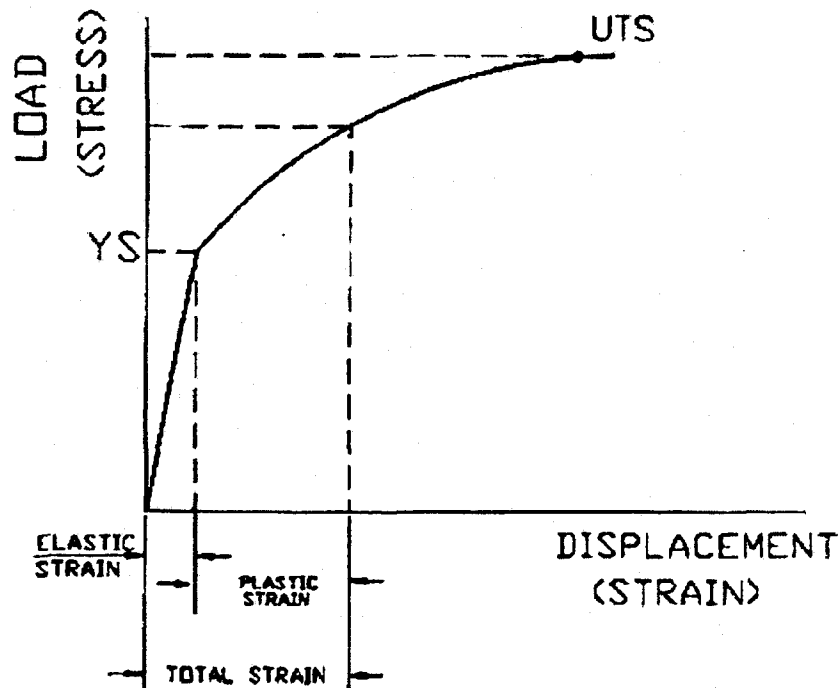


Figure 2.3. Engineering stress - strain curve [2].

A panel being formed is subjected to strains in three different directions, viz., major strain (ϵ_1), minor strain (ϵ_2) and thickness strain (ϵ_3). These three strains have the following relationships amongst them [2]:

- The volume of the metal always remains constant.
- An increase in the surface area results in the thinning of the panel.
- A decrease in the surface area results in the thickening of the panel.

In other words, there is no material being added or taken away during a stamping process and is referred to as incompressibility [3]. Further, the deformation in sheet metal stamping is termed as pure, proportional when [3]:

- a. The ratio of the strain increments remains constant,
- b. The process is monotonic, i.e., there are no reversals, and
- c. The principal directions remain fixed with respect to the material.

During incompressible plastic deformation, the sum of the principal strain increments is zero. The material just flows along different contours of the die set to develop the final shape of the panel being produced. This can be illustrated by considering an infinitesimal element of material as shown in Figure 2.4. On applying principal stresses, this element will deform. If the sides of the element are a , b and c initially, and $a+da$, $b+db$ and $c+dc$ subsequently, the principal incremental strains are:

$$\begin{aligned}\partial\epsilon_1 &= \partial a/a \\ \partial\epsilon_2 &= \partial b/b \\ \partial\epsilon_3 &= \partial c/c\end{aligned}\tag{2.1}$$

For the element illustrated in Figure 2.4, incompressibility implies that [3]:

$$(a+da)(b+db)(c+dc) - abc = 0\tag{2.2}$$

Differentiating Eq. 2.2 and neglecting the higher order derivatives $dad b$, $dbdc$, $dadc$, and $dadbdc$, gives:

$$da/a + db/b + dc/c = d\epsilon_1 + d\epsilon_2 + d\epsilon_3 = 0\tag{2.3}$$

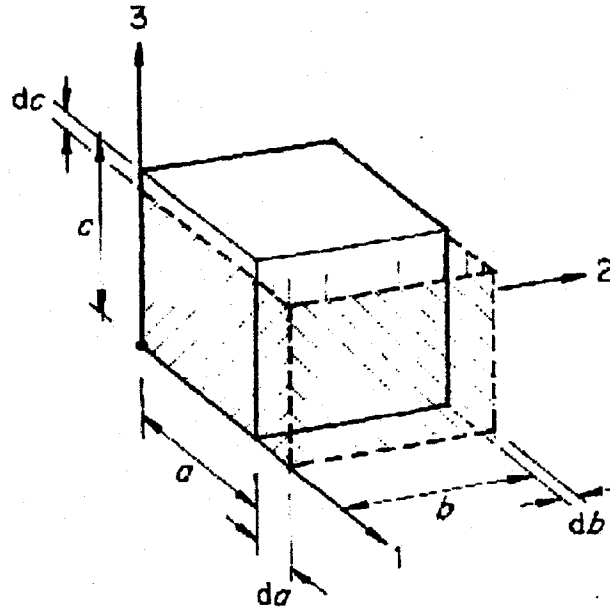


Figure 2.4. Incremental deformation of a principal element [3].

The principal strains in an incompressible material are usually plotted in the two-dimensional strain space [3] (Figure 2.5). According to the laws of pure, proportional deformation, the process in which $\epsilon_2 = \beta \epsilon_1$ is represented by a straight line of slope $1/\beta$, where β is the strain ratio. This diagram does not indicate the third principal strain (thickness strain). Figure 2.5 also illustrates the several modes of deformation in sheet metal forming operation, which are:

- a. Balanced biaxial: If $\beta = 1$, the circle increases uniformly in diameter indicating that the major and minor principal strains are equal. This process is also referred to as pure stretching.
- b. Plane strain: If $\beta = 0$, the circle elongates only in one direction. This indicates that the material undergoes deformation in the major strain direction with the minor strain being zero.
- c. Pure drawing: If $\beta = -1$, the circle extends in one direction and shrinks transversely which is exactly how the material behaves.

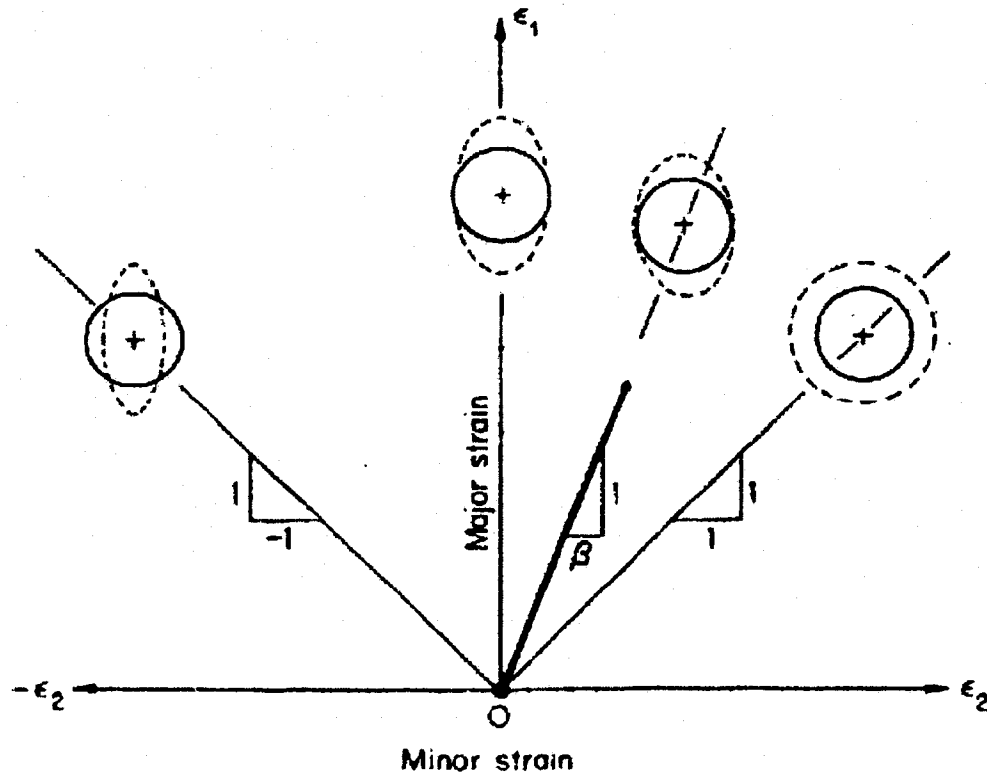


Figure 2.5. Graphical representation of deformations in the two-dimensional strain space [3].

2.2.1 Forming Limit Diagram

For any successful stamping operation, it becomes necessary to know the maximum allowable load that can be applied to a blank, without generating any failure. In a sheet forming operation, different deformation modes act simultaneously on the panel being formed. These modes, as discussed in the previous section are: pure drawing, plane strain and balanced-biaxial strain. The deformation is most likely to occur in the area undergoing a biaxial stretch which has a positive value for both the major and minor strains. Failure in such a stretching operation is generally characterized by the development of a localized neck on the surface. To understand this phenomenon, the concept of critical strain level (now formability limit) was introduced by Keeler [4] and Goodwin [5]. Keeler measured the two principal surface

strains at the onset of necking from a number of biaxial stretching experiments and plotted them as shown in Figure 2.6.

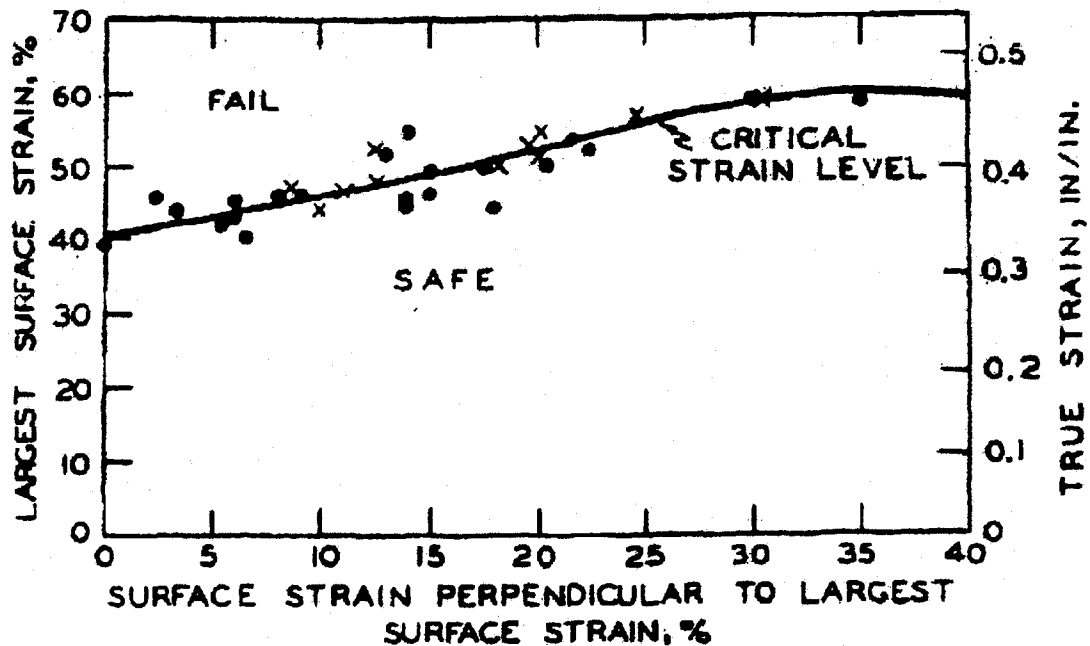


Figure 2.6. Keeler's concept of Formability Limit [4].

The curve that was drawn from the measured strains separated the failure and non-failure (safe) conditions and was labeled as the critical strain level. By using the above Figure 2.6 and measuring the strains on any stamping, the proximity of these strains to failure can be determined. However, this curve has limited practical applications as it cannot be used to predict the strains in the pure drawing and plane strain conditions. Goodwin [5] carried out various forming and tension tests to obtain failures that represented the pure drawing and plane strain conditions, i.e., a positive major strain value and a negative minor strain value. This relation between the negative minor strain and the positive major strain was shown as a band (Figure 2.7). The lower curves in the band were described as denoting the onset of localized thinning (necking), whereas the upper curves represented ultimate failure. This combined developed curve, called the "Keeler-Goodwin Curve", was found to give

the practical formability limit for different types of failures encountered in a press shop forming operation. The lower curves of the Keeler-Goodwin band were subsequently joined into one curve after some fine refinements to the curve shape on the left hand side [5, 7].

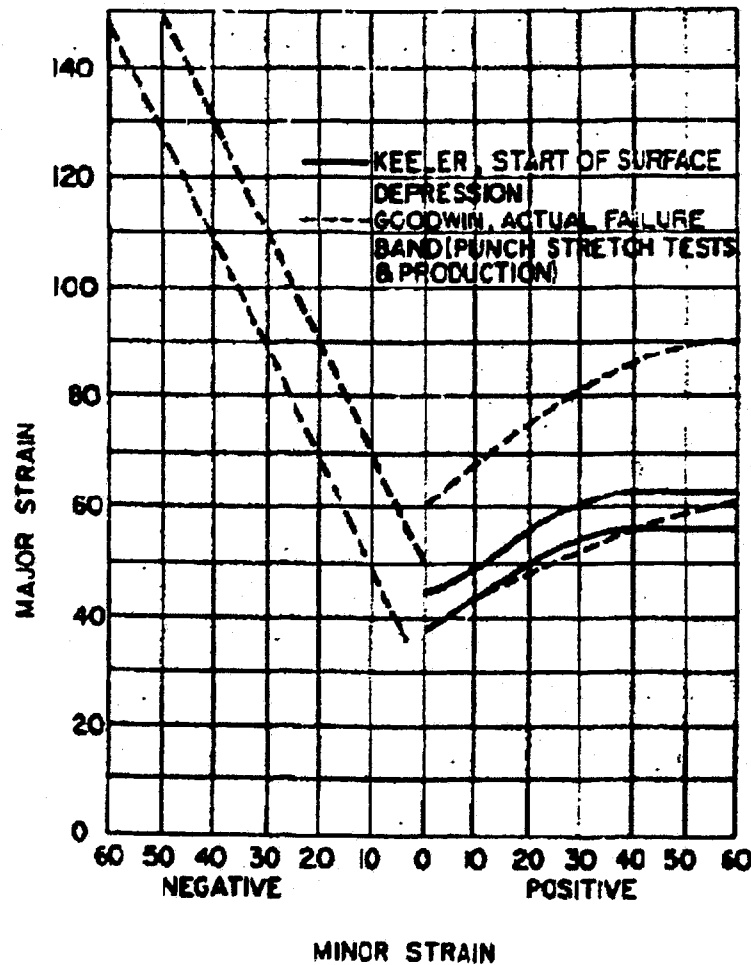


Figure 2.7. Keeler-Goodwin Curve—the first published full FLD [5].

It was further suggested by Raghavan *et al.* [7] that a safety factor or "marginal zone" of 10% strain below the modified Keeler-Goodwin curve be used to avoid the sporadic breakage due to the day-to-day variations in the stamping process

conditions. This FLD, shown in Figure 2.8, with the marginal zone, represents the standard method most commonly used today.

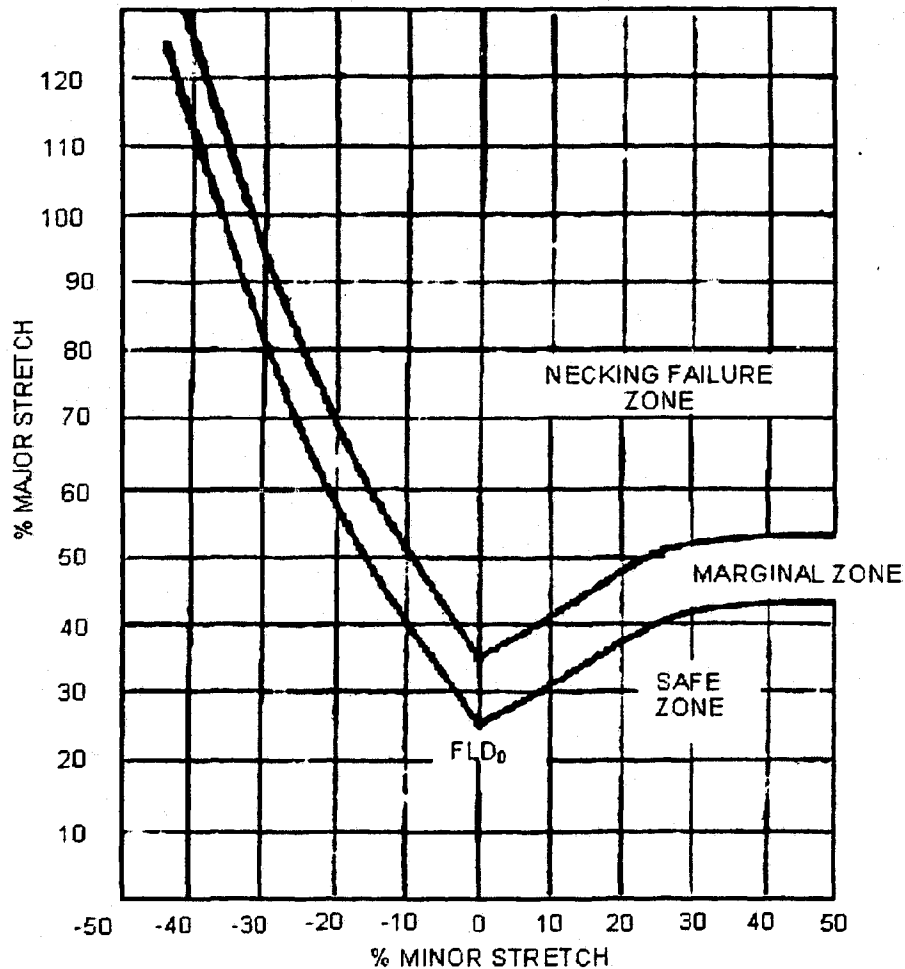


Figure 2.8. Standard FLD shape with a 10% marginal zone [7].

This initial concept of the FLD was designed for conventional low strength steels. However, it was realized that other grades of steel, such as the high strength steels, may have lower forming limits and that the sheet thickness can also influence the forming limits. Keeler and Brazier [8] established the following relationship among the position of the FLD along the major strain axis, the FLD_0 (major strain value

under plane strain having zero minor strain), the strain-hardening exponent (n-value), and the thickness of the sheet,

$$FLD_0 = a [23.3 + 14.1 t], \quad (2.4)$$

where, $a = \frac{n}{0.21}$, when $n \leq 0.21$,

and $a = 1$, when $n > 0.21$,

n = Strain-hardening exponent,

t = Material thickness in millimeters (mm).

This equation has been extensively used in the North American press shops to position the standard FLD along the major strain (y-axis) for all grades of steel [7, 8]. However, with the development of newer grades of steel, like the extra deep drawing quality (EDDQ) and interstitial free (IF) steels, having n-values higher than 0.21, the feasibility of Eq. 2.4 has been questioned, since it was suggested by some FLD users that the FLD_0 value continues to rise as the n-value increases beyond 0.21. Therefore, a recent modification to the standard method has been proposed by the North American Deep Drawing Research Group (NADDRG) [7], where the multiplying factor, a , used in the Keeler-Goodwin equation is changed to $n/0.21$, for all values of n . This modified NADDRG equation becomes,

$$FLD_0 = \frac{n}{0.21} (23.3 + 14.1 t). \quad (2.5)$$

2.2.2 Measurement of Forming Strains

As mentioned above, a stamping process is composed of various combinations of stretch and draw, to which bending, buckling and other complications are added. This leads to the development of non-uniform strains in the formed part. Thus, there will be regions of high strain as well as low strain, which may lead to wrinkling or

fracturing of the material. Keeler [4, 6] has discussed the necessity of developing a technique which could be quickly and accurately used to measure the strains developed in a blank during the forming process. Strain analysis by grid marking is a useful method, which has been used effectively to solve the above mentioned problems in metal forming [4]. After the sheet metal is deformed into the desired shape, the strain distribution can be seen and the critical areas of strain analyzed using the FLD to control the forming parameters.

Different types of grid systems can be used for accurately measuring the strain distributions. The most important feature for any grid system is the use of smaller grid spacings having a proper orientation [6]. The most commonly used pattern involves either 1 mm square grids or 2.5 mm radius circles as shown in Figure 2.9 [6]. Over a period of time, many methods have been developed for applying these grids on the surface of steel. The square grids were scribed on the surface of the steel using parallel lines. However, the scribe marks introduced stress concentrations which led to failures occurring along the scribe lines. Then an imprinting system was used which consisted of a rubber stamp and marking ink [6]. Resolution and accuracy of grids prepared in this manner were limited and the ink markings could be easily erased. The photochemical process developed was a very time consuming process and required a number of steps to be followed. Moreover, the grids were easily removed while rubbing over a die radius.

The most preferred and quick method which is currently used in the industry involves electrochemical etching of the grids on the steel surface. In this process, an electric stencil is placed on the cleaned blank. A felt pad soaked with electrolyte is placed on top of the blank and an electrode (flat or roller type) is placed above the felt pad [9].

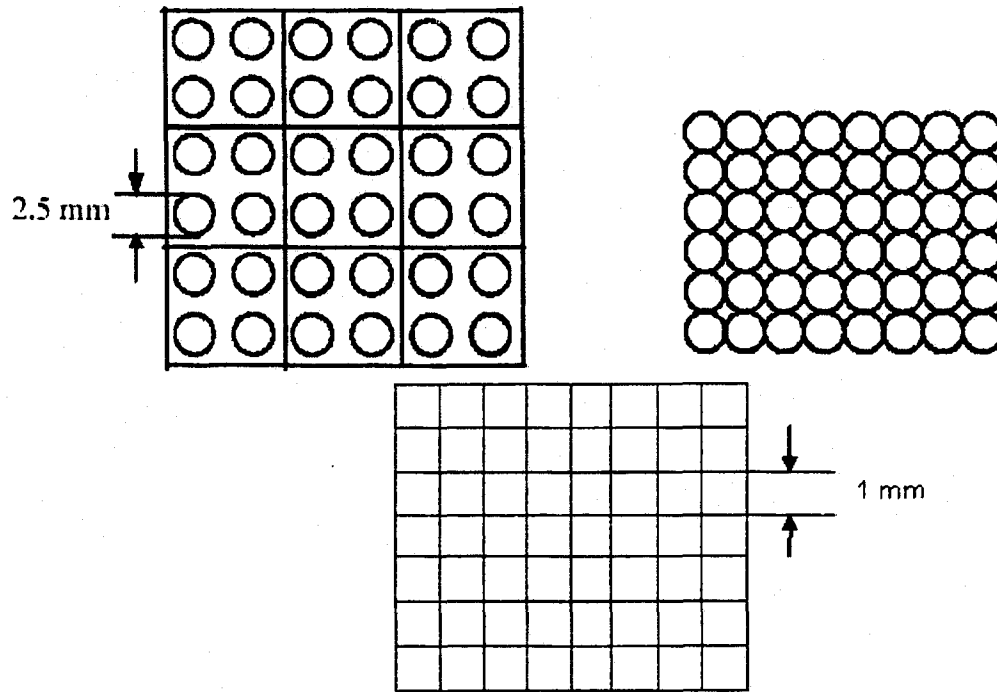


Figure 2.9. Commonly used grid patterns [6].

A wooden block is kept above as shown in Figure 2.10. Leads from a power source are attached to the electrode and the blank. The current applied varies depending on the stencil size and the line density. The pressure on the electrode squeezes the felt pad, which allows the electrolyte to pass through the stencil and to etch the grid pattern electrochemically on the blank surface. After etching, the blank is washed with a neutralizing solution.

Once the sheet metal is formed, the grids based on the initial marked pattern will either deform into ellipses or parallelograms of different sizes. For a circular grid pattern as shown in the Figure 2.11, the major and minor strains are calculated from the following formulae [10]:

$$\% \text{ Major strain} = \frac{\text{Major axis length} - \text{Original circle diameter}}{\text{Original circle diameter}} \times 100, \quad (2.6)$$

$$\% \text{ Minor strain} = \frac{\text{Minor axis length} - \text{Original circle diameter}}{\text{Original circle diameter}} \times 100. \quad (2.7)$$

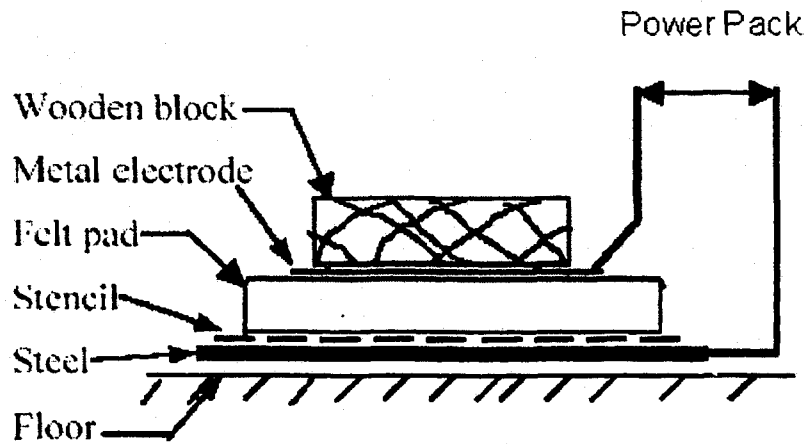


Figure 2.10. Set up for electrochemical marking [9].

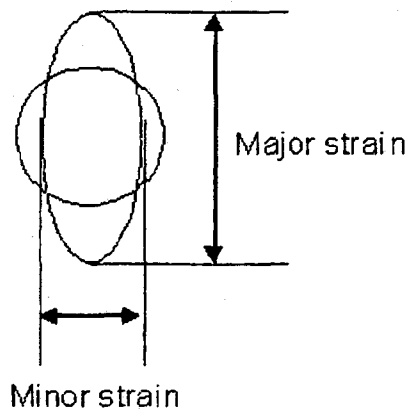


Figure 2.11. Deformed circular grid representing the major and minor strains [10].

The major and minor axis lengths can be measured using either dividers and a steel ruler or a mylar tape [2]. The mylar tape (Figure 2.12) has diverging lines scaled to read directly in percent strain. This scale is produced by photographic printing from a negative on to film. The scale is placed over the ellipse over a sharp radius and then

shifted until the diverging lines line up with the major axis of the ellipse. The scale is next turned 90 degrees to read the minor strain.

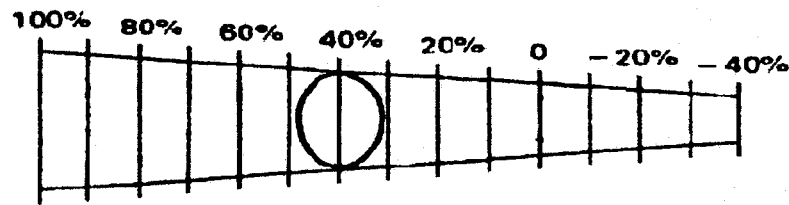


Figure 2.12. Mylar tape used for calculating the major and minor strains [2].

A more recent approach for measuring the strains involves the use of a traveling microscope. There are two right angled slides on which the work piece is mounted and positioned under the microscope. The cross-wire is aligned at one end and the measurement is taken. The cross-wire is then aligned on the other end by moving the work table and the measurement is taken. The difference between the two readings gives the absolute measurement. However, a grid analyzing system as shown in Figure 2.13 is the most widely used method for measuring the changes in the dimensions of the grids. This system uses a solid state digital array camera with a built-in light source, a computer, keyboard, and CRT display. The image of a given deformed circle is displayed on the CRT and a least squares curve fitting program selects the most suitable grid, which is displayed simultaneously [11]. The major and minor strains are then computed and displayed on the screen.

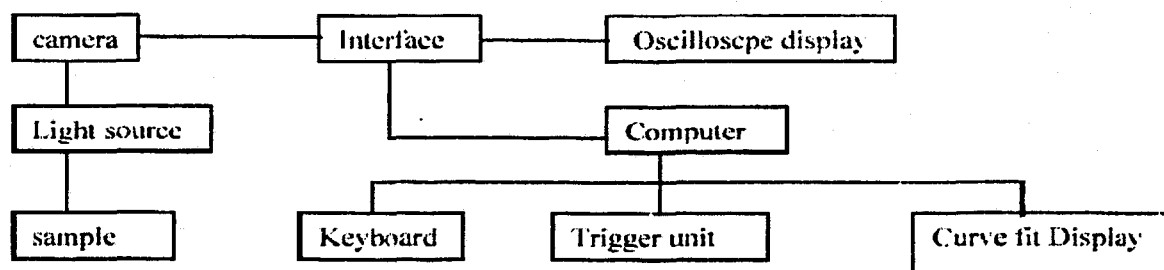


Figure 2.13. Grid analyzing system used for recording the forming strains [11].

2.2.3 Factors Affecting the Forming Process

Traditional evaluations of formability are based on basic tests which include the direct measurement of the mechanical properties of the material derived from a standard tensile test, such as yield strength, ultimate tensile strength, strain-hardening exponent (n-value), coefficient of anisotropy (r-value) and total elongation. The strain-hardening exponent (n-value) plays a significant role in evaluating the formability of sheet metals. The n-value describes the ability of the material to work harden or to uniformly distribute the deformation. A larger n-value means that the material will have greater uniform elongation and will resist localized deformation or necking. For any material, the higher the tensile/yield strength ratio, the higher the n-value [2].

The other factors affecting the strain distribution in any automotive stamping include the die geometry and lubrication. There has been a lot of work done [4, 6, 12, 13] on the effects of these factors as discussed below.

2.2.3.1 Material Properties

The formation of an automotive stamping involves complex forming processes like deep drawing (uniaxial tension), stretching operations under plane strain and bi-axial conditions and bending. The historical approach, while studying the effect of material properties on such a forming process, has been to subdivide the stamping into its component processes and study each process independently. Bending refers to the process by which a flat sheet of metal is transformed into a curved component. The deep drawing mode causes the material to undergo contraction in one direction and extension in another. The deep drawing limit of a material is greatly influenced by the coefficient of anisotropy (r-value), which is the measure of its resistance to thinning and can be obtained from a standard tensile test. The most widely used

forming process in automotive stampings is the stretching of sheet metal in plane strain and bi-axial conditions, over a rigid punch of fixed geometry. A large percentage of forming failures are associated with this kind of process [2, 4].

Keeler [4] conducted various laboratory tests to determine the influence of material properties on the strain distribution. He investigated and compared the strain distribution for brass, steel and aluminum in annealed condition by stretching them over a 101.6 mm (4 in) diameter hemispherical punch. For a more meaningful comparison for automotive purposes, Keeler [4] analyzed the strain distributions in two different types of steels, steel A and steel B, having similar thickness in a real stamping process. The critical strain level for this particular component was identified as 45% major strain. While forming the steels, it was seen that steel A, reached the critical level of 45% major strain long before the part was formed to the final shape. At this point, steel B was strained only 34% major strain. Analysis of the steel properties revealed that the n -value for steel A was 0.22 compared to 0.19 for steel B. Based on these tests, Keeler concluded that the material having the most uniform strain distribution, i.e., a higher n -value, can successfully accomplish a stamping operation.

2.2.3.2 Die Geometry

The strain distribution in an automotive stamping is greatly influenced by the die geometry. Stamping die sets consist of a punch and a die that are forced together by the action of the press to form the metal sheet into the desired shape. Additional items like binders and draw beads help in controlling the material flow during forming [2]. Figure 2.14 illustrates a simple die geometry. The punch radius, the die radius and the draw beads should be carefully determined based on the part geometry. A large and smooth punch surface (Figure 2.14) distributes the strain over a greater area and increases the permissible depth before failure. The die and punch should

be thoroughly examined for surface defects and material pick-up from previous runs. Careful measurements are often required to detect any misalignment which may lead to serious forming failures.

The laboratory test for evaluating the formability of sheet metal is based on a simple die design which consists of a 101.6 mm (4 in) hemispherical punch with a circular draw bead [14] as shown in Figure 2.15.

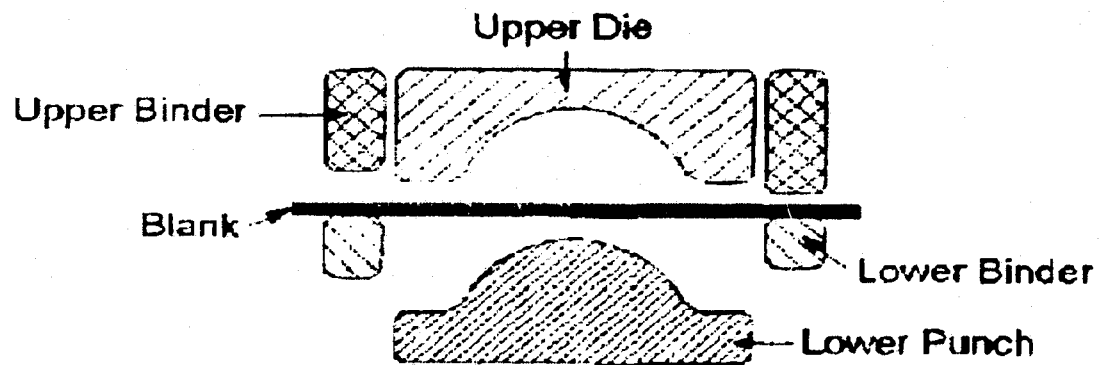


Figure 2.14. Die geometry [2].

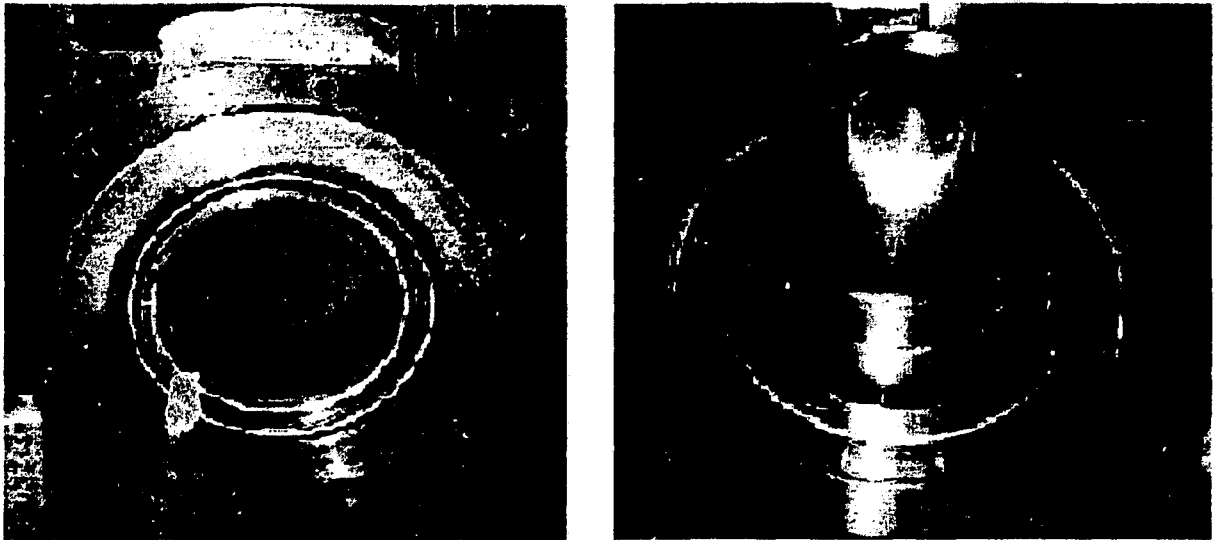


Figure 2.15. Draw bead and hemispherical punch used in laboratory experiments.

2.2.3.3 Lubrication

Lubricants are used to control or facilitate metal flow over punches and into die cavities. The degree and type of lubrication can strongly influence the strain distribution in a stamping process. The expanded growth of zinc coated (galvanized) steel sheets for automotive stampings has triggered various studies [12, 13] about the effect of interface friction with lubricants, die materials and temperature. The highly localized strain distribution reduces overall formability of the material. Also, the interface friction may change the strain path during forming and the final strain state in the part. Conventionally, the interface friction is represented by the coefficient of friction, which can be measured via different friction tests.

Keeler *et al.* [13] and Shi and Meuleman [12] have reported that the effect of lubricant is different among different types of materials or even for the same material from different suppliers. To analyze this effect, the draw bead simulator test was designed which allows the material to be pulled over a set of roller and fixed beads as shown in Figure 2.16. The data generated from this test is used to determine the friction force and finally calculate the coefficient of friction.

A series of such tests was conducted by Shi and Meuleman [12] on different types of lubricants and automotive steels from different producers. A mix of bare, electro-galvanized and hot-dip galvanized steels was tested with oil based, water based and a dry film lubricant. It was observed that the bare steels showed the least sensitivity to the characteristics of the lubricants used. This was attributed to the uniform surface characteristics generated during the processing of bare steel. On the other hand, galvanized steels that have a different surface topography than the bare or uncoated steels were found to be more sensitive to the lubricant used. Therefore, the capability of different lubricants to mask these different surfaces becomes more important. In terms of formability, the ideal press shop lubricant should be robust and

have a constant and low coefficient of friction for the widest range of materials being used [12].

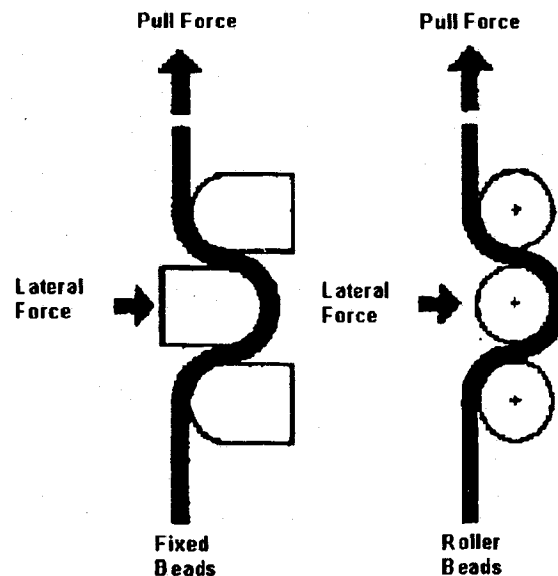


Figure 2.16. Draw bead simulator [12].

2.3 Fatigue of Formed Components

The structural sheet components used in the automobile industry are susceptible to fatigue in certain areas where high stresses occur due to the sudden change in the profile and geometry of the component. For a formed component, there are several factors that govern the fatigue life. The forming properties of the material, the layout of the forming tool, the blank holder forces, lubrication and surface properties like roughness and protective coatings are some of the factors that affect the fatigue life [15]. Also, the residual stresses, degree of prestraining, localized stress concentration and the strain path play a vital role in determining the fatigue life of the material being formed [15].

Fatigue failures generally occur at local areas of high stress concentration due to the abrupt change in geometry when any material is subjected to a repetitive or fluctuating stress (cyclic loading). The stress level at which fatigue failure occurs is

much lower than that required to cause fracture when a uniform load is applied [16]. For example, sharp press radii in combination with a reduction in the thickness of the sheet may lead to severe stress concentration at that point. This kind of failure is sudden and occurs without any warning.

A fatigue failure is generally recognized from the appearance of the fracture surface, which generally has a smooth region due to the rubbing action as the crack propagates and a rough region, where the material fails in a ductile manner as shown in Figure 2.17. The progress of the fracture is indicated by a series of rings, also called as beach marks, moving inwards from the point where the failure initiated [16].

In general, a fatigue failure occurs due to the initiation and growth of cracks which are very fine and difficult to detect. Once a large area is occupied by the cracks, the load bearing area gets reduced and sudden failure occurs without any notice [16].

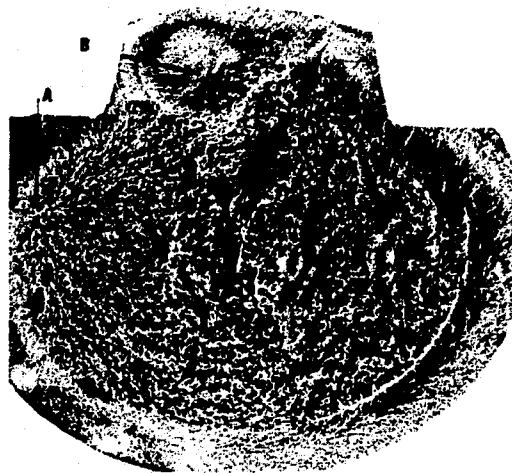


Figure 2.17. Features of a fatigue fracture—A and B are the failure initiation points [17].

The formed components in service are generally exposed to repeated stress cycles in which both the maximum and minimum stresses (σ_{\max} and σ_{\min} , respectively) are in tension [15]. The basic method of presenting engineering fatigue data is by means

of the S-N curve [16], a plot of stress S and the number of cycles to failure N , as shown in Figure 2.18. Unless otherwise indicated, N is taken as the number of cycles of stress to cause complete fracture of the specimen. The value of stress that is plotted can be σ_a (stress amplitude), σ_{\max} or σ_{\min} (Figure 2.19). The S-N relationship is determined for a specified value of mean stress σ_m , or stress ratio R [16]. The number of cycles of stress which a metal can endure before failure increases with decreasing stress amplitude. Fatigue tests are usually carried out for 10^7 cycles, beyond which the samples are considered as a run-out, i.e., no failure occurs at the applied stress amplitude. The highest stress level at which the run-out (non-failure) is obtained is thus taken as the fatigue limit. Below this value of stress level, the material can be considered to endure an infinite number of cycles without failure and the S-N curve becomes horizontal (Figure 2.18) [16].

The fatigue limit is frequently correlated with tensile properties. For steels, the fatigue limit is approximately 50% of the ultimate tensile strength (UTS). The ratio of the fatigue limit to the tensile strength is called the fatigue ratio and is often used to compare the fatigue properties of different materials.

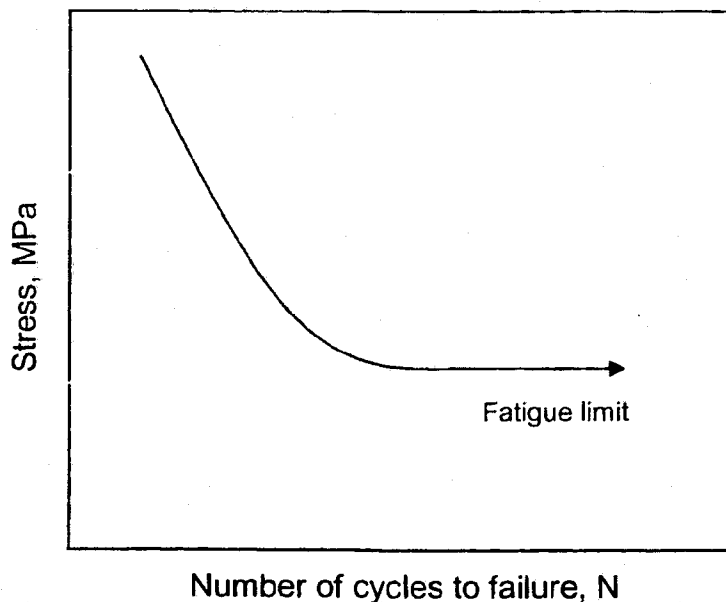


Figure 2.18. A schematic S-N curve showing the fatigue limit for steels.

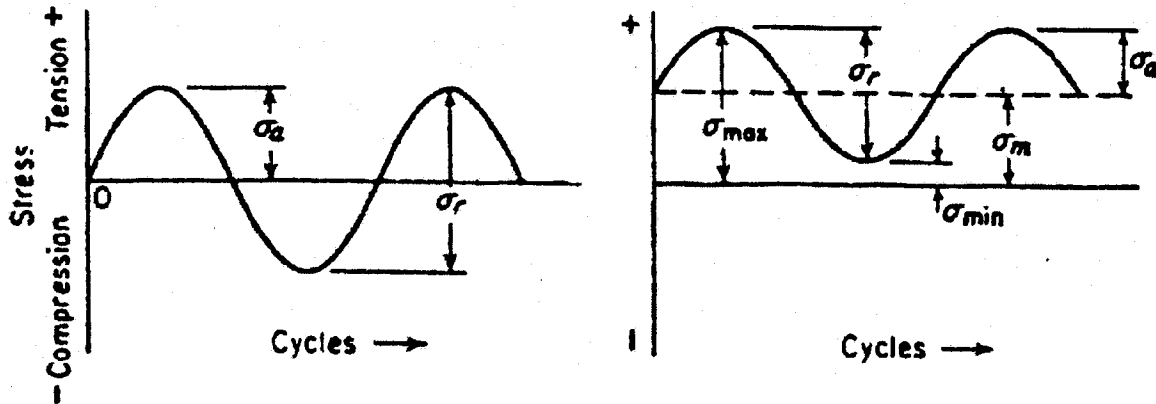


Figure 2.19. Typical fatigue stress cycles [16].

2.4 Recent Studies on Formability of Tailor Welded Blanks

The use of newer grades of steels like the interstitial free (IF), dual phase (DP), transformation induced plasticity (TRIP) and high strength low alloy (HSLA) for TWB applications has raised various challenges, including the prediction and evaluation of the performance of these TWBs in forming and other structural properties like fatigue resistance. Many reports have been documented, which discuss the forming behavior of TWBs of conventional steels.

Shi *et al.* [18], in their work on drawing quality steel, have reported different modes of forming failure for TWBs. In a similar thickness TWB combination (0.8-0.8 mm), the failure occurs in a direction perpendicular to the weld bead. In the case of a dissimilar thickness TWB (0.8-1.8 mm), failure occurs in the thinner material and is oriented parallel to the weld bead as shown in Figure 2.20. They found that the weld bead usually undergoes uni-directional deformation along the welding line and hence the positioning of the weld in the sheet blank should be carefully selected. The suggested optimum position is to place the weld perpendicular to the major strain direction. To obtain the maximum formability performance of TWBs,

deformation in the thinner or lower strength material should be minimized. They have also reported that the forming limit of a TWB depends on the specific welding set-up conditions and the material used. The maximum formability can be achieved by optimizing welding parameters and/or by using more formable steels such as IF and very low carbon steels, which result in a more formable weld.

Chan *et al.* [19] reported the effect of varying thicknesses on the formability of the TWBs. An Nd:YAG laser was used for butt welding cold rolled sheets. Their different thickness combinations were 0.5-1.0 mm, 0.6-1.0 mm and 0.8-1.0 mm, having a given carbon content of 0.12%. They carried out Swift round-bottom tests which are similar to hemispherical punch (Figure 2.15) tests and have a round punch of 50 mm diameter with a blank holding force of 30 kN. The weld bead in the forming tests was oriented perpendicular to the major strain axis. They evaluated the performance of the TWBs based on the thickness ratio by measuring the limiting dome heights (LDH) to failure. Limiting dome height represents the maximum height (h in Figure 2.21) to which a sheet specimen can stretch at the onset of necking/failure. They reported that the lower the thickness ratio of the TWBs, the higher the LDH. While comparing the FLD_0 values of the TWBs, they found that the TWBs having the highest thickness ratio yield the lowest FLD_0 value. The FLD_0 value of the TWBs was reported to be lower than the FLD_0 of the thicker (1.0 mm) base metal as seen in Figure 2.22.

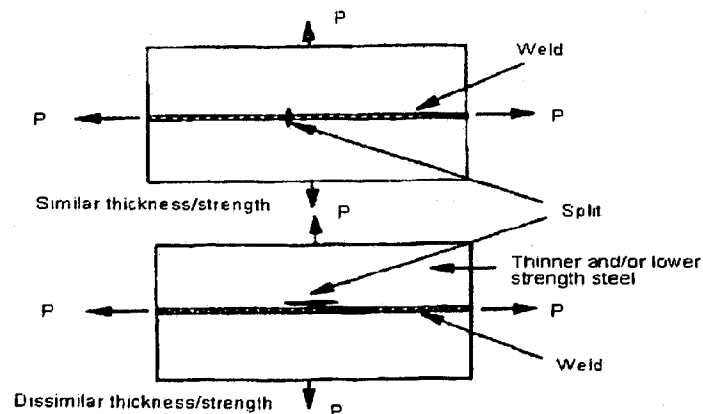


Figure 2.20. Two types of splitting in forming of TWBs [18].

Chan *et al.* [20] also carried out Swift bottom tests on TWBs of JIS-3141 (0.04% carbon) cold rolled sheets. The TWBs had different thickness combinations of 0.7-0.8 mm, 0.7-1.0 mm and 0.8-1.0 mm, welded by an Nd:YAG laser. They used 2 mm diameter grids for measuring the major and minor strains. The weld bead was once again oriented perpendicular to the major strain axis. The forming failure was reported to occur in the thinner section of the TWB and in a direction parallel to the weld bead. However, it was reported that with the variation in width of the specimens, the distance of the failure from the weld bead also varied. With the increase in the width, the failure was observed to be closer to the weld bead. They also observed that as the thickness ratio of the TWBs increased, the LDH to failure decreased as shown in Table 2.1.

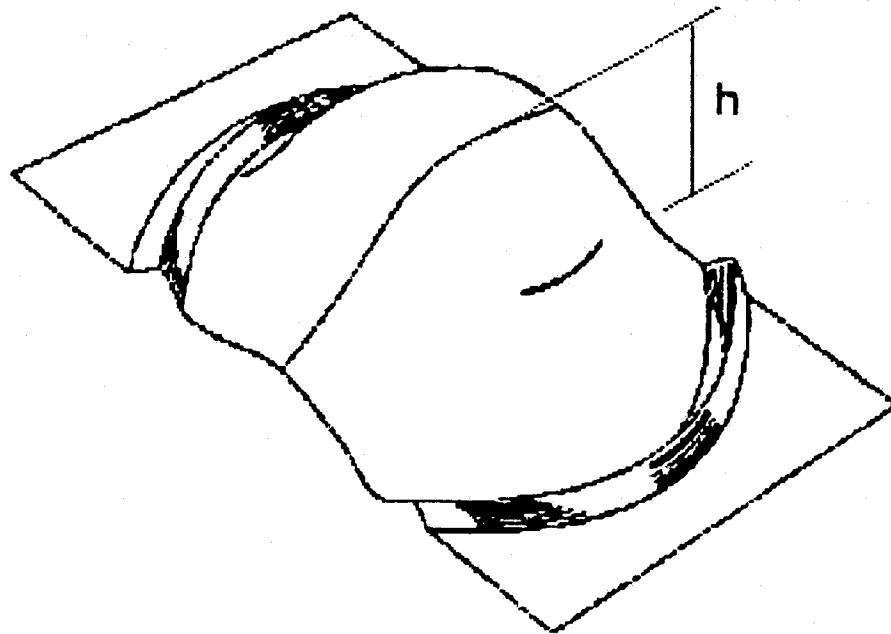


Figure 2.21. Specimen showing the limiting dome height to failure [12].

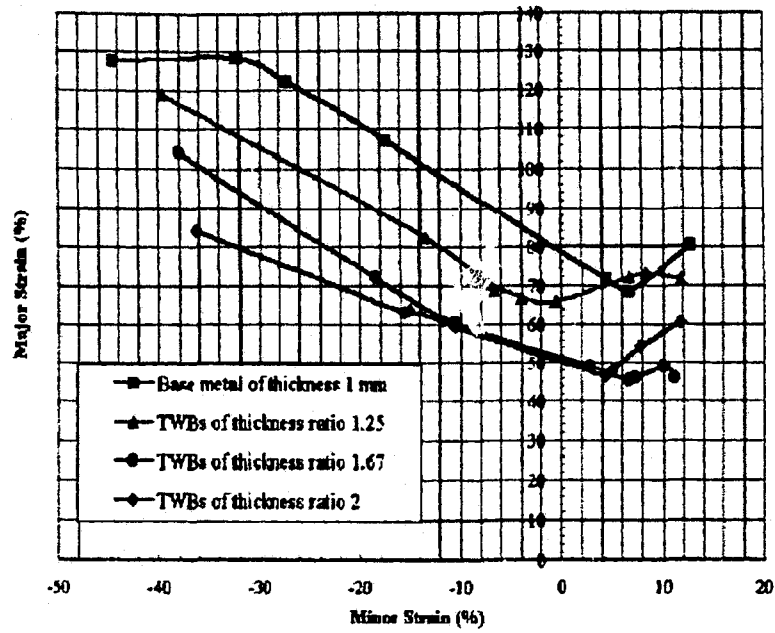


Figure 2.22. Comparing the FLDs of different thickness TWBs with the base metal of thickness 1mm [19].

Table 2.1. Comparison of failure height from the base and strain values of specimens with same deformation mode [20].

Specimen (Same deformation mode)	Failure height from the base (mm)	Major strain (%)	Minor strain (%)
TWB 0.7 mm/1.0 mm	16.88	80	-19.44
TWB 0.8 mm/1.0 mm	18.12	82.78	-21.67
TWB 0.7 mm/0.8 mm	21.46	92.23	-28.33
Base Metal 0.7 mm	22.38	101.11	-30

In the work by Ghoo *et al.* [21], the concept of a new forming limit diagram for TWBs was introduced (Figure 2.23). They carried out hemispherical dome tests on different widths of similar (0.8-0.8 mm) and dissimilar thickness (0.8-1.5 mm) TWBs. The weld bead was at the centre of the punch face and oriented parallel to the major strain direction. With the use of 2.54 mm (1 in) square grids, they measured the strains in the weld zone by generating a failure perpendicular to the weld bead. It was observed (Figure 2.23) that the FLD of the weld zone in both similar and dissimilar thickness TWBs was lower than the FLD of the base metals. Also, the dome height at fracture for similar thickness TWBs was found to be lower than the dome height for dissimilar ones.

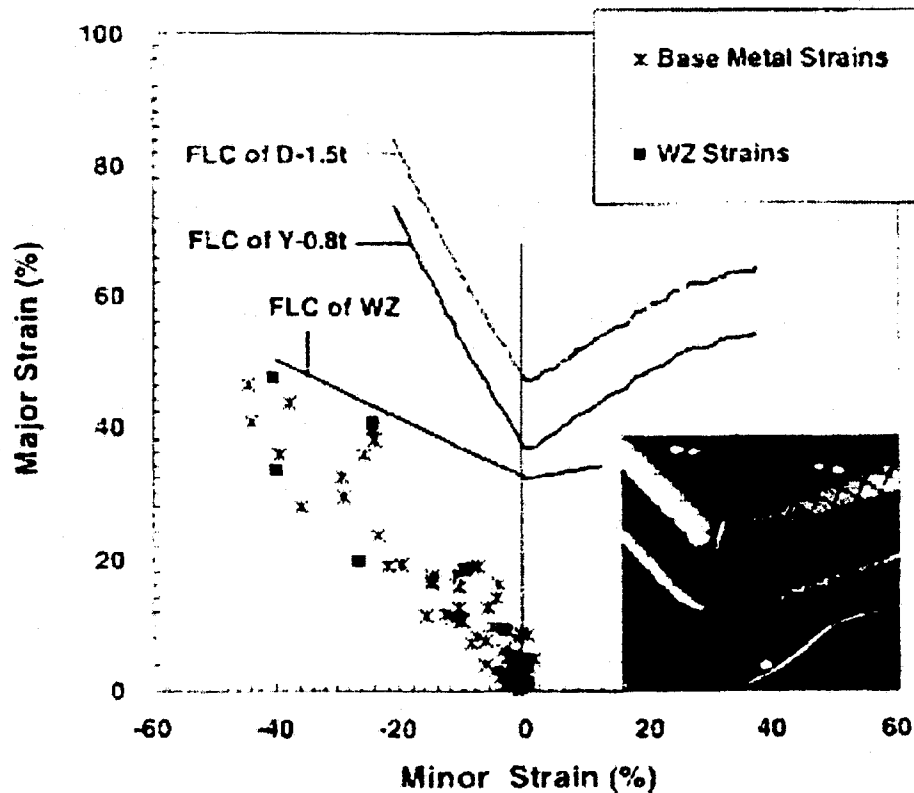


Figure 2.23. Concept of new FLD for a different thickness TWB [21].

2.5 Recent Studies on Fatigue of Tailor Welded Blanks

The auto/steel partnership (A/SP), in one of their reports [1], has remarked that the failure of the TWBs under cyclic loading or fatigue is a serious problem for the structural components. The high cycle fatigue strength of a material depends on surface conditions, residual tensile stresses and hardness. With the use of the laser welding process, residual tensile stresses and other welding defects can be introduced into a material. A/SP has identified this as an area that requires further research, as there are only limited data in this respect.

Wang and Ewing [22] have compared the fatigue strength of laser welds with that of resistance spot welds of similar thickness (0.76 mm) bare SAE 1008 grade of steel. The laser welds were oriented in a direction, both, parallel and perpendicular to the loading direction. The fatigue strength of the laser welded blank that was oriented perpendicular to the loading direction gave the highest fatigue resistance as shown in Figure 2.24. This was mainly attributed to the high stress intensity introduced at the circumference of the spot weld due to its geometry.

Lazzarin *et al.* [23], while evaluating different welding processes, determined the fatigue strengths of similar thickness (1.5 mm) laser welded sheets in both bare and hot dip galvanized conditions. The weld bead was oriented perpendicular to the loading direction. They concluded that the fatigue strengths of both the combinations were similar.

Rhee *et al.* [24] evaluated the fatigue behavior of similar (0.9 mm) and dissimilar (0.9-2.0 mm) thickness laser welded sheets of bare cold rolled steel (0.016% carbon). The weld bead was oriented both parallel and perpendicular to the loading direction. Both similar (Type B) and dissimilar (Type D) thickness specimens with weld bead being perpendicular to the loading direction showed similar fatigue

strengths as seen in Figure 2.25. The fatigue crack initiated in the base metal and the final fracture also occurred in the base metal.

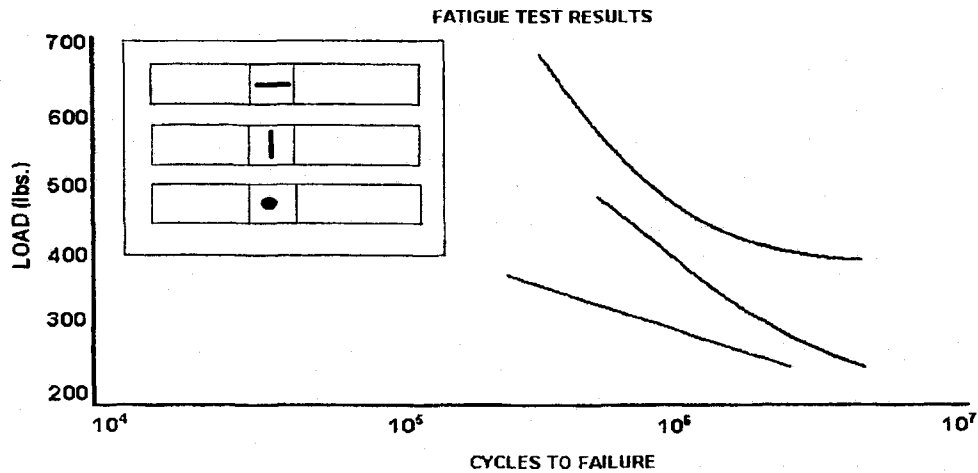


Figure 2.24. Fatigue test results for laser and spot welds [22].

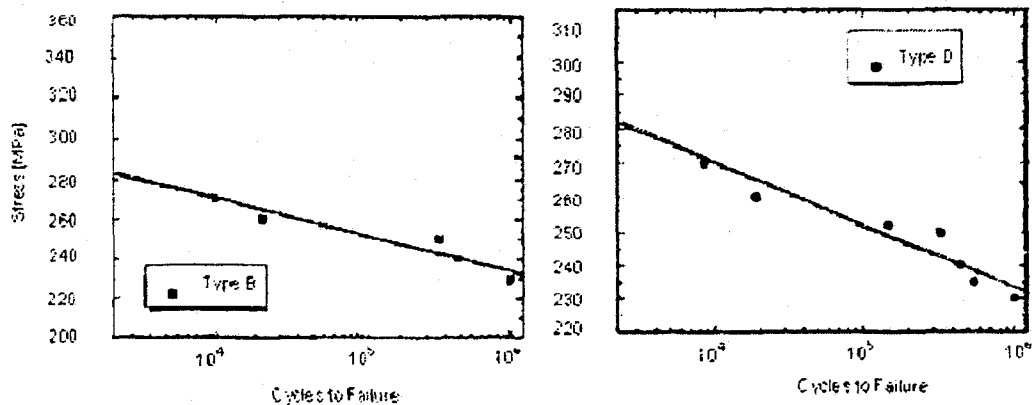


Figure 2.25. Effect of loading direction on fatigue strength for welded structure [24].

Oh *et al.* [25] reported lower fatigue strengths for dissimilar thickness sheets in their work on similar (0.9 mm) and dissimilar (0.9-2.0 mm) thickness laser welded sheets with weld oriented both parallel and perpendicular to the loading direction. This was attributed to the stress concentration induced by the discontinuous face. Lee *et al.* [26] evaluated the fatigue strengths for dissimilar thickness (0.7-1.6 mm) tailor

welded blanks. They compared the laser welding process with the mash seam welding process and found that laser welded blanks achieved a higher stress level (Figure 2.26). The mash seam welds had a greater notch effect and thus lower fatigue strength. Aristotile and Fersini [27] evaluated the fatigue strength of a production part that was formed out of a laser welded blank. The fracture was found to occur at locations having clamping holes away from the weld bead.

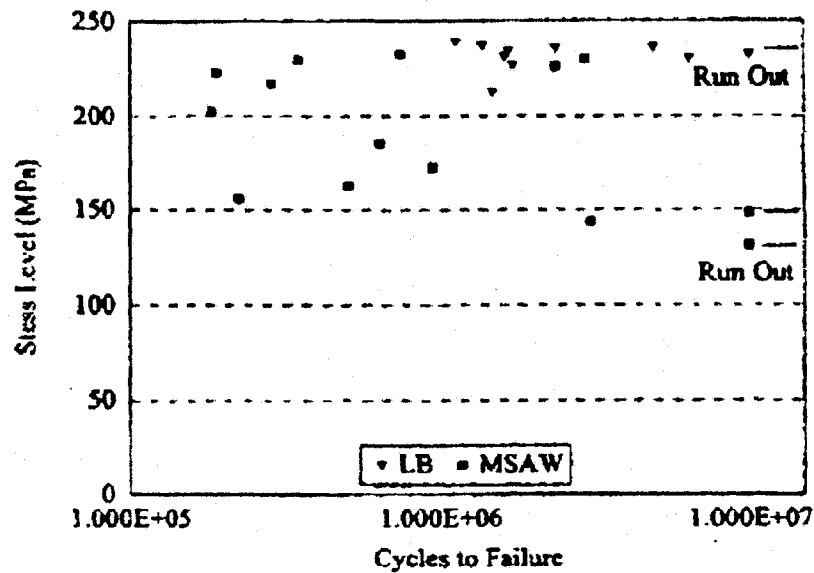


Figure 2.26. Effect of welding process on fatigue strength [26].

2.6 Objectives of Research

As seen from the above literature review, most of the reported work on formability [18-21] and fatigue [22-28] of TWBs is on conventional low carbon steels. Moreover, the formability of TWBs has been analyzed based on the limiting dome heights to failure. Extensive experimental data for the FLD_0 values of TWBs consisting of newer grades of steel cannot be found in the published literature. The effects of material properties like the strain-hardening exponent (n -value) and the thickness of the individual sheets on determining the FLD_0 values have not been investigated.

Previous work in fatigue basically analyzed the behavior of similar thickness TWBs or just one combination of TWB consisting of different thickness materials. No comparison or benchmarking regarding the fracture mechanisms has been reported for different TWBs consisting of newer developed grades in both galvanized (zinc coated) and bare (uncoated) conditions.

Therefore in this work, the forming behavior and fatigue strength characteristics of production CO₂ laser welded TWBs, composed of galvanized interstitial free and very low carbon steels, with different thickness combinations and different compositions are addressed. Limiting dome height (forming) tests were carried out and the FLD₀ values for the TWBs were determined both analytically and experimentally. The fatigue strength of the TWBs was compared to the base metal, and the fracture mechanisms were examined using scanning electron microscopy (SEM), coupled with EDS analysis.

Chapter 3

Experimental Procedure

3.1 Materials

The materials selected in this study were interstitial free (annealed-and hot dip galvanized) and very low carbon steel sheets (cold rolled and annealed). The selection was made from a lot used for actual production parts which were laser butt-welded. The chemical composition of the test materials is listed in Table 3.1. Three different combinations of TWBs were identified as GMX, W-Car and MC-DI based on the part name.

- GMX has the minimum difference in the thickness and the maximum difference in the yield strength of the two sheets.
- W-Car has the minimum difference in the yield strength of the two sheets.
- MC-DI has the maximum difference in the thickness of the two sheets.

Details of the differences in the physical characteristics of the TWBs are summarized in Table 3.2. One of the base metals, identified as BM, was selected for comparing the fatigue strength of the TWBs. As seen from Table 3.2, the thickness of the individual sheet metals in the TWBs ranges from a minimum of 0.75 mm to a maximum of 2.0 mm, the average of which is about 1.5 mm, and the BM of 1.5 mm thickness was hence selected in the present work.

Table 3.1. Chemical composition of the materials.

I.D.	Material grade	Sheet thickness (mm)	Composition						
			% C	% Mn	% P	% S	% Si	% Al	% N
GMX	Very low	1.50*	0.035	0.256	0.006	0.011	0.015	0.048	0.029
	carbon steels	0.90	0.050	0.271	0.009	0.011	0.009	0.050	0.006
W-Car	Interstitial	1.67	0.001	0.100	0.007	0.005	0.008	0.055	0.003
	free steels	0.75	0.001	0.120	0.014	0.010	0.005	0.029	0.002
MC-DI	Interstitial	2.00	0.003	0.180	0.005	0.004	0.009	0.051	-
	free steels	0.80	0.003	0.190	0.006	0.008	0.008	0.053	-

* The base metal (BM) has the same chemical composition as 1.5 mm sheet metal.

Table 3.2. Physical parameters of the tailor welded blanks.

I. D.	Material grade	Zinc coating-weight (gm/gm)	Thickness combination (mm-mm)	Difference in thickness (mm)	Difference in yield strength (MPa)
GMX	Very low	Uncoated	1.50-0.90	0.6	29
	carbon steels				
W-Car	Interstitial	70 / 70	1.67-0.75	0.92	1
	free steels				
MC-DI	Interstitial	70 / 70	2.00-0.80	1.2	9
	free steels				

3.2 Sample Preparation and Testing

3.2.1 Laser Welding Parameters

The TWBs were received from Powerlasers Limited, Concord, Canada. A CO₂ laser, without any filler metal, was used to butt-weld the TWBs. The laser welding parameters for this production run are given in Table 3.3. The shield gas used was helium and the focal length was 200 mm. All of the parameters provide consistent and sound welds.

Table 3.3. Laser welding parameters.

Process parameters	GMX	W-Car	MC-DI
Velocity	7.5 m/min	7 – 8 m/min	7 – 8 m/min
Power	100% of 8 kW	80% of 12 kW	100% of 8 kW
Shield gas flow rate	70-80 liters/min	60 liters/min	70-80 liters/min

3.2.2 Formability Tests and Strain Measurement

Prior to the forming tests, the welded blanks were etched with 1 mm square grids using the electrochemical etching technique discussed in section 2.2.2. The equipment, cleanser, electrolyte and the neutralizing agent (GMK Marking Kit) used were provided by The Lectroetch Company, OH, USA. The electrolyte was LNC-3, the cleanser used was soap based degreaser and the neutralizing agent was methanol [9].

The limiting dome height (forming) tests were carried out on an MTS 866.02 formability press, as shown in Figure 3.1. The weld bead was oriented at the centre of a 101.6 mm (4.0 in) hemispherical punch (Figure 3.2), in a direction perpendicular to both the principal strain and rolling directions. The upper and lower dies had a

bead diameter of 254 mm (10 in). A clamping force of 135 kN was used to secure the test specimen. The tests were performed according to ASTM E643-84 standards [14]. While performing the experiment, a practical difficulty of controlling and stopping the test at the point of necking was encountered. Thus both necking and fracture, as shown in Figure 3.3, were accepted as the criterion for failure for all the stretch dome tests, which has also been reported by Chan *et al.* [19]. The lubrication between the punch face and the TWB surface was provided by a light coating of mill oil (Quaker Lerrocote 61 MAL-HCL-1G), followed by a 0.05 mm plastic sheet and a 6.35 mm (0.25 in) rubber puck (Figure 3.4). Shims or circular rings, as shown in Figure 3.4, were used to compensate for the variation in the thickness of the TWBs during clamping in-between the die beads. The etching and forming tests were carried out at Dofasco's research and development facility.

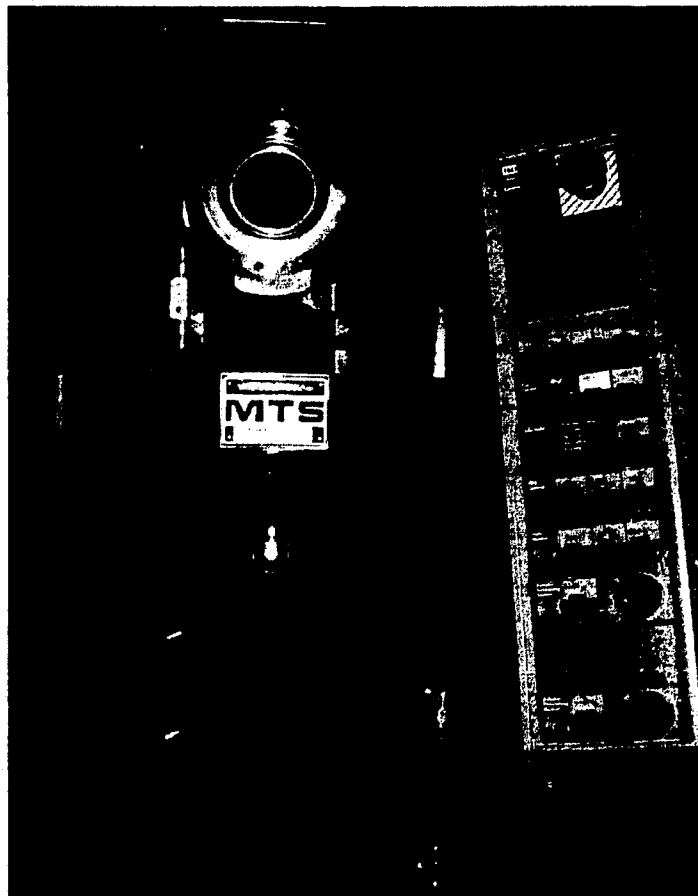


Figure 3.1. MTS 866.02 formability press.

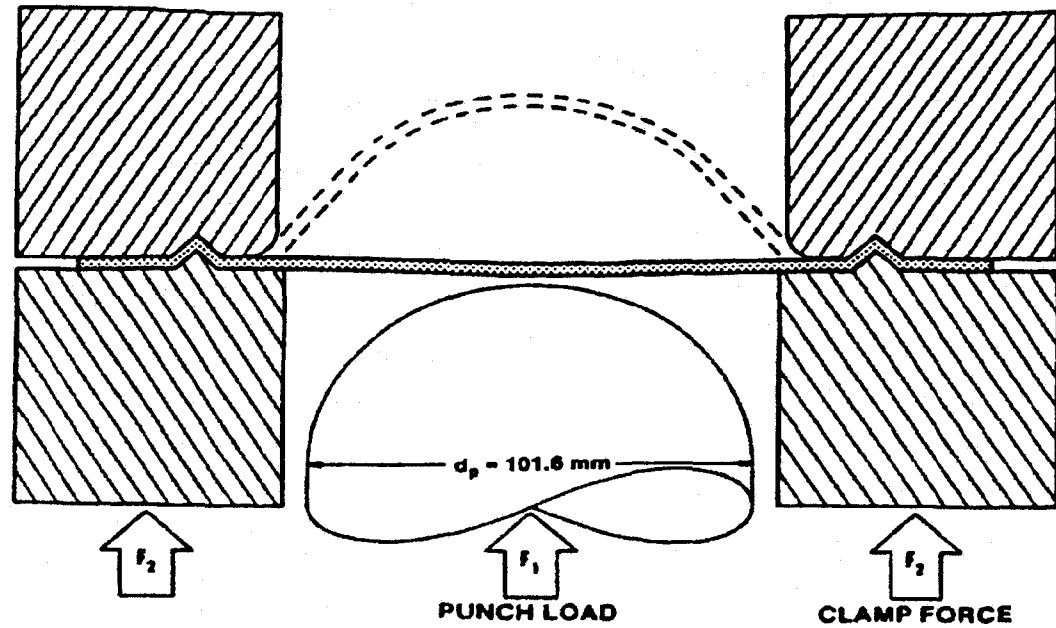


Figure 3.2. Hemispherical punch used for the forming tests [7].

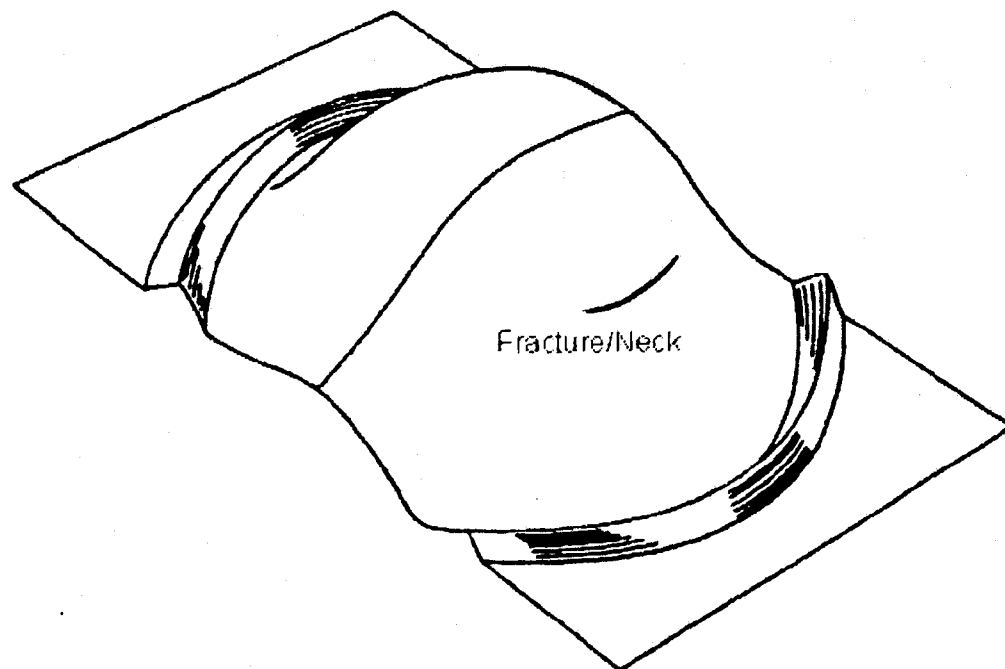


Figure 3.3. Formed specimen showing fracture/necking as the failure criterion [12].

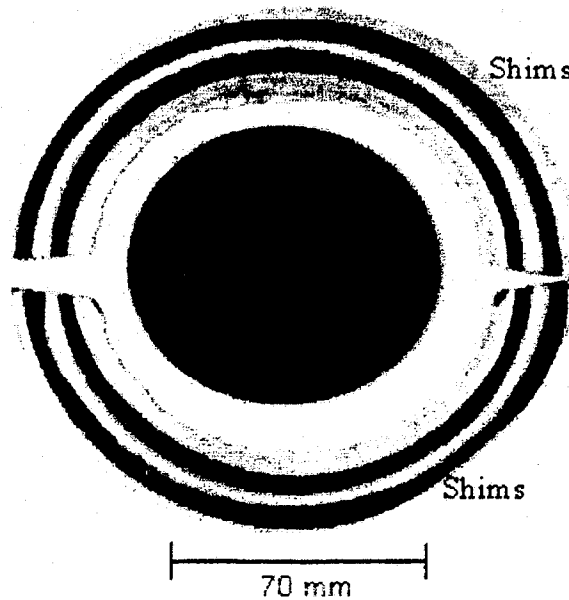


Figure 3.4. Shims and rubber puck used for forming tests.

In order to develop a comprehensive FLD for the TWBs, a series of rectangular specimens with a constant length of 203.2 mm (8.0 in) and varying widths of 25.4–203.2 mm (1.0–8.0 in) were tested as per the ASTM E2218 procedures [10]. Also, a number of different square grids (~10) were measured on each of the different width specimens to record the data for determining the different levels of major and minor strains in both safe and failed regions on the FLD. The narrower width specimen (25.4–101.6 mm) yielded the strain states on the left-hand side of the FLD. The specimen width of 101.6–152.4 mm yielded a strain state in the middle region representing plane strain condition. The right-hand side of the FLD, which accounts for the balanced bi-axial stretch, was represented by the specimens ranging from 152.4–203.2 mm. Figure 3.5 shows various widths superimposed on an FLD.

After the forming tests, the amount of deformation in the welded blanks was measured to calculate the major and minor strains. This was achieved by the use of a square grid analyzing (SGA) system manufactured by FMTI Systems Inc., Hamilton, ON, Canada. This system consists of a CCD camera (Model 100A) with a

combination of different lenses for capturing the picture of the deformed grids and square grid analysis software-version 5.31 for calculating the engineering strains from the deformed grids. The tests were carried out at Dofasco.

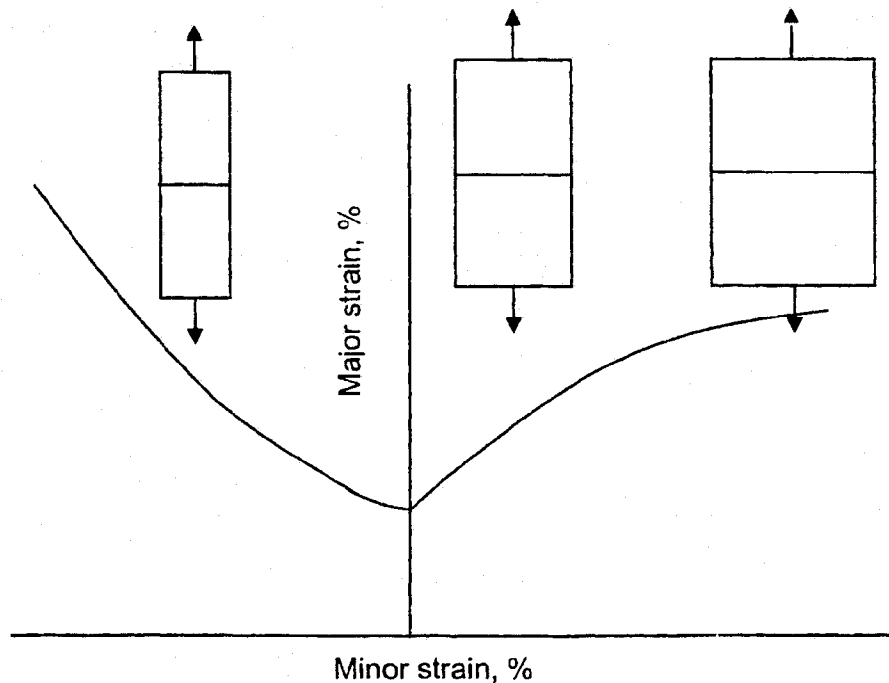


Figure 3.5. Specimen widths superimposed on a forming limit diagram.

As recommended by the manufacturer, the system was calibrated by measuring the originally etched square grids at five different locations prior to forming tests. This minimized the error in strain measurement to as low as 0.5%. The failed and non-failed (safe) regions on the formed specimens were identified on the basis of the rule of thumb commonly used in the industry. The grids which are immediately adjacent to the fracture or necked region correspond to the strain in the necked region and the grids which are about 5 mm away from the neck/fracture are considered to be in the safe region. Once these regions are identified, the CCD camera is used to manually locate a single deformed grid. After the grid has been captured, as shown

in Figure 3.6, the SGA software calculates and displays the major and minor strains (Figure 3.7). As seen in Figure 3.7, the dark circular points represent the strain corresponding to the necked region and the lighter points correspond to the strain in the safe zone. (These points appeared as red (necked) and green (safe) on the computer screen.)

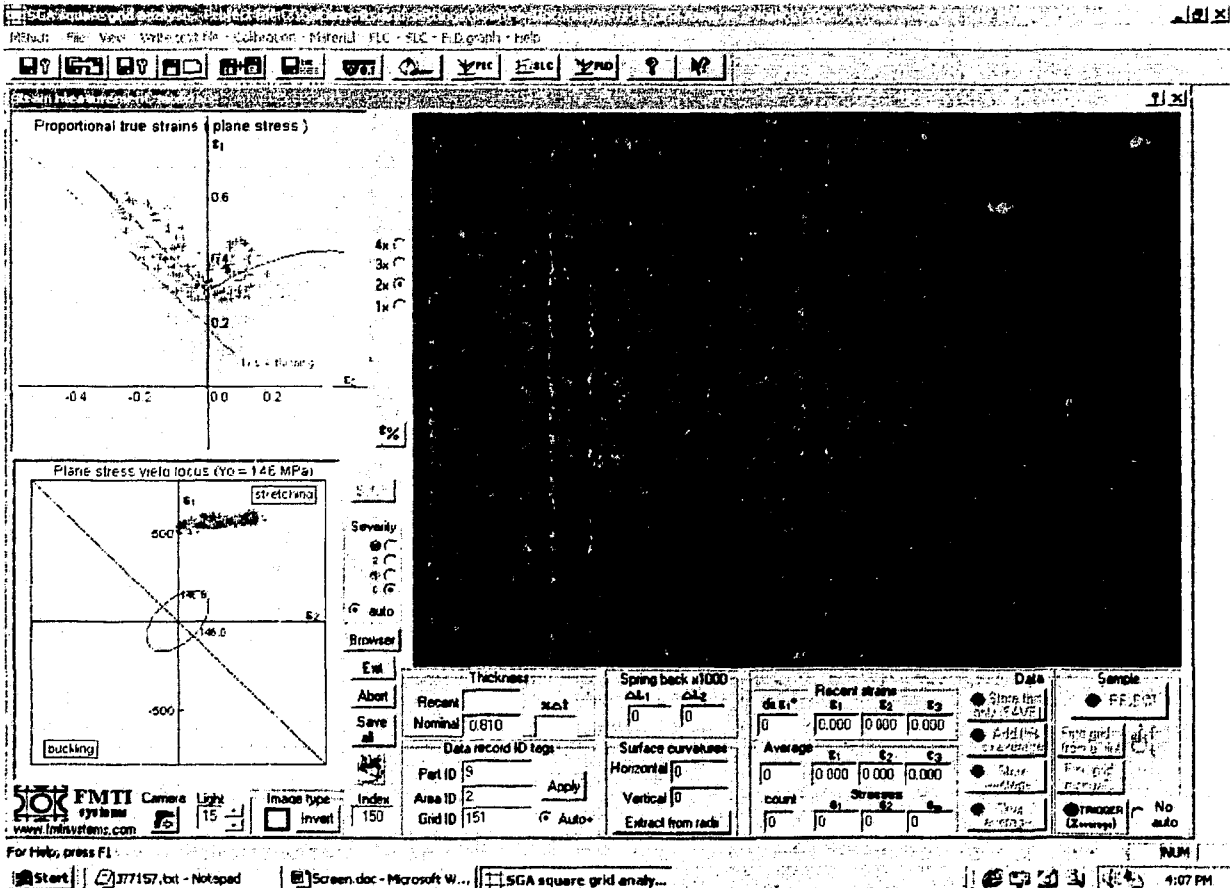


Figure 3.6. SGA software screen for locating the deformed squares.

The system calculates the strains from the deformation gradient tensor, F . The algorithm used for strain calculations has been reported by Sklad [29]. The use of 1 mm square grids as compared to circular grids gave a better understanding of the directionality and the different strain paths developed during the forming process.

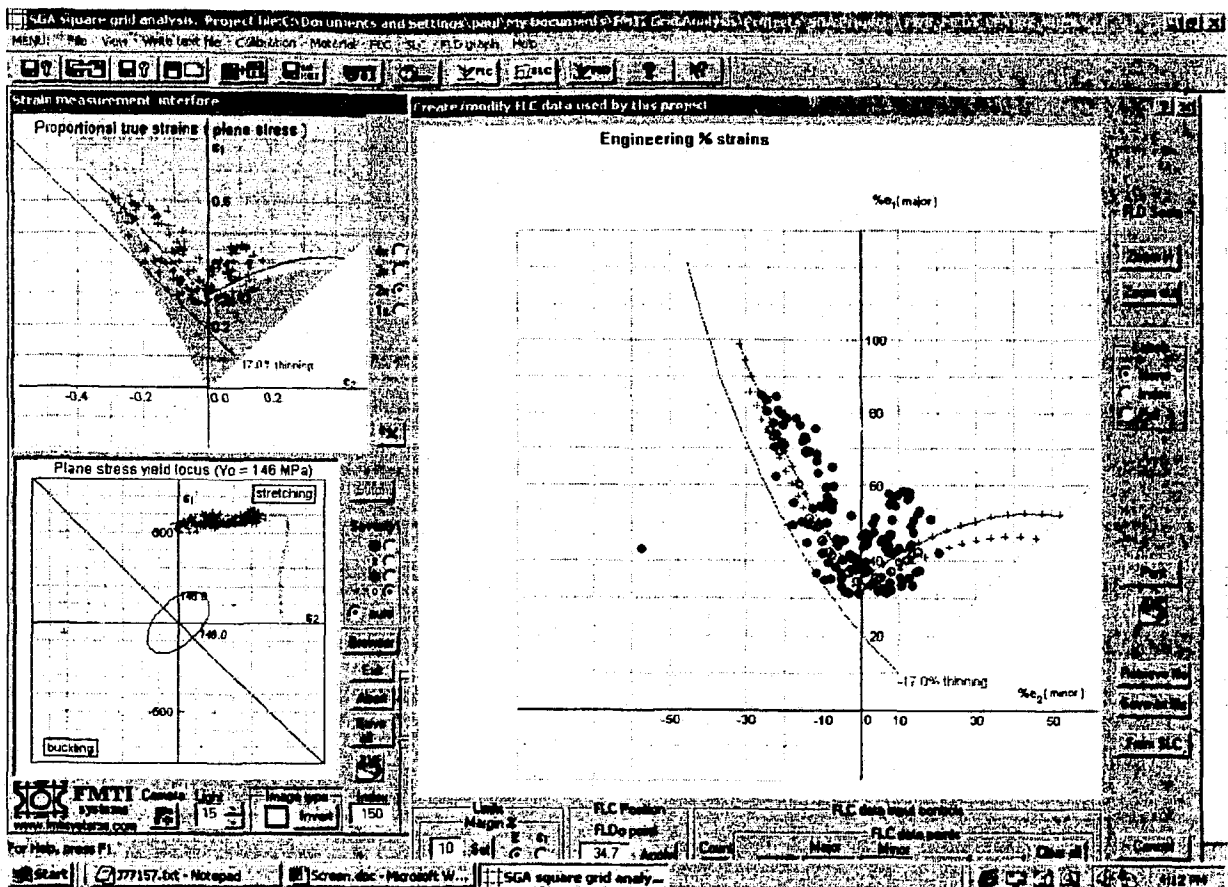


Figure 3.7. SGA software screen showing the major and minor strains.

3.2.3 Tensile Tests

The tensile properties, i.e., the yield strength, ultimate tensile strength and elongation, for all the base metals of the TWBs, without the weld bead, were determined according to ASTM E8M standards [30] using a Schenck-Treble tensile testing system at Dofasco. The specimen dimensions are shown in Figure 3.8. The tests were carried out in a velocity controlled mode. From the data generated from these tensile tests, the strain-hardening exponent (n -value) was calculated as specified in ASTM E646 [31], using the power curve representing the true-stress

versus true-strain curves within the strain range of 10–20%. The power curve is given by,

$$\sigma = K \epsilon^n \quad (3.1)$$

where, σ = True stress,

K = Strength coefficient,

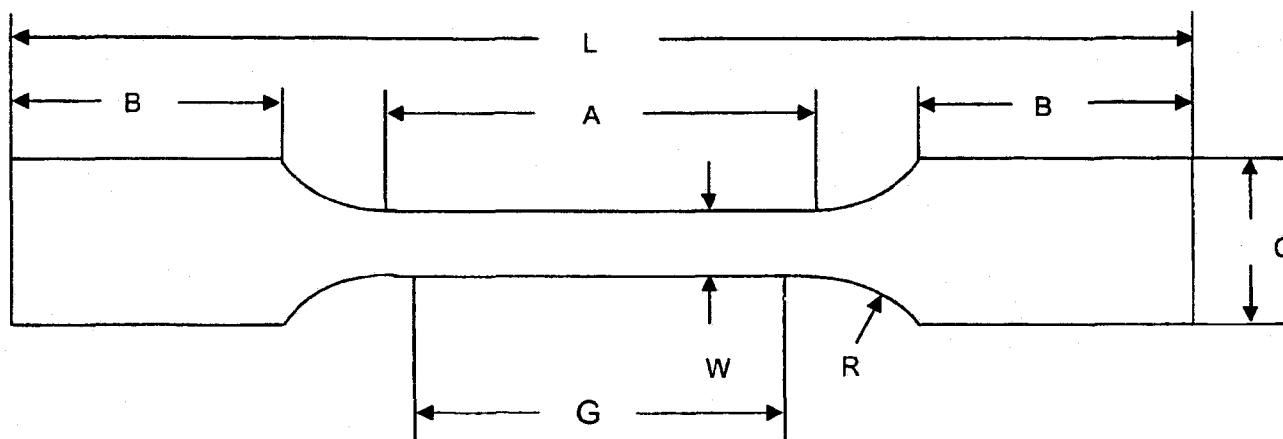
n = Strain-hardening exponent,

ϵ = True strain.

Taking natural logarithm for Eq. 3.1 gives:

$$\log \sigma = \log K + n \log \epsilon, \quad (3.2)$$

Linear regression analysis of $\log \sigma$ versus $\log \epsilon$ gives the slope, i.e., the n -value of true-stress versus true strain plot. Sample calculations with a log-log curve for one of the base metals, i.e., 1.5 mm thick (BM), are shown in Appendix A.

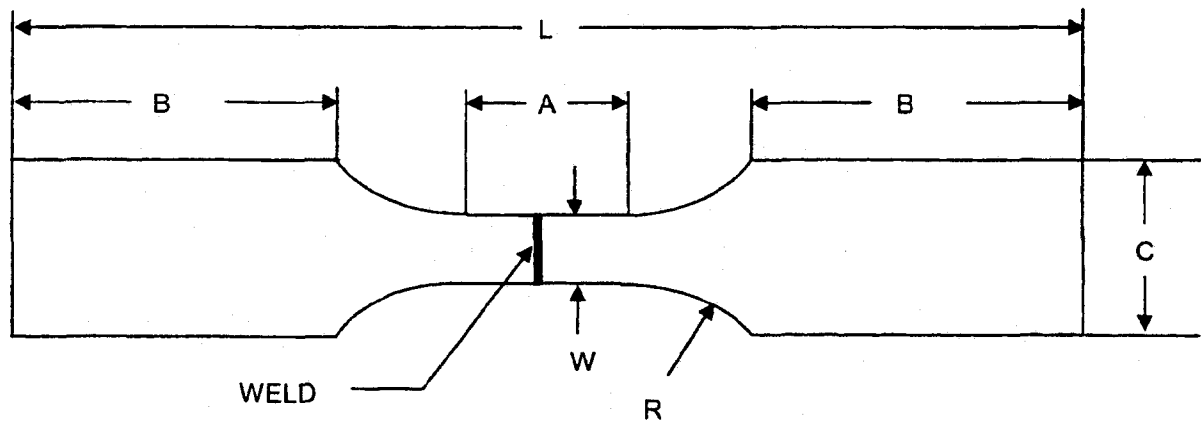


Dimensions in mm	
G – Gauge length	50
W – Width	12.5
R – Radius of fillet	12.5
L – Overall length	200
A – Length of reduced section	57
B – Length of grip section	50
C – Width of grip section	20

Figure 3.8. Geometry and dimensions of standard tensile test specimens.

3.2.4 Fatigue Tests

The geometry of the laser butt-welded fatigue test specimen is shown in Figure 3.9. The weld bead was located at the centre, oriented in a direction perpendicular to the loading direction. For the base metal (BM) being tested, the dimensions were exactly the same as those for the specimen with the laser weld at the centre. The rolling direction of the material was in the loading direction. Similar geometry has also been used in other published work [23-26]. To avoid the effect of sharp edges on the fatigue properties, the gauge area of all the specimens was slightly smoothed out by hand polishing using a 084 fine (# 400) emery paper.



Dimensions in mm	
W - Width	6.5
R - Radius of fillet	25.4
L - Overall length	145
A - Length of gauge section	15
B - Length of grip section	50
C - Width of grip section	25

Figure 3.9. Geometry and dimensions of fatigue test specimens with a laser-welded butt joint.

The fatigue tests were carried out at Ryerson University on a fully computerized servo-hydraulic fatigue testing system (INSTRON: 8801). The tests were carried out in a load control mode as per ASTM E466 [32] specifications. Samples were subjected to tensile stress fatigue cycles [23, 26-28], in a direction perpendicular to the weld line, using a stress ratio R ($\sigma_{\min}/\sigma_{\max}$) = 0.1. A sinusoidal loading shape with a frequency of 50 Hz was used in all the tests. The test was stopped at 10^7 cycles and the sample was considered as a run out. At the beginning of the test, the value of the maximum applied load, P_{\max} , was selected to be about half the tensile strength. The S-N curve for each TWB and the base metal was determined with 8-12 different specimens. The mean load, P_{mean} , which was one of the input parameters, can be calculated as follows,

$$R = \frac{\sigma_{\min}}{\sigma_{\max}} = 0.1, \quad (3.3)$$

$$\sigma_m = \frac{\sigma_{\max} + \sigma_{\min}}{2} = \left(\frac{1+R}{2} \right) \sigma_{\max}, \quad (3.4)$$

$$\sigma_a = \frac{\sigma_{\max} - \sigma_{\min}}{2} = \left(\frac{1-R}{2} \right) \sigma_{\max}, \quad (3.5)$$

$$\frac{\sigma_m}{\sigma_a} = \frac{1+R}{1-R}, \quad (3.6)$$

$$\sigma_m = 1.22 \times \sigma_a, \quad (3.7)$$

$$P_{\text{mean}} = A_c \times \sigma_m, \quad (3.8)$$

where, σ_{\min} = Minimum stress,

σ_{\max} = Maximum stress,

σ_m = Mean stress,

σ_a = Stress amplitude,

P_{mean} = Applied mean load,

A_c = Cross-sectional area of the specimen.

3.2.5 Microstructure and Microhardness Tests

Prior to the forming and fatigue tests, the microstructure of the weld cross-section was examined under an optical microscope to evaluate the quality of the laser welds. Cross-sections of the TWB with weld bead and base metals were mounted using a hot mounting press. The mounts were then ground and polished using different grits of sand papers on an automated grinding wheel manufactured by Struers Inc. The grinding of the material was carried out on MD-Piano diamond disc. The use of diamond paste as an abrasive leads to a higher material removal rate and short grinding times. The fine grinding was carried out on MD-Allergo (SiC based cloth) with diamond suspension as abrasive. The diamond size was in the range of 3-15 microns. Fine polishing of the material was carried out on MD-Dac and MD-Nap discs (SiC based cloth). The abrasive used was diamond suspension with particle range of 1–3 μm along with an alcohol based lubricant (DP-Blue). The lubricant provided a high cooling and low smearing effect [33]. The welds were initially observed in the unetched condition to check for inclusions. Further, 4% Nital was used as an etchant to develop the microstructure. The etched samples were then observed under an optical microscope.

Vickers microhardness tests were carried out on a fully computerized and automated microhardness tester, Clemex MT-2001. The specimens used were similar to those used for the microstructural analysis. The load applied was 300 grams with a dwell time of 15 seconds. The indents were spaced at a distance of 100 μm (Figure 3.10) from one another. The recorded Vickers hardness (HV) values are listed in Appendix B. The microstructure and microhardness tests were carried out at Dofasco.

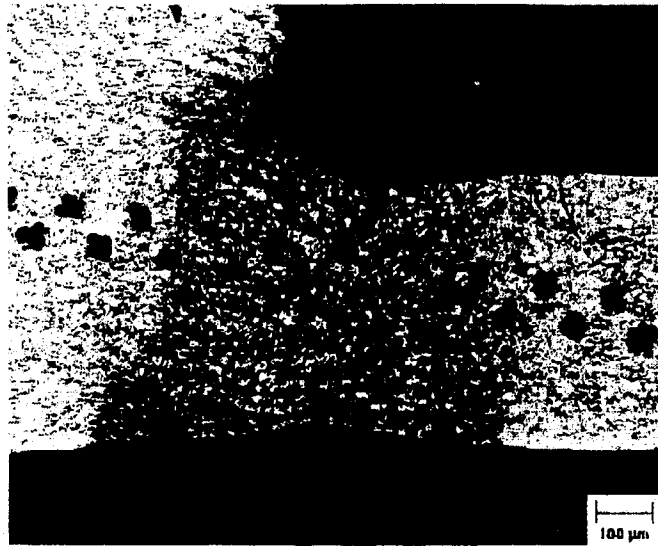


Figure 3.10. Light micrograph showing the indent pattern, size and spacing across the weld.

3.2.6 Scanning Electron Microscopy

After the fatigue tests, to identify the fatigue crack initiation sites and crack propagation mechanisms, fracture surfaces were examined using a fully automated (JEOL: JSM – 6460 LV) conventional low vacuum microscope operating in back scattered electrons (BSE) mode. EDS analysis was used to identify if zinc is present on the fracture surfaces. These tests were done at Dofasco's research and development facility.

Chapter 4

Experimental Results

4.1 Microstructural Observations

The microstructure of the weld cross-section revealed that the welds were free of any welding defects such as porosity, concavity, cracks, voids, inclusions and misalignments, as shown in Figure 4.1. This indicated that the welding parameters used for the TWBs (Table 3.3) are appropriate to obtain sound welds. The average width of the fusion zone was about 0.8 – 1 mm and that of the total heat-affected zone on either sides of the base metal was approximately 0.7 – 1 mm. The microstructure in the base metals shows equiaxed grains of ferrite. The weld zone shows fine pearlite and/or low carbon bainite. Details will be discussed in section 5.2.

4.2 Tensile Properties

The tensile properties of the base metals consisting of the TWBs were determined as described in section 3.2.3 and are given in Table 4.1. Figures 4.2 and 4.3 show the engineering stress–strain curves for the thin and thick sheets of the TWBs, respectively. It is seen that the respective yield strengths of the thinner and thicker sheets of the TWBs are 185 and 156 MPa (GMX), 160 and 159 MPa (W-Car) and 155 and 146 MPa (MC-DI). Similarly, the n -values are 0.225 and 0.227 (GMX), 0.238 and 0.244 (W-Car) and 0.237 and 0.246 (MC-DI). While strengths of GMX (very low carbon steel) and W-Car and MC-DI (IF steels) are similar, the IF steels have a better elongation.

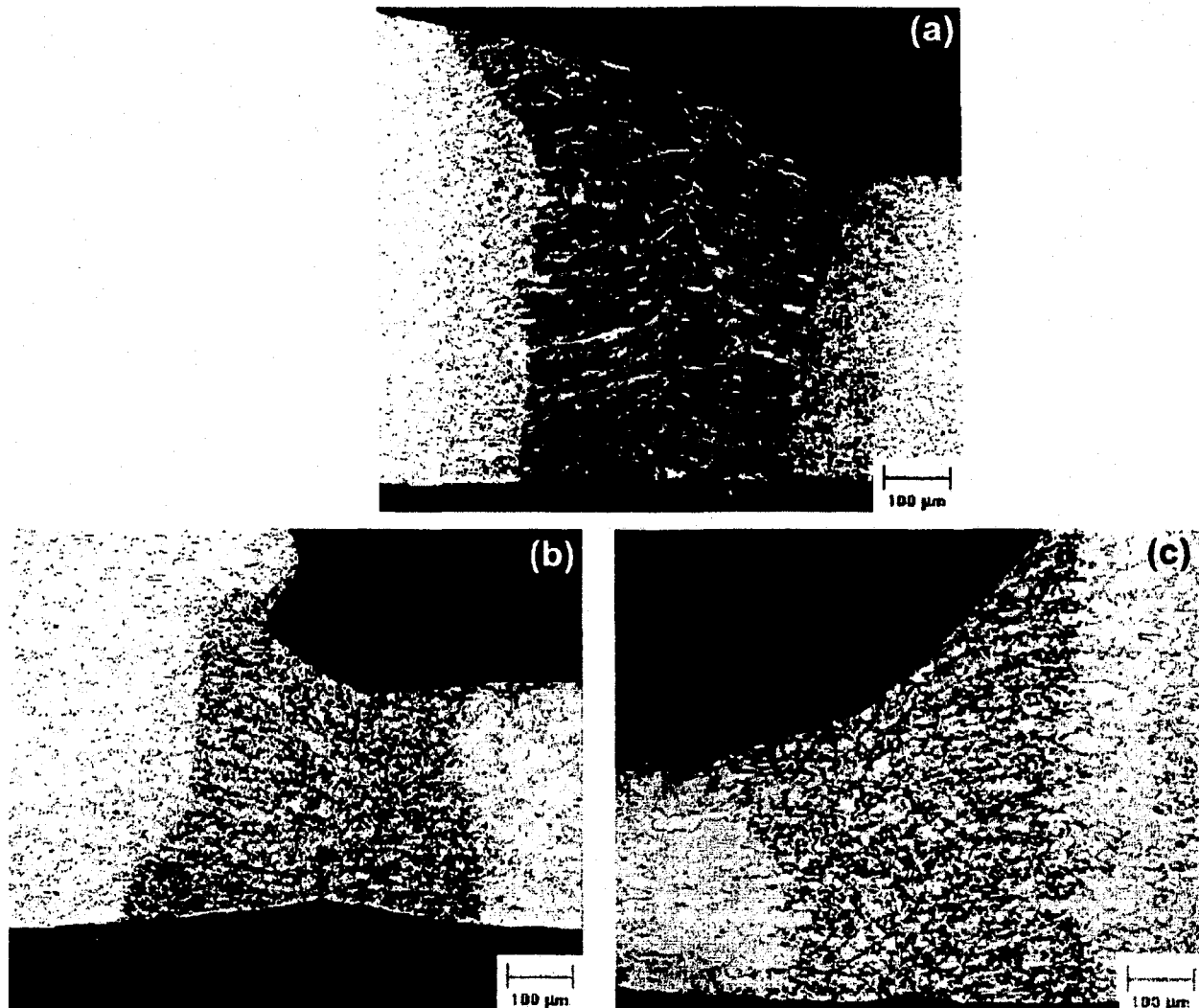


Figure 4.1. Microstructures of the laser welded blanks. (a) GMX (b) W-Car (c) MC-DI.

Chan *et al.* [19] carried out the tensile tests of the TWBs with the weld being at the centre and oriented perpendicular to the loading axis. They found no significant difference in the tensile strengths of the TWBs and their relative thinner base metals. Therefore in this study, the tensile properties of both, the thinner and the thicker base metals were determined, as opposed to the TWB combinations. The ultimate

tensile strength (UTS) of the thinner sheet of the three TWBs, i.e., GMX, W-Car and MC-DI were 301 MPa, 305 MPa and 297 MPa, respectively.

Table 4.1. Tensile properties of the base metals.

I. D.	Material grade	Sheet thickness (mm)	Yield strength (MPa)	Tensile strength (MPa)	Elongation (%)	Mean n-value*
GMX	Very low	1.50	185	324	44.9	0.225
	carbon steels	0.90	156	301	48.1	0.227
W-Car	Interstitial	1.67	160	301	50.9	0.238
	free steels	0.75	159	305	49.3	0.244
MC-DI	Interstitial	2.00	155	284	51.8	0.237
	free steels	0.80	146	297	49.3	0.246

* n-values were determined from the data in the strain range of 10–20%.

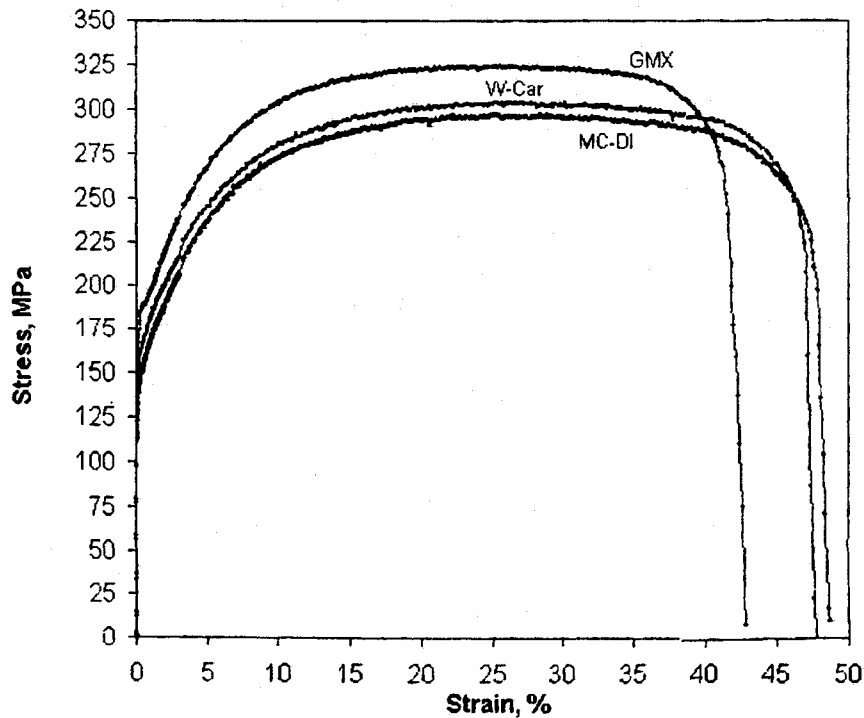


Figure 4.2. Stress-strain curves of the thinner base metals of the TWBs.

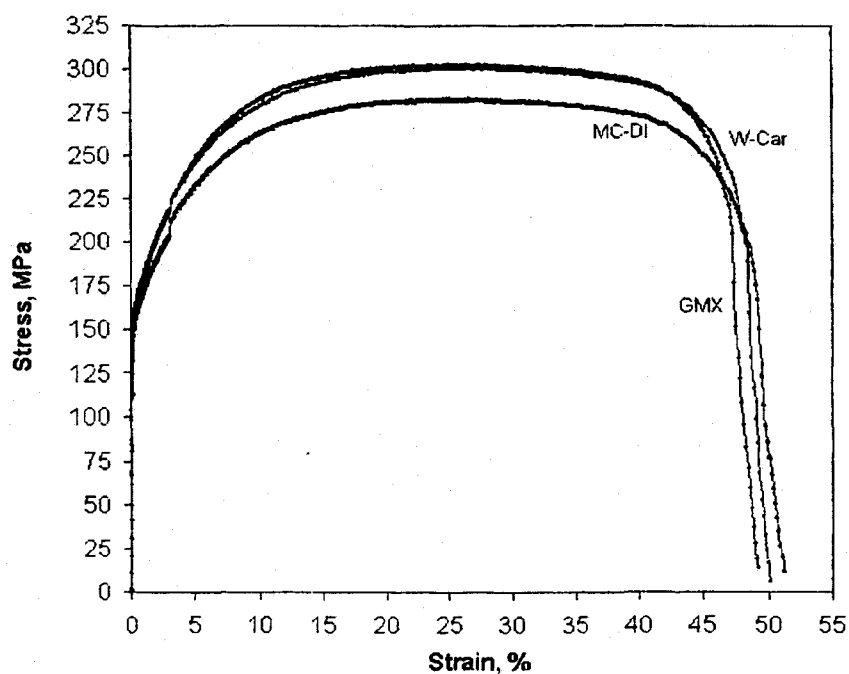


Figure 4.3. Stress-strain curves of the thicker base metals of the TWBs.

4.3 Formability Results

4.3.1 Forming Limit Diagrams

The forming tests and strain measurements were carried out according to the procedure described in section 3.2.2. The comprehensive FLDs for GMX, W-Car and MC-DI TWBs are plotted in Figures 4.4, 4.5 and 4.6, respectively. The circular points in these figures represent the strains in the fracture/necked region and the diamond shaped points are the strains from the safe region. For the ease of comparing the data, theoretical FLDs of the base metals are superimposed on the measured FLDs. The upper curve represents the theoretical FLD of the thicker sheet and the lower curve represents the thinner sheet. The theoretical FLD of the individual base metals were developed using the NADDRG equation (Eq. 2.5) and

linear regression analysis by Andreychuk [34]. The data used in plotting the comprehensive FLD are included in Appendix C.

However, for analyzing the results, only strains that clearly separated the safe and necked region were used to plot the FLD for the TWB combinations. The experimental fail-safe boundary lies between the lines representing the theoretical FLDs of thin and thick sheets of each TWB.

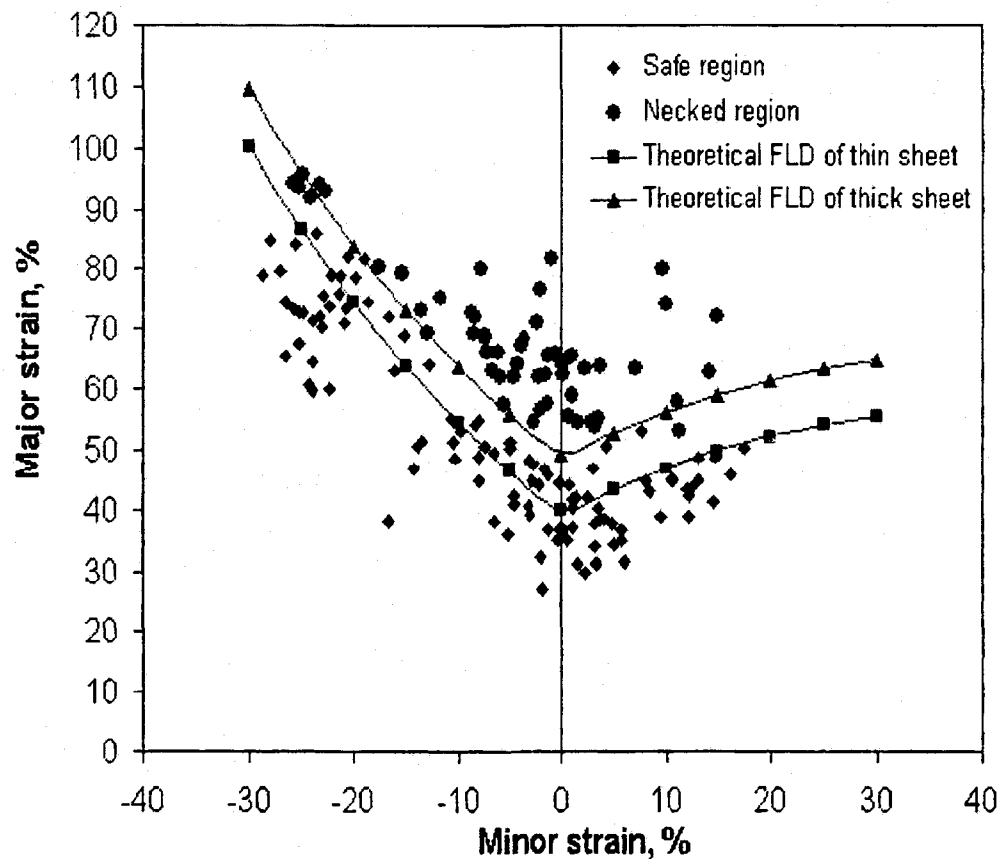


Figure 4.4. Comprehensive FLD for GMX TWB.

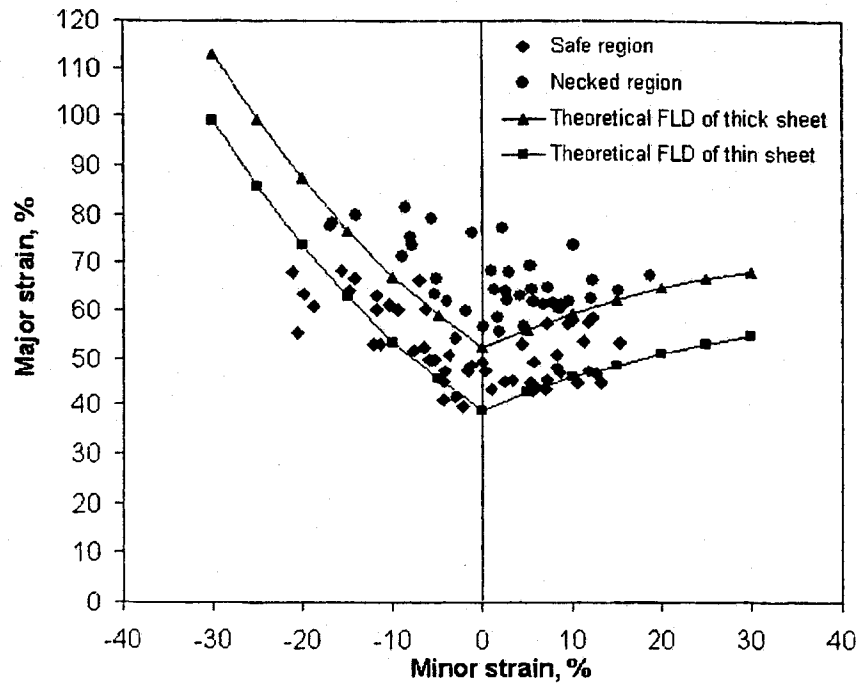


Figure 4.5. Comprehensive FLD for W-Car TWB.

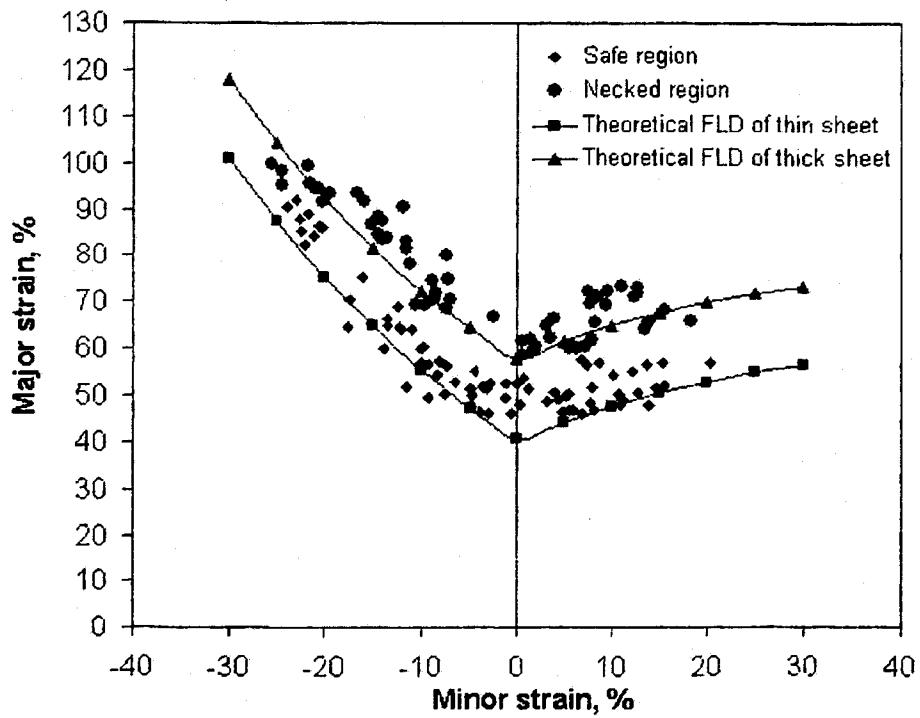


Figure 4.6. Comprehensive FLD for MC-DI TWB.

4.3.2 Major and Minor Strains

As seen from Figures 4.4, 4.5 and 4.6, a number of square grids in both the safe and fracture/necked region were measured on all the different width specimens to determine the minor and major strains. Of these, a limited but sufficient number of strain values from the safe region were used to plot the final FLD diagrams representing the experimental fail-safe boundary. These data points are given in Table 4.2.

Table 4.2. Minor and major strain values for the TWBs.

I. D.	Minor strain, %	Major strain, %
GMX	-23.6	86.1
	-20.6	82.1
	-19.8	78.7
	-18.5	74.6
	-16.5	72.3
	-15.2	68.9
	-12.8	64.3
	-7.9	54.7
	-5	50.2
	-2.7	47.4
	-1.2	45.9
	-0.2*	44.4*
	0.8*	44.2*
	3	46.8
	4.4	50.5
	7.7	53.2
I. D.	Minor strain, %	Major strain, %
W-Car	-15.7	68.6
	-14.3	66.7
	-11.8	63.4
	-10.4	61.2
	-9.4	60.3
	-3.8	51
	-1.3*	48.6*
	0.4*	47.2*
	5.7	49.2

	8.2	50.8
	11.3	53.7
	15.3	53.6
I. D.	Minor strain, %	Major strain, %
MC-DI	-23.8	90.5
	-22.6	88.2
	-21.1	84.2
	-16.1	75.3
	-13.4	66.3
	-12.2	64.5
	-12	64.1
	-10.8	63.9
	-10	59.9
	-9.7	60.4
	-8.1	57.2
	-7.3	56.1
	-6.4	52.9
	-5	51.5
	-3.5	51.6
	-3	51.4
	-2.7	52.3
	-1*	49.4*
	0.5*	47.9*
	3.3	48.6
	3.9	50.4
	4.4	49.2
	5.1	49.9
	5.5	50.1
	7.9	51.8
	10.1	54.4
	12.2	55
	13.7	56.4
	15.3	57

* Bold values indicate (near) FLD₀ strains.

4.4 Fatigue Results

Fatigue tests were carried out according to the procedure described in section 3.2.4. The recorded data for the stress amplitude and number of cycles is shown in Appendix D. The obtained S-N curves for the selected three TWB combinations and BM are shown in Figure 4.7.

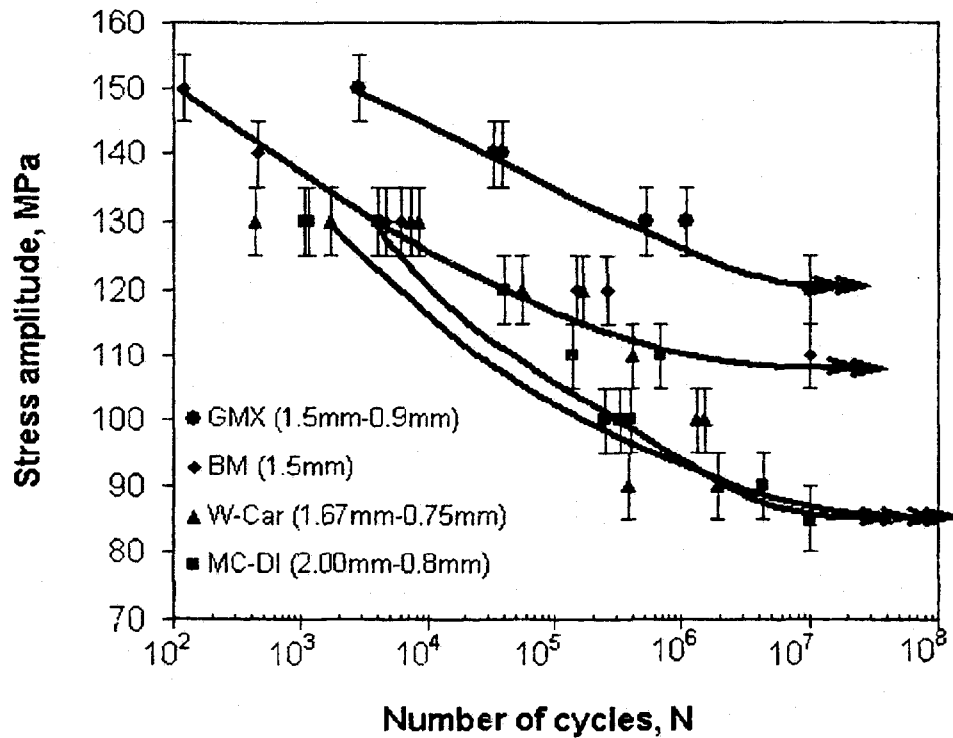


Figure 4.7. S-N curves for the base metal and different TWB combinations, tested at 50 Hz, R = 0.1 and room temperature.

It is seen from Figure 4.7 that the fatigue limit for W-Car and MC-DI TWB combinations, which were zinc-coated (galvanized), is much lower (85 MPa) than that for the non-galvanized or bare GMX TWB (120 MPa), and the base metal (110 MPa). The reason will be discussed in section 5.4.

Chapter 5

Discussion

5.1 On Weld Quality and Failure Location

The microstructural observations (Figure 4.3) show that the laser welds were free of any defects. While carrying out the forming tests on the TWBs, the forming failure for all the three combinations was observed to occur in the thinner section. These findings are summarized in Table 5.1. However, the location of the fracture/neck on the thinner section showed some variation with the difference in the widths of the specimens. The width of the specimens varied from a minimum of 25.4 mm (1.0 in) to a maximum of 203.2 mm (8 in).

It was observed that for the smaller width specimens (25.4 – 76.2 mm), the fracture/necking occurred at an angle of 30-40° to the weld bead (Figure 5.1). Also, the location of the failure was at a distance of about 40 mm from the weld bead. Narrower specimens usually generate a deep drawing effect on the materials being formed [2, 4, 5, 7]. The material flow occurs along the side of the punch face as against the top of the punch which causes the material to fail at a distance from the weld bead.

With the larger widths (88.9 – 203.2 mm) representing the plane strain and balanced bi-axial stretch modes, the failure occurred in a direction parallel to the weld bead at a distance of 7–11 mm (Figure 5.2). In this case, the punch surface has a maximum contact area with the specimen which results in the material being stretched in all directions which leads to the necking at the top of the punch face.

Irrespective of the failure mode, all the failures occurred in the thinner base metal indicating that the welding parameters given in Table 3.3 produced defect-free welds with no forming failures in the weld zone (fusion and heat affected zones). In a TWB

consisting of materials having different thicknesses with similar strength, most of the plastic strain is distributed in the thinner material as it has a lower resistance to the applied force than the thicker material, and hence the forming failure is always associated with the thinner material [19, 20].

The guideline for the acceptance of a TWB laser weld is based on the weld failure mode. A/SP [1] has specified that, if a weld failure occurs either in the weld or the heat-affected zone (HAZ) in a direction parallel to the weld seam, the weld is considered unacceptable. However, if the failure occurs in the weld in a direction perpendicular to the weld seam or in the base metal, it is acceptable. On the basis of these guidelines, the TWBs in the present work are all acceptable.

Similar observations have been reported by other researchers. Ghoo *et al.* [21] have reported failures perpendicular to the weld bead in the case of similar thickness TWBs. However, they have not confirmed the reason for such a failure mode. Chan *et al.* [19, 20] observed the forming failure in the thinner part of the TWBs in a direction that was parallel to the weld line and perpendicular to the principal strain. This was attributed to the non-uniform strain distribution in the thinner material as it resists a much smaller force than the thicker material. Shi *et al.* [18] carried out experiments on similar and dissimilar thickness TWBs. In the case of similar thickness TWBs, they observed the failure in a direction perpendicular to the weld bead and on the other hand, for dissimilar thickness TWBs, the forming failure was observed in the thinner section and was parallel to the weld bead. Failure across the weld is caused by the low forming limit in the weld. The failure parallel to the weld was because of too large of a thickness difference.

Table 5.1. Failure location and orientation in different width specimens.

Specimen width (mm)	Location of the fracture/neck from the weld bead	Orientation of the fracture/neck with respect to the weld bead
25.4-76.2	40 mm from the weld	Inclined at 30-40°
88.9-139.7	7-9 mm from the weld	Parallel
152.4-203.2	9-11 mm from the weld	Parallel

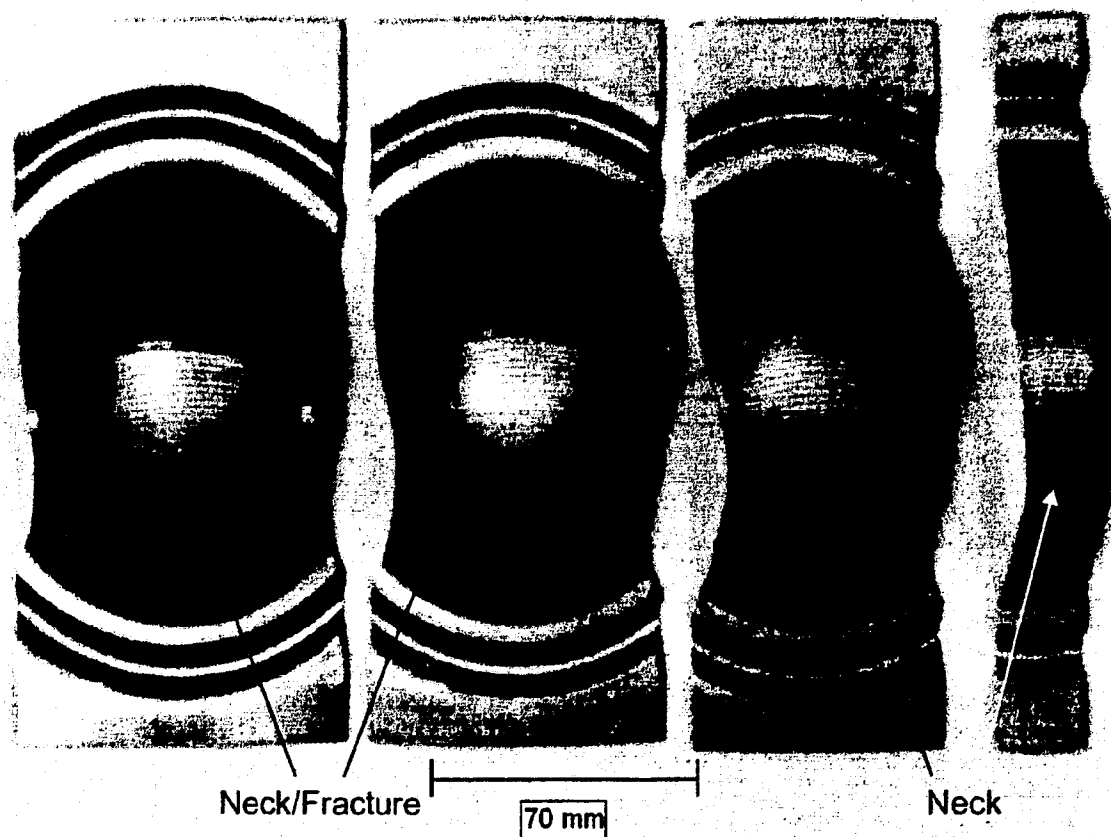


Figure 5.1. Failure location in narrow width specimens.

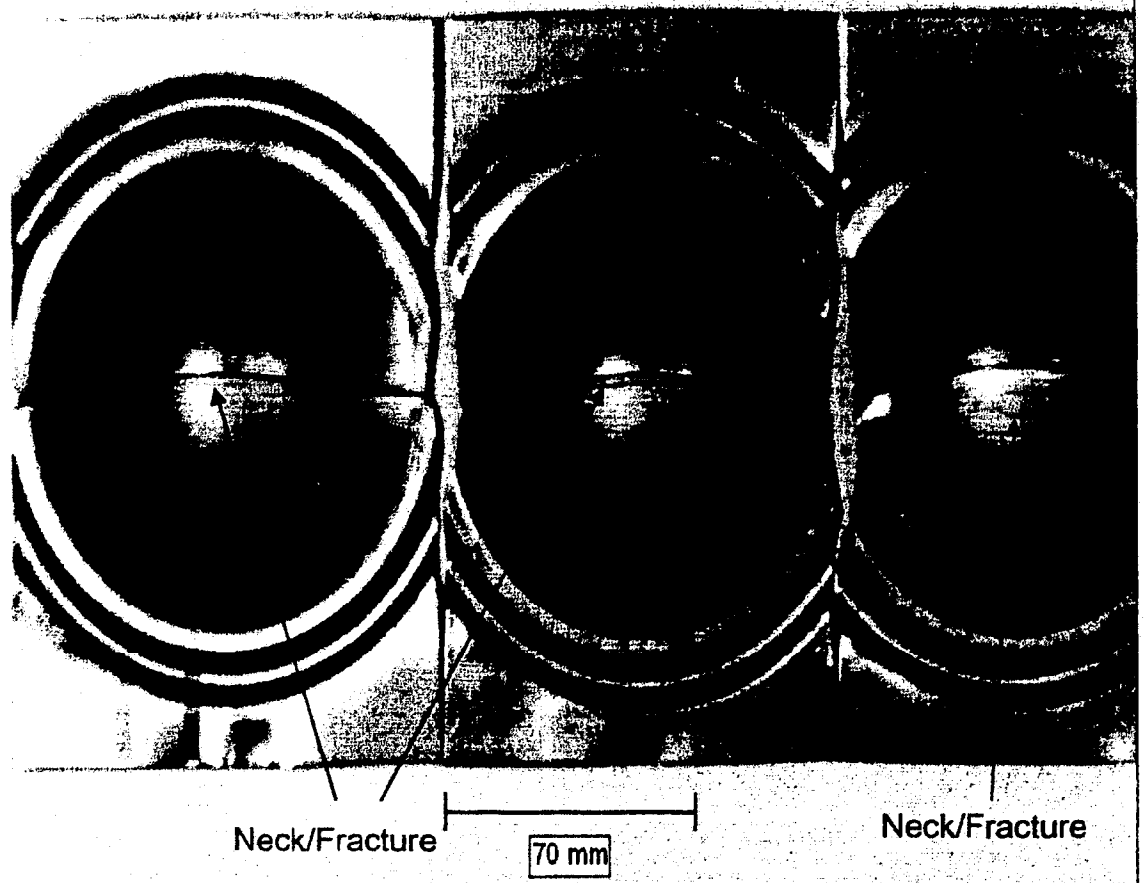


Figure 5.2. Failure location in broad width specimens.

5.2 On Microhardness

The microhardness traverses of the TWB cross-section show a higher hardness in the weld (Figure 5.3), as compared to the individual base metals. In all the three combinations of TWBs, it was found that the hardness of the weld bead was about 2.5 times higher than that of the respective base metal. This is attributed to the localized thermal energy input and sudden cooling, which is typical of the laser welding process and is reported by other researchers [20, 24, 25].

Shi *et al.* [18] and Lazzarin *et al.* [23], while comparing the different welding techniques on hot dip galvanized-low carbon steels, reported a higher hardness in the weld that was made by the laser welding process as compared with the mash seam welding process. Rhee *et al.* [24], for similar and dissimilar thickness sheet metals, reported the hardness in the weld bead to be 2.3 times than that of the respective base metals. Lee *et al.* [26] have reported that laser welding generates the narrowest weld zone as compared with the electron beam (1.5 times) and mash seam welding (4 times) processes. They also found the microhardness peaks for the laser welding process to be higher than the electron beam and mash seam welding processes. However, they did not explain the appropriate reason for the higher hardness in the weld.

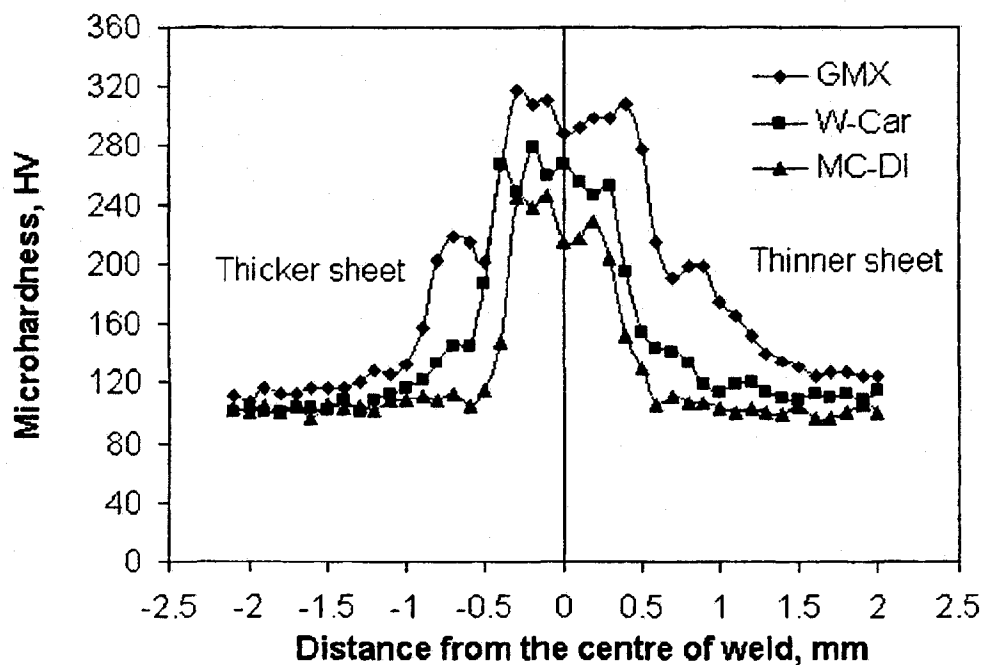


Figure 5.3. Microhardness profile of the three TWBs.

Interstitial free and very low carbon steels contain micro-alloying elements like titanium (Ti ~0.01%) and niobium (Nb ~0.02%) [35]. The addition of these micro-alloying elements contributes to an increase in strength and hardenability through

microstructural refinement, solid-solution strengthening and precipitation hardening [36]. A typical microstructure (Figure 5.4(a)) of such steels consists of a ferrite matrix with imbedded precipitates of titanium and niobium carbides. The ferrite has different morphologies based on the decomposition of austenite and are identified as: polygonal ferrite having equiaxed grains and low dislocation density, widmanstatten ferrite, defined by elongated grains with a dislocation substructure, granular ferrite containing islands of micro-constituents and a high dislocation density and bainitic ferrite, which consists of parallel ferrite laths and high dislocation densities [36]. Due to the accelerated and nonequilibrium cooling rate of the laser welding process, the formation of polygonal ferrite is suppressed and instead leads to the formation of nonequilibrium, nonequiaxed granular ferrite and/or bainitic ferrite. Due to these nonequilibrium conditions of cooling, the ferrite microstructures possess some unique morphological features [36]. With an increase in the cooling rate, the volume fraction of granular ferrite and bainitic ferrite is observed to grow at the expense of polygonal ferrite. At a point where the microstructure reveals mostly granular ferrite, the locations of prior-austenite grain boundaries get preserved. Further, as the temperature falls below the critical temperature of 727°C , this preserved austenite transforms to a finer pearlite and/or low carbon bainite structure [36], as shown in Figure 5.4(b). This phenomenon explains the increase in hardness of the weld metal.

Similar observations were reported by Biro [37]. He found that due to the high and rapid heat input by the laser welding technique, the austenite was stabilized in the carbon rich zone. The rapid heat dissipation in the fusion zone leads to the formation of finer pearlite and bainite. However, the amount of bainite formed was relatively small as compared to pearlite because of the lower carbon content in the base metals being welded.

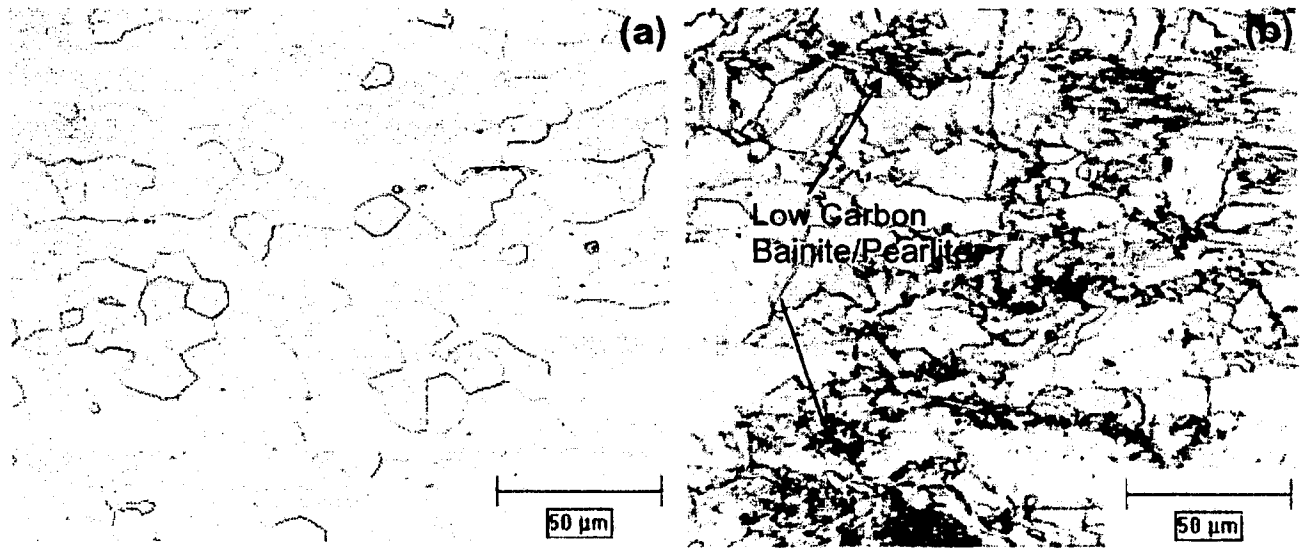


Figure 5.4. Typical microstructures in the laser welded blanks. (a) Base metal (b) Weld metal.

5.3 On Formability

5.3.1 Effect of Strain-hardening Exponent and Sheet Thickness on the FLD_0 of Tailor Welded Blanks

As can be seen from the NADDRG equation (Eq. 2.5), the FLD_0 of a sheet metal is a function of its n -value and the thickness. Since the TWBs in this study are composed of two materials with different thicknesses, a novel approach has been considered for calculating the FLD_0 values for the TWBs. It was assumed that, for the TWB combination under consideration, the n -value of the TWB is the mean of the n -values of the base metals, and similarly the thickness of the TWB is the mean of the individual base metal thicknesses. This can be represented as,

$$n_{TWB} = \frac{n_{Thick} + n_{Thin}}{2}, \quad (5.1)$$

and

$$t_{TWB} = \frac{t_{Thick} + t_{Thin}}{2} \quad (5.2)$$

where n_{TWB} = Mean n-value of thick and thin sheets of the TWB,
 t_{TWB} = Mean thickness of thick and thin sheets of the TWB,
 n_{Thick} = Strain-hardening exponent of thicker sheet,
 n_{Thin} = Strain-hardening exponent of thinner sheet,
 t_{Thick} = Thickness of the thicker sheet,
 t_{Thin} = Thickness of the thinner sheet.

These values were then used to substitute n and t in Eq. 2.5, and the FLD_0 for the TWB was calculated. For example, considering the GMX TWB combination having a thickness combination of 1.5 mm and 0.9 mm and respective n-values of 0.225 and 0.227 (Table 4.1), the n-value and the thickness of the TWB are,

$$n_{TWB} = \frac{0.225 + 0.227}{2} = 0.226, \quad (5.3)$$

and

$$t_{TWB} = \frac{1.5 + 0.9}{2} = 1.2 \text{ mm}. \quad (5.4)$$

Substituting the above values into Eq. 2.5, the FLD_0 value for the GMX TWB becomes,

$$\begin{aligned} FLD_{0(TWB)} &= \frac{0.226}{0.21} (14.1 \times 1.2 + 23.3) \\ &= 43.2\%. \end{aligned} \quad (5.5)$$

Similar calculations can be done for other TWB combinations, and the obtained results are given in Table 5.2. These calculated values were then compared with the measured FLD_0 values.

The forming failure for all the three TWB combinations was observed to occur in the thinner section. Thus, the calculated FLD_0 values (major strain values under plane strain condition) of the thinner sections were compared with the measured FLD_0 values for the TWBs. The measured FLD_0 values were not located at the exact uniaxial strain coordinate of (0, y) (Table 4.2) and hence had to be interpolated to obtain the major strain at 0% minor strain.

For the GMX TWB, the two sets of values closest to and on either side of 0% minor strain are (-0.2%, 44.4%) and (0.8%, 44.2%). The initial difference d_i between -0.2% and 0.8% is 1% and the final difference d_f between 44.2% and 44.4% is 0.2%. Using the principle of similar triangles and values of d_i and d_f (Figure 5.5) gives,

$$0.8\% : 1\% = (X - 44.2\%) : 0.2\% \quad (5.6)$$

$$\therefore X = FLD_0 \text{ (interpolated)} = 44.3\%.$$

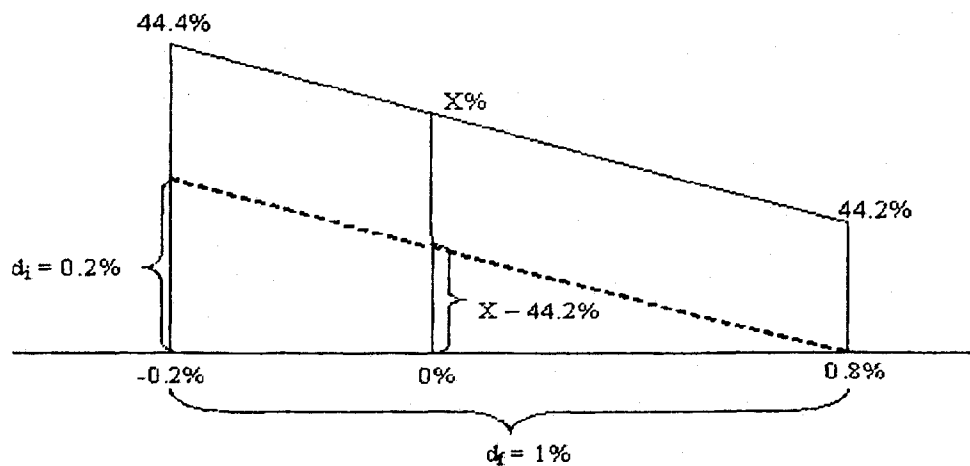


Figure 5.5. Principle of similar triangles for interpolation.

The above adjusted measured FLD_0 (i.e., interpolated) value (Eq. 5.6) gives the major strain at 0% minor strain and was compared with the calculated FLD_0 value of 43.2% obtained from Eq. 5.5. Similar results were calculated for the W-Car and MC-DI TWBs, and are shown in Table 5.2.

Table 5.2. Comparison of the calculated and adjusted measured FLD_0 value for the TWBs.

I.D.	Thickness of TWB, t_{TWB} (mm)	n-value of TWB, n_{TWB}	Calculated FLD_0 of TWB (%)	Adjusted measured FLD_0 of TWB (%)	Difference between calculated and adjusted measured FLD_0 (%)
GMX	1.2	0.226	43.2	44.3	-2.5
W-Car	1.21	0.241	46.3	47.5	-2.5
MC-DI	1.4	0.241	49.4	48.4	2.0

It can be seen from Table 5.2 that the adjusted measured (interpolated) and calculated FLD_0 values are in good agreement with small differences of less than $\pm 2.5\%$. Thus, the above method using the mean n-value and thickness values of the TWB in the NADDRG equation (Eq. 2.5) provides a reasonably accurate prediction of the FLD_0 of a TWB. Further, the above finding indicates that the two important parameters to be considered while determining the FLD_0 value of TWBs are the strain-hardening coefficients of the base metals and their respective thicknesses.

In the reported literature [18, 20, 21], researchers have evaluated the formability of TWBs by measuring the dome heights to failure (Figure 2.21). The effect of the material thickness and properties (n-value) on the FLD_0 of TWBs has not been explored in detail. The semi-empirical relation in this work, though relatively simple,

can be used as a guideline in the press shop to effectively utilize the material properties for a successful stamping operation.

5.3.2 Comparison of the Forming Limit Diagram of Tailor Welded Blanks with the Base Metals

Most of the forming failures generally occur in the plane strain condition close to the FLD_0 position. In this region, the material is stretched over the punch face leading to severe deformation. Therefore, the position of the FLD_0 on the major strain axis (y-axis) of a forming limit diagram becomes an important indicator of the failure tolerance of a TWB. For any material, the higher the FLD_0 value, the higher the forming limit. For the TWBs studied in this work, the forming failure was observed to occur in the thinner sheet. Hence the FLD_0 of the thinner sheet was calculated using Eq. 2.5 and compared with the measured FLD_0 of the TWBs.

For GMX TWB, the adjusted measured FLD_0 (section 5.3.1) was at 44.3% major strain. The calculated FLD_0 (based on Eq. 2.5) of the thinner section (0.9 mm) was 39.7% major strain. As seen from Figure 5.6, the FLD_0 of the TWB is about 4.7% higher than the FLD_0 of the thinner sheet. Also, the FLD_0 of the TWB lies in-between those of the thin and thick sheets.

Chan *et al.* [19], while comparing the FLD of a TWB with the base metal, reported lower FLD_0 values for the TWBs with respect to the thicker section alone. However, they did not report the relative FLD_0 level of the thinner sheet. It may be intuitively surmised that, because of the presence of the weld bead, the FLD_0 of the TWB would be inferior to that of the individual base metals (and hence the thicker sheet as illustrated by Chan *et al.* [19]). The findings of the present work show that the FLD_0 of the TWB is lower than that of the thicker sheet (similar to Chan *et al.* [19]); it is also greater than that of the thinner sheet. While designing a panel, the

automotive stamping industry, based on the limiting dome height results [18, 20, 21] which show a lower formability of TWBs than the individual base metals, tend to be conservative in determining the maximum FLD_0 value [1]. To avoid the sporadic breakage due to the day-to-day variations in the stamping process conditions, a safety factor of 10% major strain below the maximum FLD_0 value was suggested by Raghavan *et al.* [7]. This safety factor, which is the most common method used in the press shop, further lowers the maximum FLD_0 of a TWB. Based on this, the observation of the present work is of interest since it shows that the formability of a TWB can be superior to that of the corresponding thinner sheet.

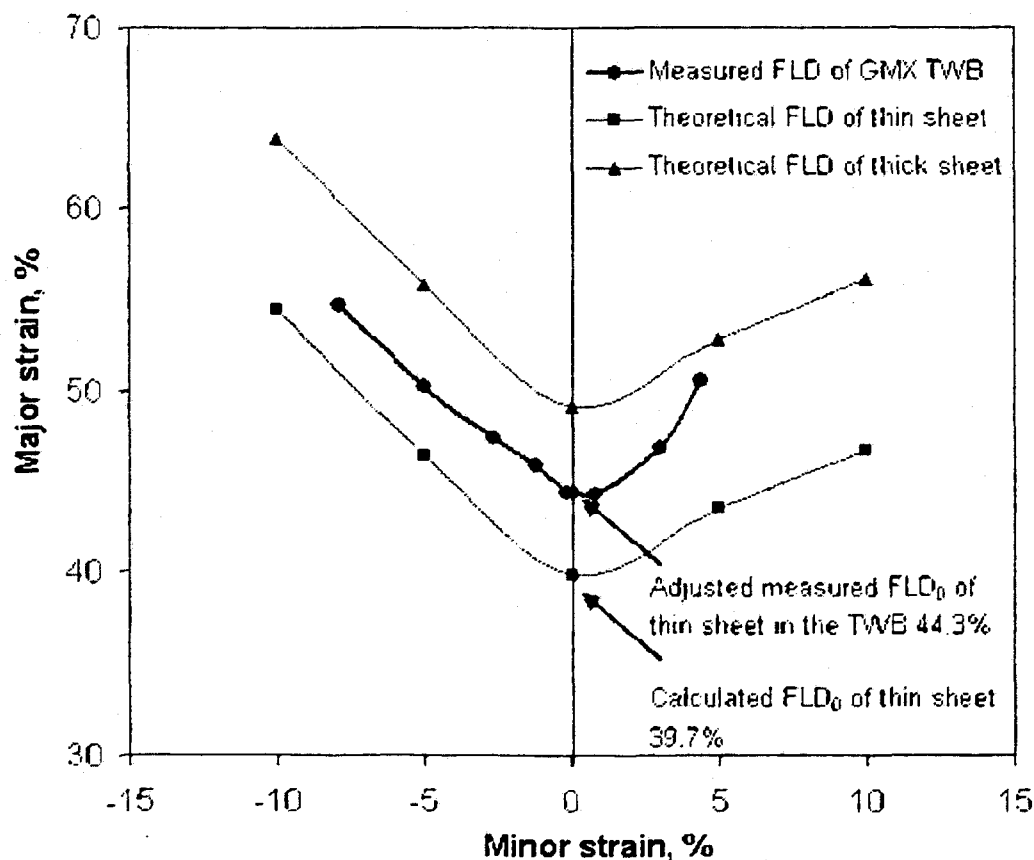


Figure 5.6. Forming limit diagram for GMX TWB combination.

The above findings can be explained as follows. While forming the TWBs, the weld bead, which has a higher hardness than the base metals (Figure 5.3), was found to shift towards the thicker section. This is attributed to the fact that no significant deformation occurred in the weld bead and the thicker section, which was evident by the etched grid pattern. During the forming process, the square grids on the weld bead and the thicker section side did not show any change in shape. Thus, only elastic deformation occurred in the weld bead and the thicker section. The plastic deformation during forming concentrates in the thinner section only. The use of shims to provide a balanced clamping force and lubricants (mill oil, plastic sheet and rubber puck) to reduce the interface friction may have uniformly distributed and increased the limit strains, leading to the increase in the FLD_0 of the TWB.

Shi *et al.* [18] reported similar observations in their work on different thickness TWBs. By positioning the weld bead perpendicular to the major strain direction, they were able to obtain maximum formability performance. In order to achieve a higher formability, they recommend using good lubrication, reducing the severity of the draw beads, applying uniform blank holding pressures and appropriately placing the weld bead. They have also mentioned that by optimizing the welding parameters and/or by using more formable steels like IF and extra low carbon steels may result in a more formable weld and lead to higher limit strains, which is confirmed by the results obtained in the present work.

Similar results to those of GMX TWB were observed for the W-Car and MC-DI TWB combinations (Table 5.3), where the material grade and thickness combinations were different from the GMX TWB and so was the difference in the yield strengths of the base materials constituting these blanks.

The W-Car TWB combination has a thickness difference of 0.92 mm. The adjusted measured FLD_0 value for this TWB was found to be at 47.5% major strain. The calculated FLD_0 of the thinner sheet of the W-Car TWB was found to be at 38.8%

major strain. This combination showed an 8.7% increase in the formability of the TWB as compared to the thinner base metal (Figure 5.7).

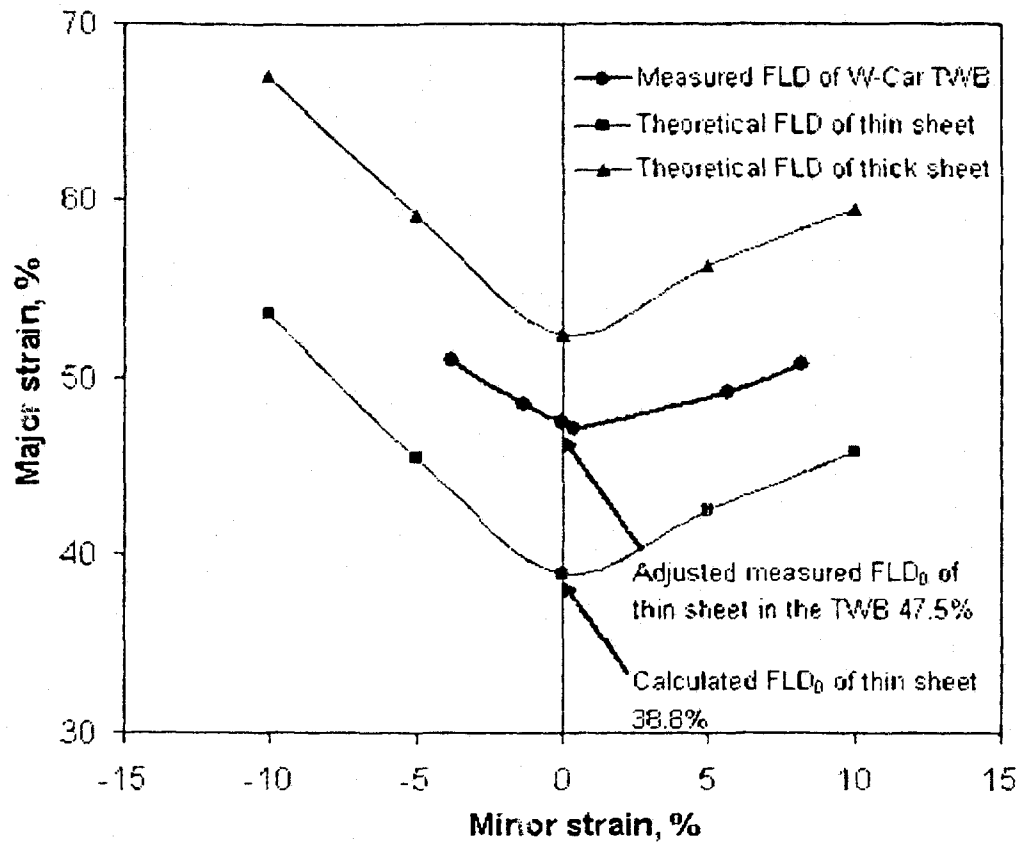


Figure 5.7. Forming limit diagram for W-Car TWB combination.

Similarly, for the MC-DI TWB combination, the thickness difference was 1.2 mm and the yield strength difference was 9 MPa. This combination showed a 7.7% increase in the FLD₀ value (Figure 5.8). The results are summarized in Table 5.3.

Table 5.3. Percentage increase in the FLD_0 values of TWBs.

I.D.	Calculated FLD_0 of thin sheet (%)	Adjusted measured FLD_0 of the TWB (%)	Percentage increase in FLD_0
GMX	39.7	44.3	4.7
W-Car	38.8	47.5	8.7
MC-DI	40.7	48.4	7.7

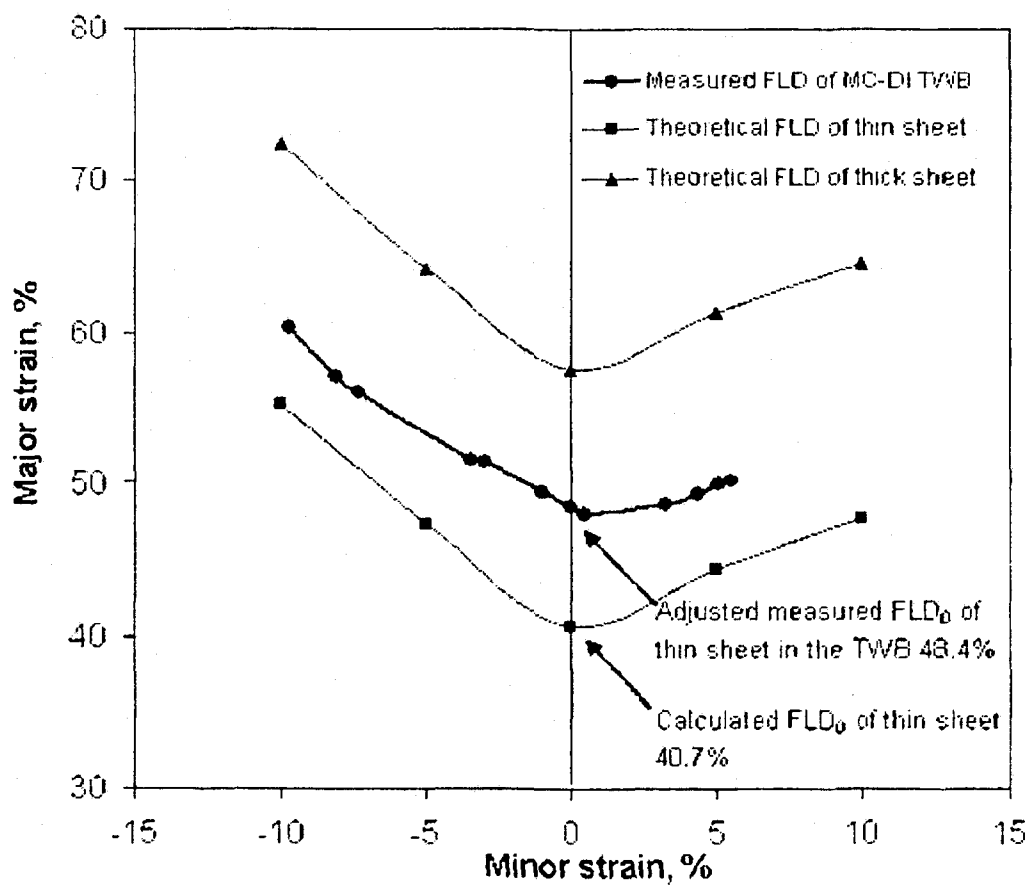


Figure 5.8. Forming limit diagram for MC-DI TWB combination.

5.4 On Fatigue Strength

The S-N curves for the three TWB combinations and the base metal have been given in Figure 4.7. It is seen that the fatigue limit of the uncoated TWB combination (GMX) was 1.4 times higher than that of zinc coated W-Car and MC-DI. The results also show a difference of 10 MPa in the fatigue limit of GMX TWB and the base metal (BM), which was probably related to the experimental error during the machining/polishing of the gauge section. In view of this, the data are represented with the error bars in Figure 4.7. The fatigue ratio of the fatigue limit of the TWBs to the ultimate tensile strength (UTS) of the thinner sections of the TWBs, where the fatigue failure occurred, is shown in Table 5.4. The fatigue ratio for the non-galvanized or bare GMX was found to be 1.4 times higher than that for the galvanized W-Car and MC-DI.

It is well known that fatigue properties depend on the surface condition of the material tested. Surface treatments like electroplating generally reduce the fatigue limit of steel. Similar findings have been reported for an age-hardenable aluminum alloy sheet coated with a soft aluminum coating [16]. The particular surface treatment conditions used to produce the coating can have an appreciable effect on the fatigue properties, since large changes in the residual stress, adhesion and hardness of the coating layer can be produced. The processing of galvanized TWBs is somewhat similar to the above mentioned process, in which the steel substrate is coated with a softer layer of molten zinc by adhesion. Residual tensile stresses are generated on the surface of the steel when the molten zinc solidifies and is further subjected to temper rolling or a skin pass operation for a homogeneous texture. This phenomenon can be one of the contributing factors for the lower fatigue limit of the galvanized TWBs.

Table 5.4. Fatigue ratio of the TWBs and BM.

I. D.	Surface condition	Fatigue limit (MPa)	Tensile strength (MPa)	Fatigue ratio
GMX	Bare	120	301	0.40
W-Car	Galvanized	85	305	0.28
MC-DI	Galvanized	85	297	0.29
BM	Bare	110	324	0.34

Even though different failure modes of these TWBs were observed, the fatigue initiation site in all the cases was in the base metal, which was associated with the inclusion or porosity, as shown in Figure 5.9. For the W-Car and MC-DI combinations, the fatigue crack propagated in the thinner base metals (0.75 mm and 0.80 mm, respectively). However, the location of the failure in the thinner base metals was found to vary with the applied stress amplitude. For the stress amplitude of 90, 100 and 110 MPa, the failure occurred close to the weld bead (about 2 mm) and for higher values of 120 and 130 MPa, the observed failure was away (about 6 – 7 mm) from the weld bead. For the bare GMX TWB combination, failure occurred in the thinner (0.9 mm) base metal and was always away (about 6 – 7 mm) from the weld bead for the entire range of applied load (120 – 150 MPa). The notch effect, because of the thickness variation in the TWBs, may have increased the stress concentration around the weld bead. The thickness difference of the base metals for W-Car and MC-DI TWBs (0.90 and 1.2 mm, respectively) is at least 1.5 times more than that of the GMX TWB (0.6 mm). Because of the stress concentration caused by such a big difference, failure close to the weld bead was observed. Similar results have also been reported by others [22-25].

Rhee *et al.* [24] compared different specimen geometries with the weld bead running both parallel and perpendicular to the loading direction. For the specimens that were loaded perpendicular to the weld bead, crack initiation and final fracture occurred in

the base metal. The crack initiation in the base metal was attributed to the higher fatigue resistance of the weld bead than the base metal. Oh *et al.* [25] found the fatigue limit of similar thickness TWBs to be higher than the dissimilar ones. This was attributed to the notch effect caused by the discontinuous face which induced stress concentration and decreased the fatigue limit. Also, Lazzarin *et al.* [23], while evaluating different welding processes, reported that visual examination of specimens under stress did not reveal any apparent transverse necking in the weld bead. Lee *et al.* [26] found that the fatigue failure in the case of mash seam welded blanks occurred in the heat affected zone, while laser welded blanks failed in the base metal. The mash seam welds had a greater notch effect than the laser welds and thus lower fatigue strength under pulsating tensile stresses.

The fatigue crack propagation in both the W-Car and MC-DI, with the zinc layer, exhibited intergranular cracking together with secondary cracks (Figure 5.10(a) and (b)). The presence of the zinc was confirmed by EDS analysis, as shown in Figure 5.11. For the GMX, without zinc coating, and the BM, the fatigue crack propagation was basically characterized by the fatigue striation-like features, as shown in Figure 5.12. EDS analysis revealed that the fracture surface in both the GMX and BM specimens was free of zinc layer, Figure 5.13. These SEM observations clearly indicated that the lower fatigue strength/limit in the galvanized W-Car and MC-DI TWBs is the consequence of intergranular cracking, caused by the zinc penetrating beneath the sheet surface. This conforms to the above mentioned findings that the surface condition is indeed one of the major factors affecting the fatigue life of materials.

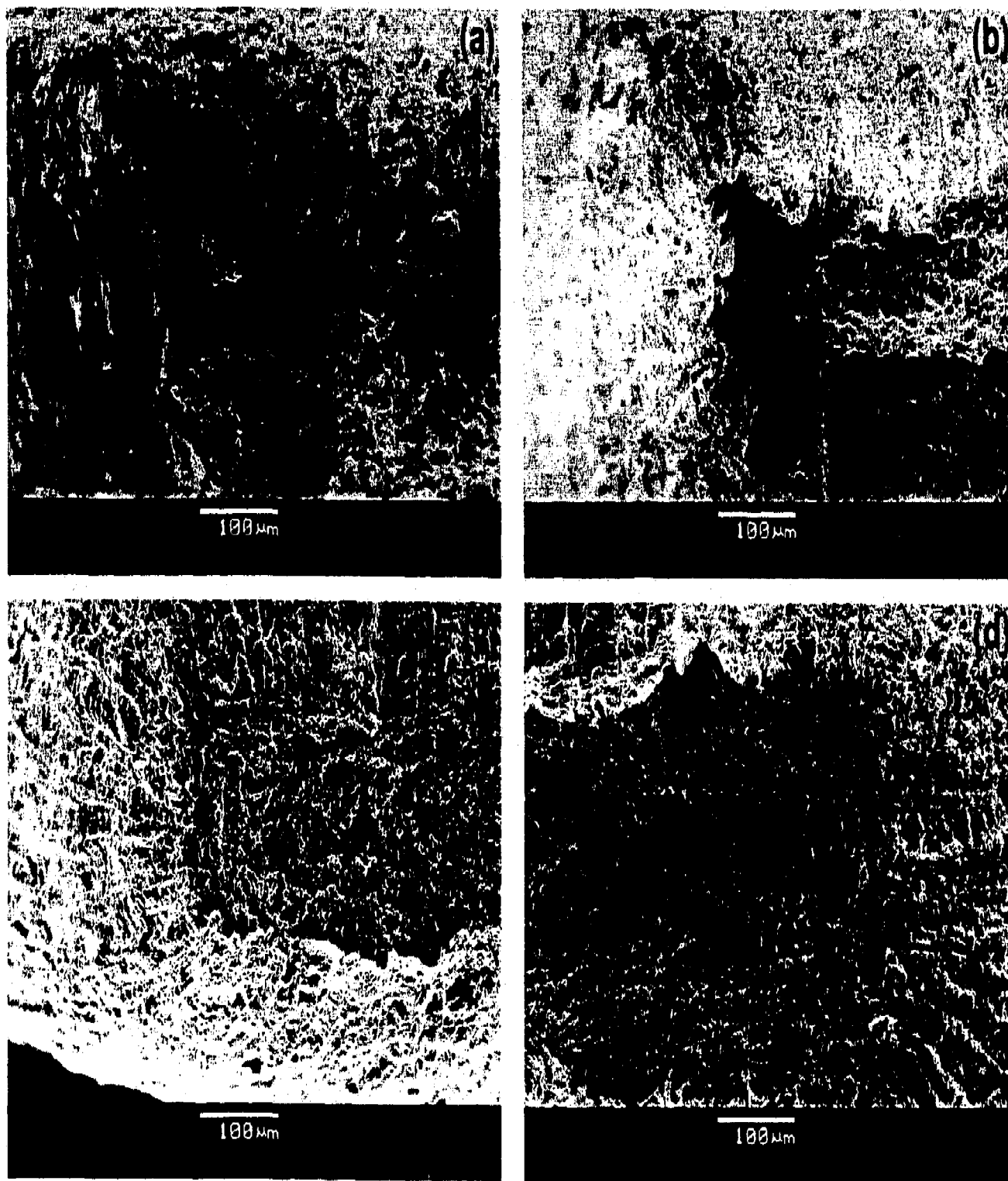


Figure 5.9. Typical SEM micrographs showing the fatigue initiation sites. (a) W-Car (b) MC-DI (c) GMX and (d) BM.

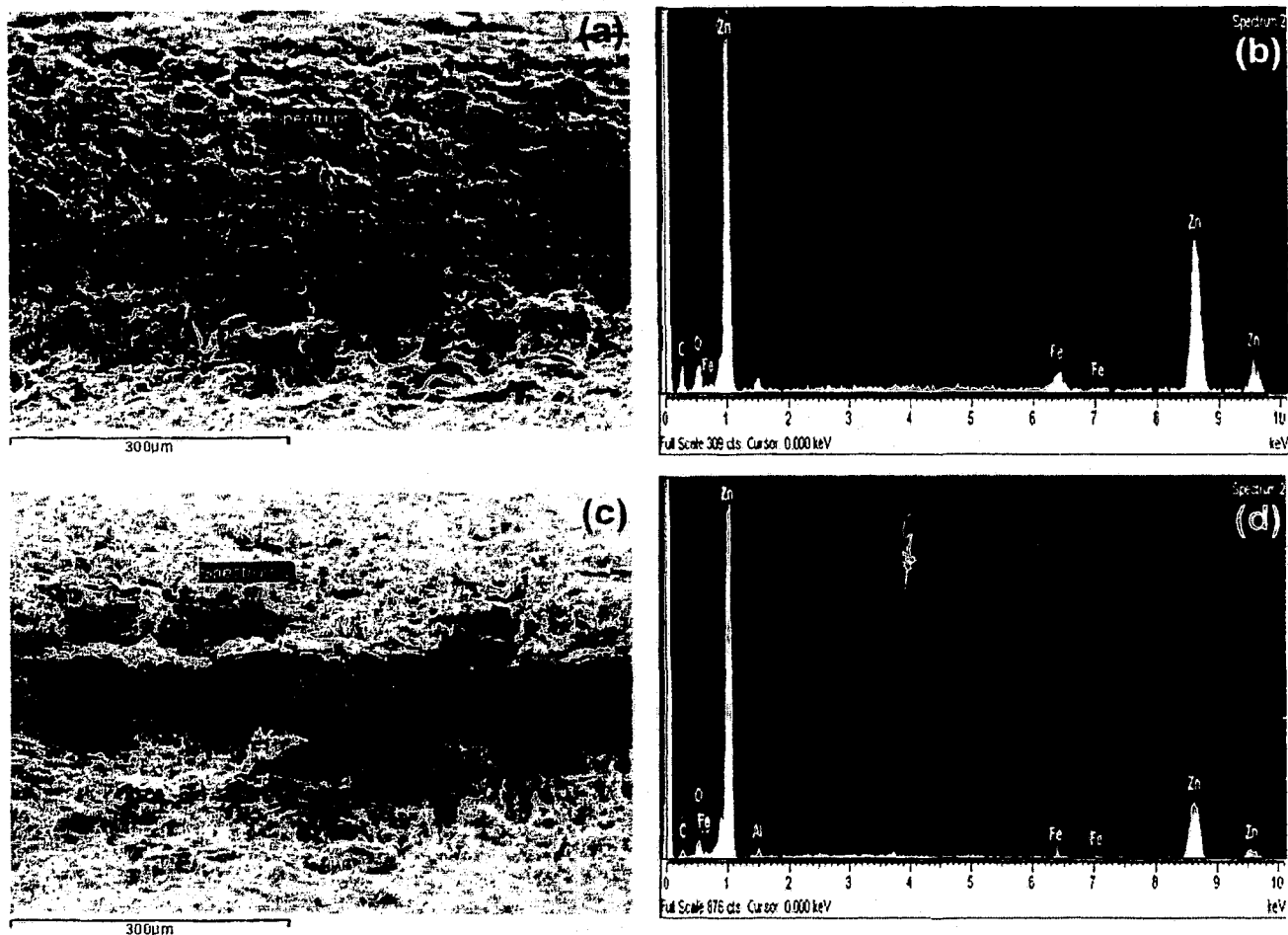


Figure 5.11. Low-magnification SEM micrograph showing an overall view of the fracture surfaces and the corresponding EDS spectrum. (a) and (b) W-Car (c) and (d) MC-DI.

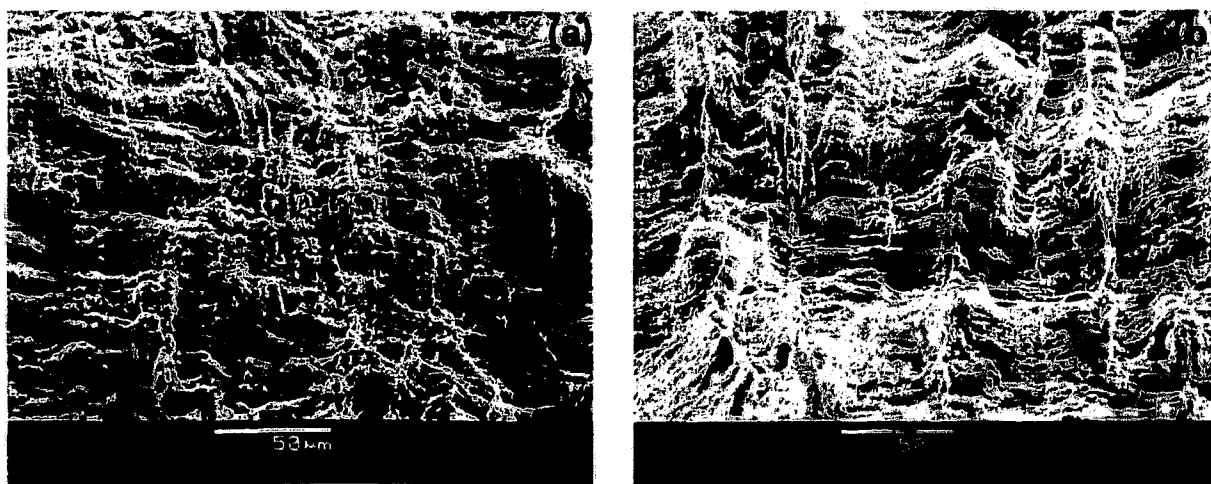


Figure 5.12. SEM micrograph showing the area of fatigue crack growth. (a) GMX (b) BM.

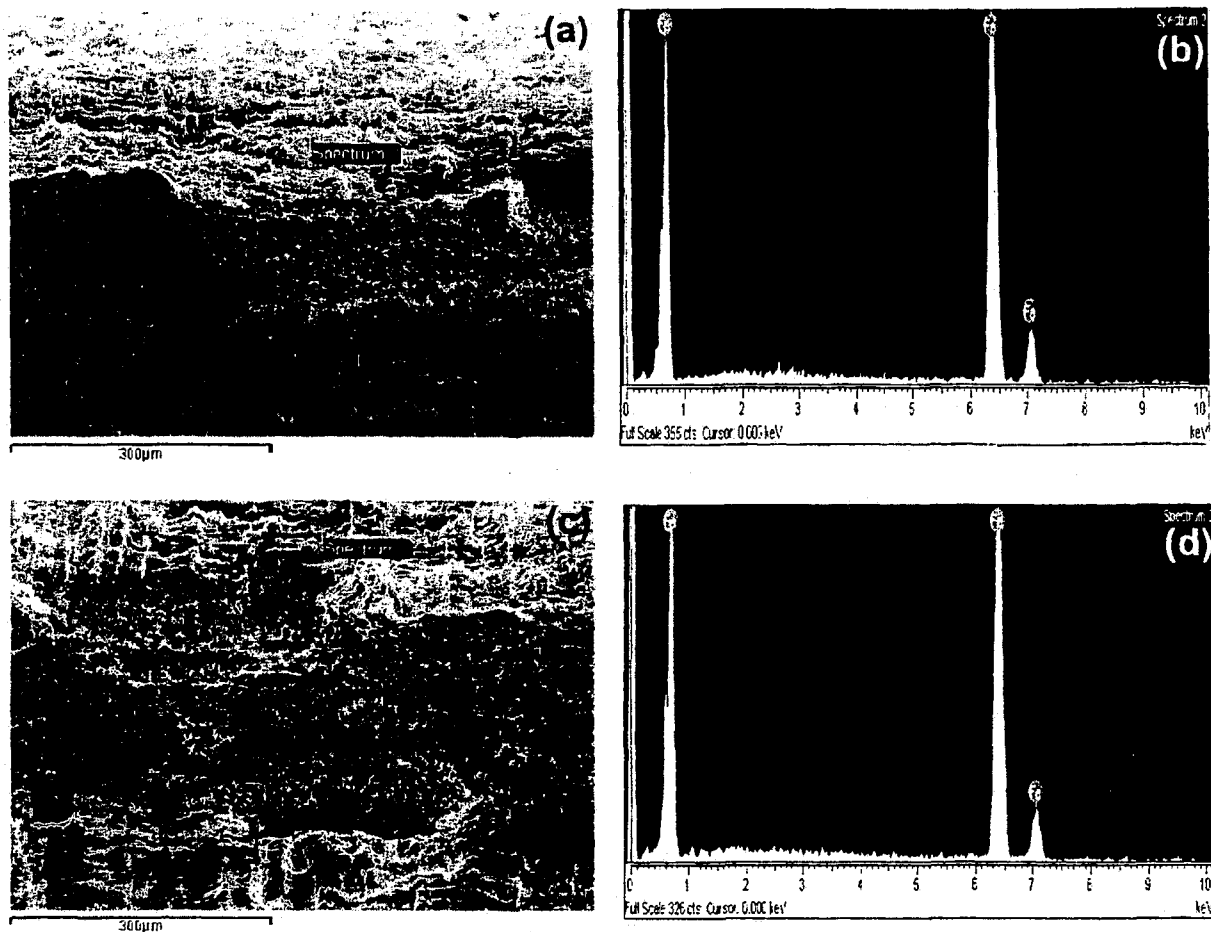


Figure 5.13. Low-magnification SEM micrograph showing an overall view of the fracture surfaces and the corresponding EDS spectrum. (a) and (b) GMX (c) and (d) BM.

Chapter 6

Conclusions

6.1 Summary

The main objective of this study was to evaluate the formability and fatigue strength of tailor welded blanks consisting of highly formable interstitial free and very low carbon steels. The experimental results yielded the following conclusions:

1. The microstructural examination of the weld cross-sections revealed that the welds were free of any significant amount of defects such as porosity, concavity, voids, inclusions or misalignments. This indicated that the welding parameters used for the TWBs are appropriate to obtain sound welds.
2. The microhardness of the weld bead after laser welding was approximately 2.5 times higher than that of the individual base metals constituting the TWBs. This is attributed to the fine pearlite and low carbon bainite structure in the weld metal as compared to the constituent base metals which showed the presence of equiaxed grains of ferrite.
3. With a careful selection of laser welding parameters and weld bead position, there is a very little likelihood of forming failure in the weld and/or the heat-affected zone of the TWBs, indicating the soundness in the weld quality. The forming failures occurred in the thinner section, indicating that the formability of the TWBs is basically dependent on that of the thinner sheet.
4. A semi-empirical relation is proposed to calculate the $FLD_{0(TWB)}$ value based on the North American Deep Drawing Equation, the mean value of the strain-hardening exponents (n_{TWB}) and the mean value of the thicknesses (t_{TWB}) of the base metals, which can be expressed as,

$$FLD_{0(TWB)} = \frac{n_{TWB}}{0.21} (14.1 \times t_{TWB} + 23.3)$$

The FLD_0 results of the TWBs calculated using this equation are in good agreement with the experimentally determined FLD_0 values.

5. For the selected grades of steel, it is found that the FLD_0 's of the TWBs are in-between those of the individually formed sheets of the TWBs. This is attributed to the use of better lubrication and a balanced clamping force that increased the limit strains leading to the increase in the FLD_0 value of the TWBs.
6. The fatigue limit of the bare TWB was found to be about 1.4 times higher than that of the galvanized TWBs.
7. Fatigue fracture was observed to occur always in the thinner sheet of the TWBs. However, the location of the fracture seemed to vary due to the stress concentration induced by the difference in the thicknesses of the sheets. The thickness difference for the W-Car and MC-DI TWBs was at least 1.5 times more than that of the GMX TWB. The failure in the W-Car and MC-DI TWBs was relatively close to the weld bead whereas for GMX TWB the failure always occurred away from the weld.
8. The fatigue crack propagation in the base metal (BM) and bare GMX TWB was mainly characterized by fatigue striations, whereas the galvanized TWBs exhibited intergranular cracking caused by the presence of zinc penetrating beneath the sheet surface. This is the major reason why the fatigue strength/limit of galvanized (W-Car and MC-DI) TWBs is much lower than that of bare (GMX) TWB.

6.2 Recommendations for Future Work

The present work was based on tailor welded blanks having similar material combinations in terms of grades of steels. Similar work can be carried out when two different types of steels like DP and IF are welded to form a tailor welded blank. With recent advances in the laser welding process, it is necessary to determine the effect of welding parameters and filler materials (if any) on the formability and fatigue properties of the weld bead. Also, the effect of various lubricants on the formability of tailor welded blanks can be analyzed using draw bead simulator test. It would be of interest to compare the forming results from the laboratory tests with an actual production part in terms of the weld bead location and different forming modes generated on the same stamping.

References

- [1] Auto/Steel Partnership, "Tailor welded blanks design and manufacturing manual", 1998, Technical report.
- [2] Forming Technologies Incorporated, "Basic formability: From product design to die tryout", July 1999, Technical report, Rev. 3.
- [3] Z. Marciniak and J. L. Duncan, "Principles of plastic flow theory and Experimental strain analysis", Topics in the mechanics of sheet metal forming, Edward Arnold - A division of Hodder and Stoughton, 1992, pp. 1-41.
- [4] S. P. Keeler, "Determination of forming limits in automotive stampings", SAE Technical Paper, 1965, 650535, pp. 1-9.
- [5] G. M. Goodwin, "Application of strain analysis to sheet metal forming problems in the press shop", SAE Technical Paper, 1968, 680093, pp. 380-387.
- [6] S. P. Keeler, "Circular grid system – A valuable aid for evaluating sheet metal formability", SAE Technical Paper, 1968, 680092, pp. 371-379.
- [7] K. S. Raghavan, R. C. Van Kuren and H. Darlington, "Recent progress in the development of forming limit curves for automotive sheet steels", SAE Technical Paper, 1992, 920437, pp. 87-104.
- [8] S. P. Keeler and W. G. Brazier, "Relationship between material characterization and press-shop formability", Microalloying 75, 1975, New York, pp. 517-530.
- [9] "Electrochemical Marking Manual", The Electroetch Company, 1996, pp. 1-20.

- [10] Annual Book of ASTM Standards, "Standard test methods for determining forming limit curves", 2002, Designation: E 2218-02, Vol. 03.01, pp. 1237-1251.
- [11] J. H. Vogel and D. Lee, "The automated measurement of strains from three dimensional deformed surface", Journal of Minerals, Metals and Materials, 1990, Vol. 42, No. 2, pp. 8-13.
- [12] M. F. Shi and D. J. Meuleman, "An evaluation of interface friction in different forming models for coated steel sheets", SAE Technical Paper, 1992, 920633, pp. 35-142.
- [13] S. P. Keeler, H. D. Nine and J. F. Siekirk, "Formability criteria for selecting sheet metal lubricants", SAE Technical Paper, 1988, 880366, pp. 49-60.
- [14] Annual Book of ASTM Standards, "Standard test methods for ball punch deformation of metallic sheet material", 2002, Designation: E 643-84, Vol. 03.01, pp. 603-606.
- [15] A. Gustavsson, M. Larsson and A. Melander, "Fatigue life of pressed steel sheet components", International Journal of Fatigue, 1997, Vol. 19, Nos. 8-9, pp. 613-619.
- [16] G. E. Dieter, "Fatigue of metals", Topic in mechanical metallurgy, McGraw Hill Book Company (UK) Ltd., 1988, pp. 375-431.
- [17] Metals Handbook, "Fractography", Ninth Edition, 1987, Vol. 12, ASM International, Metals Park, Ohio, pp. 261.
- [18] M. F. Shi, K. M. Pickett and K. K. Bhatt, "Formability issues in the application of tailor welded blank sheets", SAE Technical Paper, 1993, 930278, pp. 27-35.

- [19] S. M. Chan, L. C. Chan and T. C. Lee, "Tailor-welded blanks of different thickness ratios effects on forming limit diagrams", *Journal of Materials Processing Technology*, 2003, No. 132, pp. 95-101.
- [20] S. M. Chan, L. C. Chan and T. C. Lee, "Deformation mode analysis of forming limit diagrams for tailor-welded blanks", *SAE Technical Paper*, 2001, 010092, pp. 1-8.
- [21] B. Y. Ghoo, S. W. Park and Y. T. Keum, "New forming limit diagram of laser tailored blank", *Journal of Strain Analysis*, 2001, Vol. 36, No. 2, pp. 143-152.
- [22] P. C. Wang and K. M. Ewing, "A comparison of fatigue strengths: Laser beam vs. resistance spot welds", *Welding Journal (USA)*, October 1991, Vol. 70, No. 10, pp. 43-47.
- [23] P. Lazzarin, E. Rabino, and D. Zandonella Necca, "Fatigue behaviour of laser and resistance seam welds in the automotive industry", *Welding International (UK)*, 1995, Vol. 9, No. 1, pp. 165-172.
- [24] K. Y. Rhee, D. S. Kwak and T. Y. Oh, "Fatigue behavior characterization of laser-welded cold rolled sheet metal (SPCEN)", *Journal of Materials Science*, 2002, Vol. 37, No. 5, pp. 1019-1025.
- [25] T. Y. Oh, Y. K. Kwon, C. J. Lee and D. S. Kwak, "The characteristics of fatigue strength in laser tailored welded blanking sheet metal", *Key Engineering Materials*, 2000, Vols. 183-187, pp. 1321-1326.
- [26] A. P. Lee, E. Feltham and J. V. Deventer, "Tailor welded blank technology for automotive applications", *SAE Technical Paper*, 1996, 960817, pp. 91-102.

- [27] R. Aristotile and M. Fersini, "Tailored blank's for automotive components. Evaluation of mechanical and metallurgical properties and corrosion resistance of laser-welded joints", *Welding International (UK)*, 1999, Vol. 13, No. 3, pp. 16-25.
- [28] J. Onoro and C. Ranninger, "Fatigue behaviour of laser welds of high-strength low-alloy steels", *Journal of Materials Processing Technology*, 1997, Vol. 68, No. 1, pp. 68-70.
- [29] M. P. Sklad, "Aspects of automated measurement of proportional and non-proportional deformation in sheet metal forming", *Journal of Materials Processing Technology*, 2004, Vol. 145, No. 3, pp. 377-384.
- [30] Annual Book of ASTM Standards, "Standard test methods for tension testing of metallic materials [Metric]", 2002, Designation: E 8M, Vol. 03.01, pp. 83-104.
- [31] Annual Book of ASTM Standards, "Standard test methods for tensile strain-hardening exponents (n-values) of metallic materials", 2002, Designation: E 646-00, Vol. 03.01, pp. 607-614.
- [32] Annual Book of ASTM Standards, "Standard practice for conducting force controlled constant amplitude axial fatigue tests of metallic materials", 2002, Designation: E 466-96, Vol. 03.01, pp. 515-519.
- [33] Struers Inc. webpage, "<http://www.struers.com/modules/emetalog/login.asp>", as on July 10, 2004.
- [34] P. Andreychuk, "Regression analysis for predicting the forming limit diagram of sheet metal", Dofasco Internal Report.

[35] T. Gladman, "Properties and applications", Topic in the physical metallurgy of microalloyed steels, The Institute of Materials (UK), 1997, pp. 263-355.

[36] P. Cizek, B. P. Wynne, C. H. J. Davies, B. C. Muddle and P. D. Hodgson, "Effect of composition and austenite deformation on the transformation characteristics of low-carbon and ultralow-carbon microalloyed steels", Metallurgical and Materials Transactions A, 2002, Vol. 33A, No. 5, pp. 1331-1349.

[37] E. Biro, "Characterization of the microstructure and hardness profile of a low carbon tube welded under normal operating conditions", Dofasco Report, June 2003, No. 0051/RR/03, pp. 1-10.

Appendix A

Sample calculations for determining the strain-hardening exponent (n-value) of the base metal (BM) of thickness 1.5 mm.

The true stress and true strain to be substituted in Eq. 2.1 were calculated from the following equations [31]:

$$\text{True stress, } \sigma = S (1 + e), \quad (\text{A.1})$$

$$\text{True strain, } \epsilon = \ln (1 + e), \quad (\text{A.2})$$

where S = Engineering stress,
e = Engineering strain.

The equation for the slope of the linear regression line for calculating the strain-hardening exponent (n-value) is as follows:

$$n = \frac{N \sum_{i=1}^N (\log \epsilon_i \log \sigma_i) - \left(\sum_{i=1}^N \log \epsilon_i \sum_{i=1}^N \log \sigma_i \right)}{N (\log \epsilon_i)^2 - \left(\sum_{i=1}^N \log \epsilon_i \right)^2} \quad (\text{A.3})$$

where n = Strain-hardening exponent,
N = Number of data pairs.

The above Eq. (A.3) is made more convenient by a symbolic representation of terms as,

$$Y = \log \sigma,$$

$$X = \log \epsilon,$$

N = Number of data pairs,

n = Strain-hardening exponent (n-value).

Based on the above representation, the simplified form of Eq. (A.3) is given as follows:

$$n = \frac{N \sum XY - \sum X \sum Y}{N \sum X^2 - (\sum X)^2} \quad (A.4)$$

The following worksheet shows the data and calculations for the base metal (BM) of thickness 1.5 mm.

Data pair	Load, P, kips	Engg. stress, ksi	True stress, σ , ksi	Y , $\log_{10} \sigma$	Y^2	Engg. strain, %	Engg. strain, e	True strain, ϵ	X , $\log_{10} \epsilon$	X^2	XY
1	1.253	41.051	45.167	1.655	2.738	10.026	0.100	0.096	-1.020	1.040	-1.688
2	1.255	41.092	45.254	1.656	2.741	10.129	0.101	0.096	-1.016	1.031	-1.681
3	1.254	41.074	45.267	1.656	2.742	10.210	0.102	0.097	-1.012	1.025	-1.676
4	1.259	41.231	45.485	1.658	2.749	10.317	0.103	0.098	-1.008	1.016	-1.671
5	1.258	41.191	45.484	1.658	2.748	10.422	0.104	0.099	-1.004	1.007	-1.664
6	1.260	41.280	45.595	1.659	2.752	10.452	0.105	0.099	-1.003	1.005	-1.663
7	1.262	41.325	45.705	1.660	2.755	10.598	0.106	0.101	-0.997	0.994	-1.655
8	1.265	41.442	45.875	1.662	2.761	10.696	0.107	0.102	-0.993	0.986	-1.650
9	1.267	41.483	45.958	1.662	2.763	10.788	0.108	0.102	-0.990	0.979	-1.645
10	1.267	41.492	46.011	1.663	2.765	10.891	0.109	0.103	-0.986	0.971	-1.639
11	1.268	41.514	46.073	1.663	2.767	10.982	0.110	0.104	-0.982	0.965	-1.634
12	1.270	41.582	46.183	1.664	2.771	11.067	0.111	0.105	-0.979	0.958	-1.629
13	1.272	41.654	46.300	1.666	2.774	11.156	0.112	0.106	-0.976	0.952	-1.625
14	1.272	41.645	46.337	1.666	2.775	11.267	0.113	0.107	-0.972	0.944	-1.619
15	1.272	41.667	46.403	1.667	2.777	11.365	0.114	0.108	-0.968	0.937	-1.613
16	1.274	41.734	46.522	1.668	2.781	11.470	0.115	0.109	-0.964	0.930	-1.608
17	1.276	41.802	46.626	1.669	2.784	11.541	0.115	0.109	-0.962	0.925	-1.605
18	1.280	41.937	46.820	1.670	2.790	11.644	0.116	0.110	-0.958	0.918	-1.600
19	1.280	41.923	46.853	1.671	2.791	11.758	0.118	0.111	-0.954	0.910	-1.594
20	1.280	41.914	46.879	1.671	2.792	11.844	0.118	0.112	-0.951	0.904	-1.589
21	1.283	42.013	47.031	1.672	2.797	11.943	0.119	0.113	-0.948	0.898	-1.585
22	1.283	42.022	47.083	1.673	2.798	12.045	0.120	0.114	-0.944	0.891	-1.579
23	1.282	42.000	47.092	1.673	2.799	12.125	0.121	0.114	-0.941	0.886	-1.575
24	1.285	42.094	47.242	1.674	2.803	12.229	0.122	0.115	-0.938	0.880	-1.570

Data pair	Load, P, kips	Engg. stress, ksi	True stress, σ , ksi	Y , $\log_{10}\sigma$	Y^2	Engg. strain, %	Engg. strain, e	True strain, ϵ	X , $\log_{10}\epsilon$	X^2	XY
25	1.285	42.071	47.266	1.675	2.804	12.347	0.123	0.116	-0.934	0.872	-1.564
26	1.285	42.094	47.322	1.675	2.806	12.420	0.124	0.117	-0.932	0.868	-1.560
27	1.289	42.224	47.509	1.677	2.812	12.517	0.125	0.118	-0.928	0.862	-1.557
28	1.288	42.188	47.513	1.677	2.812	12.622	0.126	0.119	-0.925	0.856	-1.551
29	1.290	42.256	47.630	1.678	2.815	12.719	0.127	0.120	-0.922	0.850	-1.547
30	1.292	42.310	47.732	1.679	2.818	12.815	0.128	0.121	-0.919	0.844	-1.542
31	1.291	42.296	47.760	1.679	2.819	12.919	0.129	0.121	-0.915	0.838	-1.537
32	1.293	42.341	47.848	1.680	2.822	13.007	0.130	0.122	-0.913	0.833	-1.533
33	1.295	42.427	47.981	1.681	2.826	13.091	0.131	0.123	-0.910	0.828	-1.530
34	1.296	42.431	48.036	1.682	2.828	13.209	0.132	0.124	-0.906	0.821	-1.524
35	1.294	42.364	48.002	1.681	2.827	13.309	0.133	0.125	-0.903	0.816	-1.519
36	1.294	42.386	48.030	1.682	2.827	13.316	0.133	0.125	-0.903	0.816	-1.519
37	1.298	42.512	48.219	1.683	2.833	13.424	0.134	0.126	-0.900	0.810	-1.514
38	1.297	42.467	48.200	1.683	2.833	13.500	0.135	0.127	-0.897	0.805	-1.510
39	1.300	42.588	48.386	1.685	2.838	13.612	0.136	0.128	-0.894	0.799	-1.506
40	1.301	42.593	48.436	1.685	2.840	13.718	0.137	0.129	-0.891	0.794	-1.501
41	1.298	42.503	48.374	1.685	2.838	13.814	0.138	0.129	-0.888	0.789	-1.496
42	1.304	42.696	48.636	1.687	2.846	13.911	0.139	0.130	-0.885	0.784	-1.493
43	1.302	42.629	48.604	1.687	2.845	14.016	0.140	0.131	-0.882	0.778	-1.488
44	1.304	42.705	48.727	1.688	2.849	14.100	0.141	0.132	-0.880	0.774	-1.485
45	1.306	42.773	48.816	1.689	2.851	14.130	0.141	0.132	-0.879	0.772	-1.484
46	1.304	42.705	48.823	1.689	2.851	14.325	0.143	0.134	-0.873	0.763	-1.475
47	1.306	42.759	48.920	1.689	2.854	14.409	0.144	0.135	-0.871	0.758	-1.471
48	1.307	42.795	49.010	1.690	2.857	14.522	0.145	0.136	-0.868	0.753	-1.467
49	1.306	42.773	49.018	1.690	2.857	14.602	0.146	0.136	-0.866	0.749	-1.463
50	1.309	42.876	49.185	1.692	2.862	14.715	0.147	0.137	-0.862	0.744	-1.459
51	1.307	42.818	49.168	1.692	2.862	14.831	0.148	0.138	-0.859	0.738	-1.454
52	1.308	42.854	49.244	1.692	2.864	14.913	0.149	0.139	-0.857	0.734	-1.450
53	1.311	42.943	49.393	1.694	2.868	15.019	0.150	0.140	-0.854	0.730	-1.447
54	1.309	42.876	49.362	1.693	2.868	15.127	0.151	0.141	-0.851	0.725	-1.441
55	1.312	42.979	49.519	1.695	2.872	15.215	0.152	0.142	-0.849	0.721	-1.439
56	1.312	42.984	49.572	1.695	2.874	15.327	0.153	0.143	-0.846	0.715	-1.434
57	1.312	42.966	49.596	1.695	2.875	15.431	0.154	0.144	-0.843	0.711	-1.429
58	1.312	42.984	49.652	1.696	2.876	15.514	0.155	0.144	-0.841	0.707	-1.426
59	1.315	43.060	49.784	1.697	2.880	15.614	0.156	0.145	-0.838	0.703	-1.423
60	1.315	43.074	49.849	1.698	2.882	15.730	0.157	0.146	-0.835	0.698	-1.418
61	1.313	42.997	49.802	1.697	2.881	15.826	0.158	0.147	-0.833	0.694	-1.414
62	1.317	43.119	50.002	1.699	2.887	15.963	0.160	0.148	-0.829	0.688	-1.409
63	1.311	42.921	49.808	1.697	2.881	16.046	0.160	0.149	-0.827	0.685	-1.404
64	1.317	43.132	50.089	1.700	2.889	16.130	0.161	0.150	-0.825	0.681	-1.403
65	1.319	43.186	50.203	1.701	2.892	16.247	0.162	0.151	-0.822	0.676	-1.399
66	1.320	43.227	50.299	1.702	2.895	16.362	0.164	0.152	-0.819	0.672	-1.394
67	1.320	43.227	50.335	1.702	2.896	16.444	0.164	0.152	-0.817	0.668	-1.391

Data pair	Load, P, kips	Engg. stress, ksi	True stress, σ , ksi	Y, $\log_{10}\sigma$	Y^2	Engg. strain, %	Engg. strain, ϵ	True strain, ϵ	X, $\log_{10}\epsilon$	X^2	XY
68	1.320	43.222	50.371	1.702	2.897	16.541	0.165	0.153	-0.815	0.664	-1.387
69	1.321	43.276	50.488	1.703	2.901	16.665	0.167	0.154	-0.812	0.659	-1.383
70	1.322	43.294	50.552	1.704	2.903	16.764	0.168	0.155	-0.810	0.656	-1.380
71	1.321	43.276	50.584	1.704	2.904	16.886	0.169	0.156	-0.807	0.651	-1.375
72	1.321	43.263	50.567	1.704	2.903	16.885	0.169	0.156	-0.807	0.651	-1.375
73	1.321	43.263	50.604	1.704	2.904	16.969	0.170	0.157	-0.805	0.648	-1.372
74	1.321	43.263	50.644	1.705	2.905	17.062	0.171	0.158	-0.803	0.644	-1.368
75	1.324	43.370	50.817	1.706	2.910	17.169	0.172	0.158	-0.800	0.640	-1.365
76	1.327	43.451	50.968	1.707	2.915	17.299	0.173	0.160	-0.797	0.635	-1.361
77	1.323	43.325	50.856	1.706	2.912	17.382	0.174	0.160	-0.795	0.632	-1.357
78	1.325	43.388	50.970	1.707	2.915	17.475	0.175	0.161	-0.793	0.629	-1.354
79	1.325	43.379	51.011	1.708	2.916	17.592	0.176	0.162	-0.790	0.625	-1.350
80	1.325	43.397	51.074	1.708	2.918	17.689	0.177	0.163	-0.788	0.621	-1.346
81	1.326	43.429	51.161	1.709	2.920	17.805	0.178	0.164	-0.786	0.617	-1.342
82	1.324	43.375	51.145	1.709	2.920	17.913	0.179	0.165	-0.783	0.613	-1.338
83	1.325	43.393	51.204	1.709	2.922	18.001	0.180	0.166	-0.781	0.610	-1.335
84	1.328	43.496	51.371	1.711	2.927	18.105	0.181	0.166	-0.779	0.607	-1.332
85	1.327	43.465	51.389	1.711	2.927	18.231	0.182	0.167	-0.776	0.602	-1.328
86	1.326	43.424	51.380	1.711	2.927	18.321	0.183	0.168	-0.774	0.599	-1.324
87	1.329	43.523	51.535	1.712	2.931	18.409	0.184	0.169	-0.772	0.596	-1.322
88	1.327	43.469	51.525	1.712	2.931	18.531	0.185	0.170	-0.770	0.592	-1.317
89	1.329	43.523	51.631	1.713	2.934	18.630	0.186	0.171	-0.767	0.589	-1.315
90	1.330	43.573	51.744	1.714	2.937	18.754	0.188	0.172	-0.765	0.585	-1.311
91	1.327	43.469	51.664	1.713	2.935	18.851	0.189	0.173	-0.763	0.582	-1.307
92	1.328	43.492	51.733	1.714	2.937	18.949	0.189	0.174	-0.761	0.579	-1.304
93	1.329	43.537	51.835	1.715	2.940	19.062	0.191	0.174	-0.758	0.575	-1.300
94	1.329	43.537	51.877	1.715	2.941	19.158	0.192	0.175	-0.756	0.572	-1.297
95	1.331	43.595	51.996	1.716	2.945	19.270	0.193	0.176	-0.754	0.568	-1.294
96	1.329	43.532	51.976	1.716	2.944	19.397	0.194	0.177	-0.751	0.565	-1.289
97	1.330	43.573	52.066	1.717	2.947	19.492	0.195	0.178	-0.749	0.562	-1.286
98	1.332	43.613	52.158	1.717	2.949	19.592	0.196	0.179	-0.747	0.559	-1.283
99	1.332	43.618	52.210	1.718	2.951	19.699	0.197	0.180	-0.745	0.555	-1.280
100	1.333	43.663	52.316	1.719	2.954	19.820	0.198	0.181	-0.743	0.552	-1.277
101	1.332	43.636	52.328	1.719	2.954	19.920	0.199	0.182	-0.741	0.549	-1.273
102	1.333	43.658	52.402	1.719	2.956	20.029	0.200	0.183	-0.739	0.546	-1.270
103	1.334	43.680	52.479	1.720	2.958	20.143	0.201	0.184	-0.736	0.542	-1.266
104	1.334	43.676	52.511	1.720	2.959	20.229	0.202	0.184	-0.735	0.540	-1.264
105	1.333	43.658	52.544	1.721	2.960	20.354	0.204	0.185	-0.732	0.536	-1.260
106	1.333	43.645	52.582	1.721	2.961	20.478	0.205	0.186	-0.730	0.533	-1.256
107	1.334	43.703	52.692	1.722	2.964	20.568	0.206	0.187	-0.728	0.530	-1.254
108	1.336	43.770	52.771	1.722	2.967	20.564	0.206	0.187	-0.728	0.530	-1.254
109	1.336	43.748	52.794	1.723	2.967	20.678	0.207	0.188	-0.726	0.527	-1.250
110	1.334	43.685	52.766	1.722	2.967	20.787	0.208	0.189	-0.724	0.524	-1.247

From the above data, we have,

$$N = 110,$$

$$\Sigma Y = 186.211,$$

$$\Sigma Y^2 = 315.265,$$

$$\Sigma X = -94.078,$$

$$\Sigma X^2 = 81.263,$$

$$\Sigma XY = -159.076.$$

By substituting these values into Eq. (A.4), an n -value of 0.225 can be obtained.

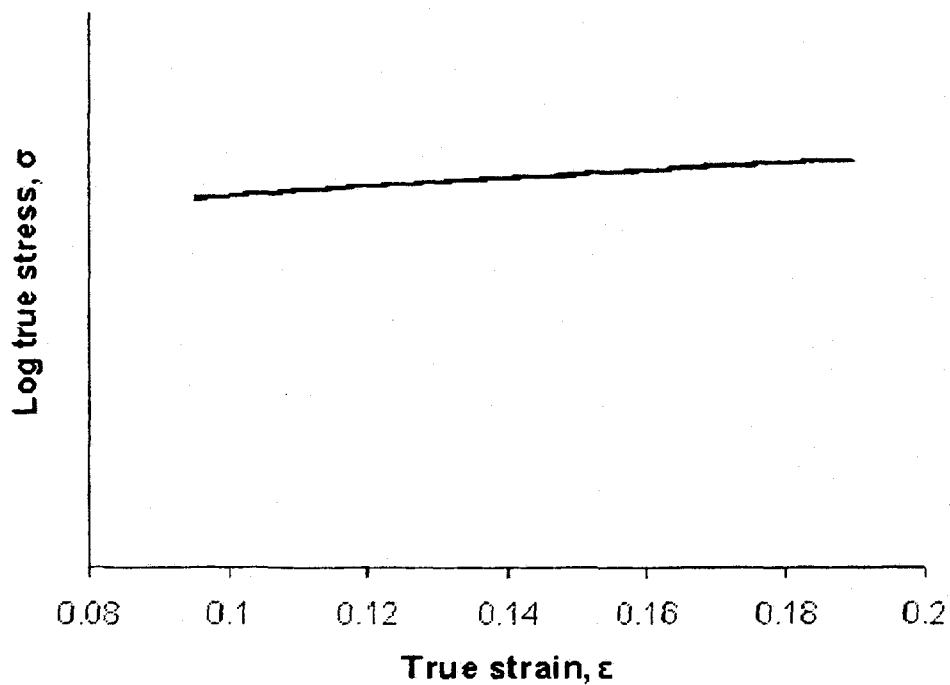


Figure A.1. Log-log plot of true stress-strain curve.

Appendix B

B.1. Microhardness values for GMX tailor welded blank combination.

Distance from the centre of weld, mm	Microhardness, HV
-2.1	111
-2	107
-1.9	116
-1.8	113
-1.7	112
-1.6	117
-1.5	117
-1.4	117
-1.3	120
-1.2	129
-1.1	126
-1	132
-0.9	157
-0.8	202
-0.7	219
-0.6	214
-0.5	201
-0.4	268
-0.3	318
-0.2	308
-0.1	311
0	289
0.1	293
0.2	299
0.3	299
0.4	308
0.5	278
0.6	215
0.7	191
0.8	199

Distance from the centre of weld, mm	Microhardness, HV
0.9	198
1	175
1.1	166
1.2	152
1.3	140
1.4	135
1.5	131
1.6	125
1.7	127
1.8	127
1.9	124
2	124

B.2. Microhardness values for W-Car tailor welded blank combination.

Distance from the centre of weld, mm	Microhardness, HV
-2.1	100
-2	103
-1.9	101
-1.8	101
-1.7	103
-1.6	103
-1.5	102
-1.4	109
-1.3	101
-1.2	109
-1.1	112
-1	117
-0.9	122
-0.8	134
-0.7	145
-0.6	146
-0.5	187
-0.4	268
-0.3	249
-0.2	279
-0.1	260

Distance from the centre of weld, mm	Microhardness, HV
0	268
0.1	256
0.2	246
0.3	253
0.4	195
0.5	155
0.6	144
0.7	142
0.8	134
0.9	119
1	114
1.1	119
1.2	120
1.3	114
1.4	110
1.5	108
1.6	112
1.7	110
1.8	113
1.9	109
2	115

B.3. Microhardness values for MC-DI tailor welded blank combination.

Distance from the centre of weld, mm	Microhardness, HV
-2.1	103
-2	100
-1.9	105
-1.8	101
-1.7	106
-1.6	97
-1.5	106
-1.4	103
-1.3	104
-1.2	102

Distance from the centre of weld, mm	Microhardness, HV
-1.1	108
-1	109
-0.9	111
-0.8	109
-0.7	113
-0.6	105
-0.5	115
-0.4	148
-0.3	245
-0.2	238
-0.1	246
0	214
0.1	217
0.2	229
0.3	204
0.4	152
0.5	130
0.6	106
0.7	111
0.8	107
0.9	107
1	103
1.1	101
1.2	103
1.3	101
1.4	99
1.5	104
1.6	97
1.7	97
1.8	101
1.9	106
2	101

Appendix C

C.1. Major and minor strain values for the GMX tailor welded blank – Safe region.

Minor strain, %	Major strain, %
-16.6	38.3
-22.3	60.1
-16.1	63.1
-23.9	64.4
-24.4	60.6
-24	59.7
-10.6	55
-13.5	51.2
-14.3	46.7
-12.8	64.3
-10.3	48.6
-7.4	50.5
-7.9	54.7
-9.8	52.9
-13.9	50.5
-8.3	54.2
-27.1	79.8
-23	70.4
-25.2	67.7
-23.2	72
-18.5	74.6
-20.7	73.4
-21.2	79.1
-22.2	79.2
-28.6	79.2
-6.5	38.1
-1.7	46.8
-10.5	51.4
-5.1	51.5
-7.9	44.7

Minor strain, %	Major strain, %
-5	50.2
-2.8	44.9
-3.2	40.5
-3.2	48.3
-25.2	72.9
-23.6	86.1
-26.4	74.4
-21.4	76.1
-20.6	82.1
-22.4	73.7
-20.9	71.2
-15.2	68.9
-25.7	73.4
-5.3	35.9
1	41.6
-2.2	44
1.4	42
-6.5	49.6
-8	48.9
-28	84.9
-25.5	84.3
-19	81.7
-16.5	72.3
-19.8	78.7
-26.4	65.7
-24	71.4
-22.9	75.7
-4.6	40.8
-0.1	36.6
1.1	40.1
1.7	31.3
-2	32.4
3.6	40.4
-4.6	40.8

Minor strain, %	Major strain, %
2.3	30
-0.3	35
5.8	36.7
-4.6	42.2
-2.7	47.4
-1.2	45.9
5.8	35
-0.2	44.4
-1.2	36.7
0.5	35.2
0.2	36.9
3.3	33.9
1.1	37.1
3.4	31.1
-1.8	27.2
4.8	37.9
-3.1	39.1
3.2	37.7
9.6	38.8
5.1	34.2
4.2	38.4
2.5	42
6.1	31.4
0.8	44.2
3	46.8
13.2	44.6
12.2	38.7
12.7	43.6
8.1	44.7
12.2	42.4
4.4	50.5
7.7	53.2
13.1	48.4
16.2	45.8
14.6	41.3
8.4	43
10.7	45.2
17.5	50.2
12	43.4
10.7	44.8

C.2. Major and minor strain values for the GMX tailor welded blank – failed region.

Minor strain, %	Major strain, %
-8.6	72.8
-13.5	73.2
-15.3	79.3
-7.8	80.1
-8.5	69.3
-17.4	80.6
-12.9	69.4
-8.2	72
-3.6	68.2
-7.3	68.8
-3.9	67.3
-2.4	71.2
-1.9	76.5
-11.8	75.2
-1.2	57.6
-5.6	57.4
-6.7	63.2
-7.2	66.1
-5.9	62.2
0.5	65
-7.4	68.9
-0.5	65.8
-25.5	94.3
-25.8	94.5
-25.2	93.7
-24.1	92
2.4	63.5
-4.7	62.2
3.7	63.8
-2.2	62.1

Minor strain, %	Major strain, %
-6.2	66.1
0	64.5
-4.3	64.3
-22.7	92.8
-23.2	94
-24.9	95.7
3.3	53.9
1	59
-2	56.4
0.2	62.5
2.4	63.6
-2.7	54.3
-1.5	62.3
11.4	53
2.8	54.4
1.7	54.3
0.8	55.4
-0.9	81.7
1	65.5
9.7	80
14.9	72.1
14.3	62.8
3.6	55
11.2	57.8
7.2	63.4
10.1	74.2

C.3. Major and minor strain values for the W-Car tailor welded blank – safe region.

Minor strain, %	Major strain, %
-11.5	53
-10.4	61.2
-14.3	66.7
-6.5	60.4
-14.9	64.1
-11.8	63.4
-12.2	53.3
-9.4	60.3
-7.2	66.6
-11.8	60.4
-3.8	51
-5.4	49.8
-1.3	48.6
-6.1	49.8
-1.6	47.3
-5.7	49.5
-6.6	52.6
-7.7	51.8
-4.3	47.3
0.4	47.2
-4.5	45.1
-4.4	41
-3.1	41.6
-2.1	39.8
1	43.5
8.5	47
5.7	49.2
2.5	44.9
0	49.2
5.4	44.7
7	43.4
5.9	43.8
10.6	44.7
5.5	43.1
12.7	46.6
7.2	45.2
13.2	44.8
11.3	53.7
11.7	57.8

Minor strain, %	Major strain, %
-3	54.3
15.3	53.6
7.2	57.5
9.4	57.5
10	58.1
3.4	45.3
8.2	47.9
8.2	50.8
12.3	58.7
4.4	53.1
11.8	47.2
-15.7	68.6
-21	68
-19.8	63.5
-18.8	61.1
-20.5	55.5

C.4. Major and minor strain values for the W-Car tailor welded blank – failed region.

Minor strain, %	Major strain, %
-8.1	75.4
-9	71.5
-7.9	73.7
-16.7	78.4
-8.5	81.6
-14.1	79.9
1.7	58.8
-1.7	60.1
-3.9	61.8
1.1	68.5
-5.1	66.8
-1.1	76.2
-5.8	79.1
2.3	77.3
3.1	68.1
-5.3	63.7
0.2	56.9
8.7	60.7
1.4	64.6

Minor strain, %	Major strain, %
5.7	61.8
10.2	73.8
7.4	64.9
8.4	60.5
12.1	62.5
4.7	56.9
2	55.9
8.8	61.4
7.8	61.7
12.4	66.6
2.6	64.4
18.8	67.4
4.3	63.1
15.2	64.2
5.4	69.5
5.5	64.7
6.7	61.4
2.9	62.3
9.7	62
-16.9	77.7

C.5. Major and minor strain values for the MC-DI tailor welded blank – safe region.

Minor strain, %	Major strain, %
-22	82.6
-23.8	90.5
-22.9	92.3
-21.1	84.2
-22.3	85.3
-20.6	86.7
-21.7	89.2
-20.1	86.1
-16.1	75.3
-17.4	70.3
-15.2	65.2
-12	64.1
-12.2	64.5
-13.8	59.8

Minor strain, %	Major strain, %
-17.6	64.4
-22.6	88.2
-13.5	64.8
-13.4	66.3
-10.8	63.9
-9.7	60.4
-12.4	68.8
-8.3	54.3
-9.9	56.9
-9.1	56.7
-7.3	56.1
-4.8	49.8
-9.1	49.6
-3	51.4
-11.5	51.6
-8.1	57.2
-10	59.9
-3.8	46.4
-4.4	54.9
-2.7	52.3
-6.4	52.9
-1.1	52.4
-7.6	50.1
-5	51.5
0.5	47.9
-4.9	47.7
1.4	51.5
-1	49.4
3.3	48.6
0	52.5
5.5	50.1
-2.9	46.1
4.4	49.2
-0.5	46.1
-3.5	51.6
0.9	53.6
13.7	56.4
3.9	50.4
8	46.8

Minor strain, %	Major strain, %
13.8	48
8.6	56.8
5.1	49.9
10.8	48
5.5	46.9
10.7	50.1
7.9	51.8
15.3	57
15.5	52.1
14.6	51.7
7.4	56.7
7.7	48.5
11.1	49.2
6.7	46.1
12.7	50.4
10.1	54.4
20.4	56.9
6.8	57.8

C.6. Major and minor strain values for the MC-DI tailor welded blank – failed region.

Minor strain, %	Major strain, %
-20.5	94.9
-21.4	95.8
-24.4	98.4
-24.4	95.4
-25.5	99.9
-21.7	99.5
-16.7	93.6
-14.4	88.3
-20.9	94.7
-19.4	93.5
-15.9	91.6
-14.1	87.5
-20.2	91.6
-15.1	86.9
-14.1	83.7
-11.4	83.3
-11.8	90.8

Minor strain, %	Major strain, %
-14.4	84.5
-7.3	68.4
-11.5	81.5
-11.1	78.4
-2.3	66.7
-10.5	69.3
-8.7	70.3
-9.6	69.2
-8.5	71.9
-7.4	80.1
-7.1	74.8
-7	70.4
0.7	58.3
1.8	59.1
0.6	61.3
1.5	61.9
2.1	60.5
5.9	60.4
7.9	61.7
12.8	73.2
13.4	64
3.6	62.2
3.2	64.7
4	66.2
7.7	61.4
6.2	60
5.4	59.8
7.1	60.2
8.3	65.5
9.3	69.4
15.1	67.6
13.9	65.5
7.5	72.4
18.3	65.8
12.8	71.9
12.4	71.3
9.6	72.2
7.7	69.6
8.4	71.1
11.1	73.5

Appendix D

D.1. Recorded data for plotting the S-N curves.

I.D.	Stress amplitude, MPa	Number of cycles, N
GMX	150	2918
	140	33589
	140	38929
	130	525092
	130	1092480
	120	10020025
	120	10001655
W-Car	130	432
	130	1728
	130	7185
	130	8467
	120	54413
	120	167349
	110	403904
	100	1345917
	100	1559111
	90	384520
	90	1938880
	85	10035376
	85	10044875

I.D.	Stress amplitude, MPa	Number of cycles, N
MC-DI	130	1047
	130	1143
	130	4025
	120	39302
	110	689411
	110	137901
	100	248993
	100	322475
	100	397665
	90	4350597
	85	10035376
	85	10035376
BM	150	120
	140	463
	130	4617
	130	6022
	120	151246
	120	263731
	110	10005086
	110	10065911

Curriculum Vitae

Dheeraj Anand

EDUCATION: Master of Applied Science (2004)
Ryerson University, Toronto, ON, Canada
Major: Mechanical Engineering, GPA: 3.81

Bachelor of Engineering (2000)
Government College of Engineering, Pune, India
Major: Metallurgy, Marks: 64.8%, First Class

EXPERIENCE: Senior Executive – Sales and Marketing, March 2002 to August 2002
Mahindra Ugin Steel Company Ltd., Mumbai, India

Graduate Engineer Trainee, March 2001 to March 2002
Jindal Iron and Steel Company Ltd., Vasind, India

Trainee Metallurgist, September 2000 to February 2001
Metallurgical Services, Mumbai, India

PUBLICATIONS: D. Anand, G. Boudreau, P. Andreychuk, D. L. Chen and S. D. Bhole,
"Formability of Tailor (Laser) Welded Blanks for Automotive Applications",
16th Canadian Materials Science Conference, Ottawa, Canada, 5-8 June,
2004, Edited by J. Beddoes, p. 57.

D. Anand, D. L. Chen, S. D. Bhole, P. Andreychuk and G. Boudreau,
"Fatigue Strength of Tailor (Laser) Welded Blanks for Automotive
Applications", Journal publication under review, Materials Science and
Engineering: A.

D. Anand, G. Boudreau, P. Andreychuk, D. L. Chen and S. D. Bhole,
"Forming Behavior of Tailor (Laser) Welded Blanks for Automotive
Applications", Journal publication under review, Canadian Metallurgical
Quarterly.